Process Modelling of the Recovery of Volatile Organic Compounds on Activated Carbon Monoliths

Chehadeh Al Kahf, Dduha

Award date:
2013

Awarding institution:
University of Bath

Process Modelling of the Recovery of Volatile Organic Compounds on Activated Carbon Monoliths

Dduha Chehadeh Al Kahf

A Thesis submitted for the degree of Doctor of Philosophy

University of Bath

Department of Chemical Engineering

June 2013

Dedicated to Yasser

Abstract

The research described in this thesis is to develop and validate a process system model for an electrothermal swing adsorption (ESA) process that incorporates novel activated carbon monoliths (ACMs) for the recovery of volatile organic compounds (VOCs). The process system comprises two columns one dedicated for adsorption and the other for desorption and works in a cyclic mode of operation. Two mathematical models have been developed to describe the process system, namely in one dimension (1D) and in three dimensions (3D). The developed models have been validated using experimental data at the bench and the pilot scale, at different operating conditions and for two VOCs. It has been concluded that the 1D model was sufficient to represent the experimental data of the current study without going through the trouble of using the 3D model which was more demanding in terms of formulation and computation. The linear driving force approximation (LDF) approximation adequately predicted the concentration of VOCs in the gas phase with no need for a fundamental diffusion study within the solid of the ACMs. The kinetics of adsorption and desorption was governed by the mass transfer coefficient which was found by parameter estimation and was directly related to the internal mass transfer coefficient controlled mainly by molecular diffusion inside the pore structure of the ACMs.

Acknowledgments

"*My Lord, increase me in knowledge*" Al Qur'an Surah 20: Verse 114

In our quest for knowledge, pursuit of our dreams and search for happiness we long for a better life. The people around us shape this life and to them acknowledgments are due.

I would like to thank Prof. Barry Crittenden for giving me the opportunity to pursue my Ph.D. studies at the University of Bath. I am deeply grateful for the long hours spent in his office and the vivid discussions.

Thanks are due to Prof. Haitham Lababidi of Kuwait University for this support throughout this work. Without his help, this work would not have been possible.

A big thank you note "Merci" goes to Dr. Olivier Camus for sharing with me experimental data based on which the built models were validated.

I would like to acknowledge the academic and research community for sharing their valuable endeavours. I have had some enlightening communications with members of this community throughout this work, and I value the generosity of those, Dr. S. Tennisson, Dr. C. Grande, Dr. F. Yu and Dr. G. Koumpouras, who were willing to share their experiences.

My deep gratitude and appreciation go to my parents for their continuous support and encouragement.

Yahia, Salma and Massa, you are my life. May your dreams come true!

Table of Contents

List of Tables

List of Figures

Nomenclature

A	Gas channel surface area	m^2
a	Half channel side length	m
a_s	Specific surface area	m^{-1}
a_m	Specific surface area	m^{-1}
a_w	Specific surface area	m^{-1}
b	Affinity coefficient	Pa^{-1}
b_0	Affinity parameter	Pa^{-1}
c	Gas concentration	mol m^{-3}
c_0	Initial gas concentration	mol m^{-3}
c_{pore}	Gas concentration in pore	mol m^{-3}
c_{pa}	Heat capacity of air	J kg^{-1} K^{-1}
c_{pc}	Heat capacity of carbon	J kg^{-1} K^{-1}
c_{pg}	Heat capacity of gas	J kg-1 K^{-1}
c_{pn}	Heat capacity of nitrogen	J kg^{-1} K^{-1}
c_{ps}	Heat capacity of solid	J kg^{-1} K^{-1}
c_{pw}	Heat capacity of water	J kg^{-1} K^{-1}
c_w	Concentration in the wall	mol m^{-3}
c^*	Concentration at the gas solid interface	mol m^{-3}
d	Channel side length	m
D	Diameter of monolith	m
D_{ax}	Axial diffusion coefficient	m^2 s^{-1}
D_c	Intra-crystalline diffusivity	m^2 s^{-1}
D_{eff}	Effective diffusion coefficient	m^2 s^{-1}
D_k	Knudsen diffusivity	m^2 s^{-1}
D_{mol}	Molecular diffusion coefficient	m^2 s^{-1}
D_p	Pore diffusivity	m^2 s^{-1}

e	Channel wall thickness	m
h_s	Heat transfer coefficient gas/solid	W m^{-2} K^{-1}
h_w	Heat transfer coefficient solid/wall	W m^{-2} K^{-1}
h_a	Heat transfer coefficient wall/air	W m^{-2} K^{-1}
k	Mass transfer coefficient	s^{-1}
K	Henry's law adsorption constant	
K_{ax}	Axial thermal conductivity	W m^{-1} K^{-1}
k_c	Internal mass transfer coefficient	s^{-1}
k_e	External mass transfer coefficient	s^{-1}
k_f	Film mass transfer coefficient	s^{-1}
L	Length of monolith	m
M_A	Molar mass of A	g mol^{-1}
M_B	Molar mass of B	g mol^{-1}
MW	Molecular weight	g mol^{-1}
Nu	Nusselt number	
P	Pressure	Pa
p	Partial pressure	Pa
Pr	Prandtl number	
P_v	Volumetric power	W m^{-3}
Q	Flow rate	l min^{-1}
q	Amount of VOC adsorbed	mol kg^{-1}
q^*	Loading in equilibrium with gas	mol kg^{-1}
$\bar{q}$	Average loading	mol kg^{-1}
q_m	Maximum amount adsorbed	mol kg^{-1}
q_1	Loading in section q_1	mol kg^{-1}
q_2	Loading in section q_2	mol kg^{-1}
q_3	Loading in section q_3	mol kg^{-1}
$\bar{q}_{11}$	Average loading at interface q_{11}	mol kg^{-1}
q^*_{11}	Loading in equilibrium with gas	mol kg^{-1}
$\bar{q}_{22}$	Average loading at interface q_{22}	mol kg^{-1}

q^*_{22}	Loading in equilibrium with gas	mol kg^{-1}
r	Radial direction	m
R	Ideal gas constant	m^3 Pa K^{-1} mol^{-1}
R_p	Adsorbent pellet radius	m
R_x	Single channel half-length in x direction	m
Re	Reynolds number	
r_c	Crystal or micro-particle	m
r_i	Internal radius of hollow cylinder	m
r_o	External radius of hollow cylinder	m
Sc	Schmidt number	
Sh	Sherwood number	
t	Time	s
t	Tóth parameter	
T	Temperature	K
T_a	Ambient temperature	K
T_g	Gas temperature	K
T_s	Solid temperature	K
T_w	Wall temperature	K
t_w	Half channel wall thickness	m
u	Velocity	m s^{-1}
u_{ave}	Interstitial velocity	m s^{-1}
u_m	Specific molar flux	mol m^{-2} s^{-1}
V_A	Molar volume of A	mol m^{-3}
V_B	Molar volume of B	mol m^{-3}
W	$t_w + a$	m
x	Axial direction	m
y, y_1, y_2, y_3	Y axes of distribution domains	m
y	Mole fraction	
y_0	Initial mole fraction	
z, z_1, z_2, z_3	Z axes of distribution domains	m

Greek Letters

ΔH_{ads}	Isosteric heat of adsorption	J mol^{-1}
ΔH	Enthalpy change	J mol^{-1}
ΔP	Pressure difference	Pa
ΔS	Entropy change	J mol^{-1} K^{-1}
ε	Porosity of monolith	
ε_p	Porosity of adsorbent particle	
ρ	Density	mol m^{-3}
ρ	Electrical Resistivity	Ω
ρ_g	Density of gas	mol m^{-3}
ρ_s	Density of solid	kg m^{-3}
μ	Viscosity	kg s^{-1} m^{-1}
μ_g	Gas viscosity	kg s^{-1} m^{-1}
σ_A	Collision parameter of A	Å
σ_B	Collision parameter of B	Å
σ_{AB}	Collision parameter	Å
Ω	Parameter of the species interaction	
τ_p	Tortuosity factor	
λ	Thermal conductivity	W m^{-1} K^{-1}
η	Fin efficiency of internal heat-exchanger	

Abbreviations

1D	One dimension
2D	Two dimensions
3D	Three dimensions
ACM	Activated carbon monolith
ACFC	Activated carbon fibre cloth
AIChE	American Institute of Chemical Engineers
CFC	Chlorofluorocarbon
DCM	Dichloromethane (methylene chloride)
EPA	Environmental Protection Agency
ESA	Electrothermal swing adsorption
FID	Flame ionization detector
IGA	Intelligent gravimetric analyser
IUPAC	International Union of Pure and Applied Chemistry
LDF	Linear driving force
MTZ	Mass transfer zone
PSA	Pressure swing adsorption
PSE	Process Systems Enterprise
ppbv	Parts per billion volume
ppmv	Parts per million volume
TSA	Temperature swing adsorption
TSB	Technology Strategy Board
VOC	Volatile Organic compound

Chapter 1

Introduction

Mankind since ancient times has been seeking energy resources in his pursuit to shape his environment. Nowadays, more attention is being paid to the environment, and stricter regulations are being imposed for its protection as conventional energy sources are emitting pollutants to the atmosphere thereby jeopardizing public health.

Volatile organic compounds (VOCs) are toxic polluting compounds and have direct impact on human health. In the atmosphere, they are precursors to the formation of highly toxic compounds: pollutant ozone O_3 and smog. VOCs are emitted to the air from different sources. The predominant source remains the automobile industry with the contribution of other commencers such as paint, petroleum, solvent, lubricant, etc. VOC emission and control involve the removal and the recovery of VOCs from air streams, as the loss of VOCs to the atmosphere represents a loss of valuable hydrocarbon resources.

Activated carbon monoliths (ACMs) have been considered a suitable sorbent for the removal and recovery of VOCs from air streams. Activated carbon is a processed porous form of carbon with large surface area suitable for adsorption. These activated carbons, in their monolithic form, consist of a bundle of channels resembling a honeycomb. They have equivalent performance compared with their granular carbon counterparts. They are, however, more advantageous in performance due to their lower pressure drop and their higher electrical conductivity (Crittenden, *et al*., 2005; Camus, *et al*., 2007).

Adsorption of VOCs on activated carbon monolith is used for the removal of VOCs at low concentration. The knowledge of this technology is fundamental for its proper application. The type of adsorption process used in this study is temperature swing adsorption (TSA) and particularly a branch of TSA known as electrothermal swing

adsorption (ESA), since the activated carbon monoliths are electrically conducting and can be electrically regenerated. This separation process consists of a cyclic sequence of adsorption and desorption in which the adsorption step adsorbs the VOCs onto the ACM and the desorption step regenerates the adsorbent surface for reuse during the subsequent adsorption step.

Modelling of the ESA process proposes a mathematical model that covers the whole cyclic process from its start-up condition up to its cyclic steady state and involves dynamic mass and energy balances in one or three dimensional spaces in the gas and solid phases of the monolithic channels.

The mathematical model developed can be applied on a currently initialized £2.3 million Technology Strategy Board (TSB) project which has delivered its first prototype unit for the recovery of solvents in an industrial company. The prototype illustrated in Figure 1 is currently on test recovering over 93% of ethanol from a diluted air stream (Crittenden, 2011).

Figure 1. Prototype unit (Crittenden, 2011)

1.1. Aim

The overall aim of research on this TSB project is to develop equipment that can control and manage VOCs in factory air streams. VOCs are major air pollutants threatening the public health. Nonetheless, VOCs represent valuable resources not to be wasted. Adsorption on activated carbon is a popular technology for the recovery of low concentration VOCs from air streams. ACMs are advantageous vis-à-vis their granular counterpart in term of pressure drop and fast regeneration. The aim of this thesis is the recovery process of VOCs in a dynamic process comprising adsorption and desorption conducted in a cyclic mode of operation to recover the VOC from the ACM and then to regenerate the ACM for reuse.

1.2. Objective

The objective of this thesis is to develop and validate a process system model for an electrothermal swing adsorption (ESA) process that incorporates novel activated carbon monoliths for the recovery of volatile organic compounds. A number of models have been developed in the literature to represent the dynamic ESA process, and some of these models are covered in this thesis and have been used as a starting point in modelling.

The research involves modelling the cyclic adsorption/regeneration process used to remove VOCs from air steams. Mathematical modelling of the ESA system is established incrementally from the simpler models toward the overall goal of modelling the complete cyclic steady state process. Process modelling in 3D of the ESA cycle for the recovery of VOC on activated carbon monoliths will be considered in the current research, and 1D modelling will be studied as a building block towards the 3D model.

The mathematical model to be tackled will encounter the following complexities:

- The performance of the process is strongly dependent on the operating conditions.
- The need to cope with high temperature (200°C) when dealing with desorption since this is approximately the temperature required for ACM regeneration.
- The selection of the modelling software that can handle cyclic processes from start-up to steady state conditions.

- The assumptions made for the sake of model development.
- The formulation of the modelling equations, boundary and initial conditions.
- The validation of the model with experimental data.

1.3. Scope

The scope of this thesis is to model the cyclic ESA process in three dimensions for the recovery of an example VOC, namely dichloromethane (DCM), using ACMs supplied by MAST Carbon Technology Ltd. The modelling was conducted using gPROMS software of PSE. Two models have been developed, namely in one dimension (1D) and in three dimensions (3D). The developed 1D and 3D models have been validated using experimental data obtained from the University of Bath. The experimental data used have been produced by Dr. O. Camus from the bench and pilot scale platforms present in the laboratories of the Chemical Engineering Department at the University of Bath. The 1D and 3D models have then been compared, and conclusions have been drawn based upon this comparison.

This thesis comprises ten Chapters, and these Chapters are described briefly as follows:

Chapter 1: Introduction

The present Chapter establishes a brief background to the topics of this study by supplying the definitions of the main terms discussed throughout the thesis. In addition, this Chapter sets the boundary of the study by briefly identifying the aim, objective and scope of the conducted work.

Chapter 2: Volatile organic compounds (VOCs)

Volatile organic compounds are defined in this Chapter along with their emission and control technologies. VOCs emission levels and their regulating legislations are touched upon. In addition, a summary of the control technologies suitable for VOC abatement is presented.

Chapter 3: Activated carbon monoliths (ACMs)

Activated carbon monoliths used for the removal of VOCs from gas streams are studied in this Chapter. The different production schemes used for ACM manufacturing are discussed covering specifically the production of the MAST ACM. The application of ACMs in different industries is also considered to demonstrate their use and viability.

Chapter 4: Modelling

This Chapter establishes the ground level of this study, as modelling is the heart of this thesis. The basic concepts of adsorption equilibrium and kinetics are introduced. The choice of modelling software and its selection criteria are discussed. Ultimately, the modelling approaches used in the literature are presented as a starting point in the quest for the ideal model.

Chapter 5: One-dimensional modelling

One dimensional modelling is the building block of the extended modelling covered at a later stage. The equations and parameters of the constructed 1D model are identified and presented. Also the modelling organization in gPROMS is initiated at this stage.

Chapter 6: One-dimensional modelling results

The results of 1D modelling are presented in this Chapter, including a parametric study and parameter estimation of the constructed model. The adsorption, desorption and cyclic modes of operation are tested. Finally, the model is validated on the bench and pilot scales for dichloromethane (DCM) and for another type of VOC (toluene).

Chapter 7: Three-dimensional modelling

Three dimensional modelling is presented in this Chapter covering the aspects that differentiate 1D from 3D modelling. The deduced equations of the 3D model are detailed along with the methodology behind their presentation.

Chapter 8: Three-dimensional modelling results

The results of 3D modelling derived in the previous Chapter are covered in this Chapter. Specifically, the resulting breakthrough curves are illustrated in the 3D arrangement.

Chapter 9: Discussion

The overall outcome of this work is discussed and compared to similar and relevant work in the literature. The results of 1D and 3D modelling are particularly evaluated.

Chapter 10: Conclusions and recommendations

Finally, Chapter 10 presents the conclusions deduced from this work and provides the reader with recommendations that can be beneficial for future work and similar applications.

1.4. References

Camus, O., Crittenden, B., Perera, S., Mays, T., Sánchez-Liarte, F., Patsos, A., Tennison, S. R. & Crezee, E., 2007. Non-uniformities in adsorbent monoliths, *In: 9th International conference on Fundamentals of Adsorption*, 20 - 25 May. Giardini Naxos, Sicily.

Crittenden, B. D., 2011. *Discussion on prototype* [email] (Personal communication, 5 December 2011).

Crittenden, B. D., Patton, A., Jouin, C., Perera, S. P. & Tennison, S., 2005. Carbon Monoliths: a comparison with Granular materials. *Adsorption*, 11, pp.537-541.

Chapter 2

VOC emission & control

Worldwide, stricter environmental regulations impose the continuous monitoring, logging and controlling of pollutants emitted into the atmosphere from different industries. Volatile organic compounds (VOCs) are major air pollutants harmful to human health. Their toxicity presses public and governments to attach great importance to the study of VOC emission and control (AIChE, 2001; Moretti, 2002).

2.1. VOC definition

There is no clear and general definition of VOCs, but regulations and policies create the legal definitions of VOCs. In general, VOCs are organic compounds with high vapour pressures so that they exist in the gas phase at ambient conditions. They are carbon containing compounds that evaporate into the air (UK Environment Agency), and they roughly have a vapour pressure equivalent to 0.01 kPa at 20 ºC (US Environmental Protection Agency). There are millions of different compounds which may be classified as VOCs. Usually, those that are nose detectable as smells are VOCs.

Industrial chemicals such as fuels, coatings, paints, pesticides, and refrigerants are usually VOCs. Fuel consumption emits VOCs directly as products upon fuelling (gasoline) or indirectly as by-products upon combustion (automobile exhaust). Volatile organic compounds (VOCs) are numerous and varied and cover a wide and large number of products, such as construction materials, office equipments, craftsmen tools and photographic solutions. Also a number of household consumer products, such as cleaning solvents, detergents, and wooden furniture all emit VOC compounds (EPA, 1995).

VOCs can have a direct impact on human health arising from their toxicity. They also may contribute to allergic or asthmatic symptoms. Many are carcinogenic and are precursors to ozone formation. VOCs react with nitrogen oxides (NO_x) and produce photochemical pollutant (tropospheric) ozone O_3, a toxic greenhouse gas harmful to the environment and to human health.

The impact of ozone is different depending on its location in the atmosphere. Stratospheric ozone, found in the upper atmosphere, protects the earth from the dangerous ultraviolet (UV) radiation, as ozone absorbs the UV light. On the other hand, ground level ozone, or tropospheric ozone, has adverse effects on human health.

In addition, VOCs play a major role in smog formation. VOCs, under sunbeams, react with polluting NO_x emitted from various chemical industries to form ground-level ozone. The build up of ozone, fine particulates and other gaseous pollutants results in the formation of smog. Smog is a problem in a number of cities. It reduces visibility and harms public health. Smog irritates the eye, nose and throat (ENT) system and aggravates existing heart and respiratory problems (e.g. asthma) affecting mostly the fragile population (children & elderly) by putting their respiratory and circulatory systems at risk.

2.2. VOC emission

The loss of VOCs to the atmosphere represents a loss of valuable resources. Figure 2 shows the predominant sources of VOCs. The main contributor remains from motor vehicles followed by the solvents industry covering paints and coatings (Perth Airshed, 2003).

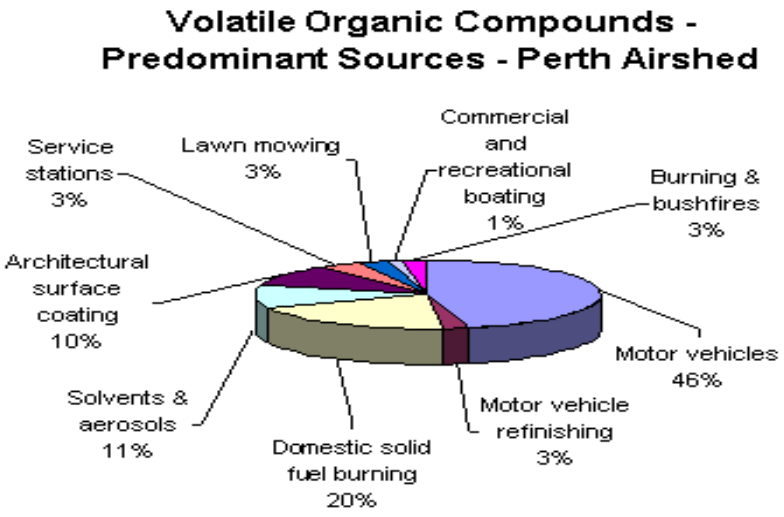

Figure 2. Predominant sources of VOCs (Perth Airshed, 2003)

The removal of VOCs from air streams is of significant importance in relation to air pollution control, as air pollution is one of the major environmental concerns affecting the quality of our life. VOC emission control legislation varies throughout the European Union and the United States. Over 200 EC directives and regulations relating to the environment have been issued and are continuously changing. It is hard to present complete details of each piece of legislation or the control of the different VOC emission sources, which include painting processes, surface cleaning, coating processes, etc.

Volatile organic compound (VOC) emissions are coming under increased inspection worldwide and especially in both Europe and the United States. The European Commission advocated a VOC limit for solvent-borne paints at 400 g l^{-1} in 2007 and 300 g l^{-1} in 2010. Similarly, the United States Environmental Protection Agency (USEPA) regulated the VOC levels of many consumer products in order to improve air quality. Regional VOC regulations imposed by the Ozone Transport Commission (OTC), California Air Resources Board (CARB) and South Coast Air Quality Management District (SCAQMD) have stricter limits on VOC content in comparison to the national VOC standards set by USEPA. The VOC rule adopted by the OTC for many consumer products was 350 g l^{-1}, and this regulation went into effect in 2005.

In view of the control measures for VOC abatement, the UK has met its target of reducing emissions of VOCs to less than 1.2 million tonnes per year in 2010 under the EU National Emission ceiling directive and the 1999 Gothenburg protocol to cut VOC emission by 40% in 2010 compared to 1990 (Department of Environment, Food and Rural Affairs, 2011). VOC concentrations decreased significantly in the UK from 1998 through 2008 for a number of VOC compounds ranging from -3% to -26% per year. This decrease was more important in London in comparison to sites in rural England as reported by Schneidemesser, *et al*. (2010) and presented in Table 1. For example, toluene decreased from 10 ppbv in 1998 to 1 ppbv in 2008 at an average rate of -22% per year at a selected site in London.

Table 1. VOC trends extracted from Schneidemesser, *et al*. (2010)

Compound	London		Rural England	
	2008 g-mean (ppbv)	change per year 1998 – 2008 (%)	2008 g-mean (ppbv)	change per year 1998 - 2008 (%)
Propane	2.7	-3	0.61	-3%
Pentane	0.54	-12	0.081	-2%
Ethene	2.4	-20	0.29	-6
Benzene	0.32	-26	0.088	-12%
Toluene	1.0	-22	0.12	-9%

VOC emissions have also declined in the United States. Figure 3 shows approximations of U.S. emission levels of VOCs. Emissions reached their highest level around 1970 and later on have decreased by about 40% from that level. Major contributors are industrial applications, solvent utilization (paints), non-road sources (marine and garden equipments) and road related sources (Allen, 2004).

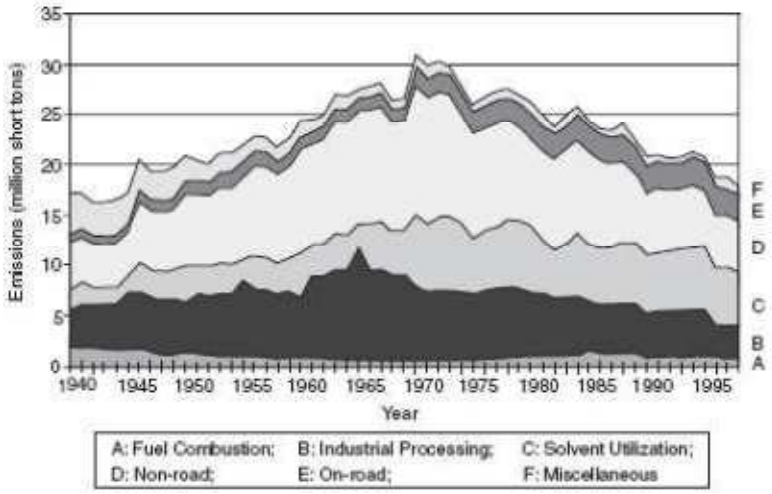

Figure 3. Emission trends of VOCs 1940-1998, in USA (Allen, 2004)

2.3. VOC control

The best way to avoid VOC emission is to control its source by using materials and products that do not give off VOCs. Pollution prevention, or source reduction, offers itself as the waste management strategy of choice because it avoids the generation of waste in the first place.

The next level down the hierarchy of waste management is to reduce the use of VOCs and thereby reduce their emissions. Rather than arguing about how to treat or where to put the wastes created, society needs to design systems that imitate the cycles of nature whereby waste is reduced.

The subsequent downward level is recycling, that is to recover the VOCs emitted so that they can be reused, especially if the recovered VOCs have a recovery value lower than the purchase of new VOCs. Condensation and adsorption both offer highly efficient treatment systems to remove and recover VOCs from gaseous process streams. They are known techniques with paybacks on the installation and operation. Adsorption onto activated carbon monoliths followed by electrically-driven regeneration and condensation allows valuable compounds to be recovered and stringent environmental regulations to be met. This very important solvent recovery process is the subject of this thesis.

The next level down the hierarchy is to destroy the VOCs with energy recovery. Thermal oxidizers burn off VOCs from process exhausts. This regenerative technology

offers an impressive energy saving and results in a rapid payback period on the investment. In addition, the main advantage of this system is its extremely high thermal energy recovery. However, the additional fuel required to support combustion leads to both the reduction in non-renewable resources as well as an increase in greenhouse gas emissions. In addition, the solvent is lost.

Finally, the lowest level in the waste management hierarchy is to destroy VOCs by incineration with no energy recovery, especially if the VOC stream cannot be recovered, has no recovery value, or if there is a disposal concern for a toxic compound. Figure 4 illustrates the levels of the waste management hierarchy.

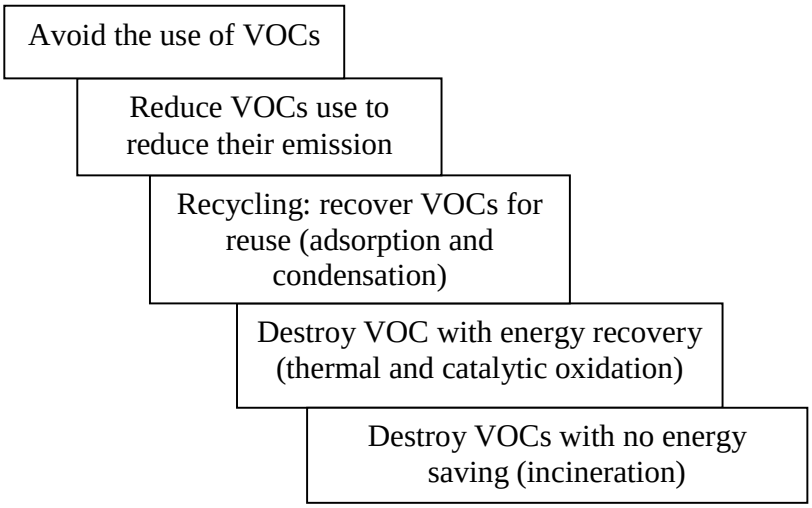

Figure 4. Waste management hierarchy

The widespread techniques for removing VOCs from gas streams are condensation, oxidation and adsorption. The choice depends, to a large extent, on the flow rates, compositions and concentrations to be dealt with, as well as on whether destruction or recovery is required, as illustrated in Figure 5.

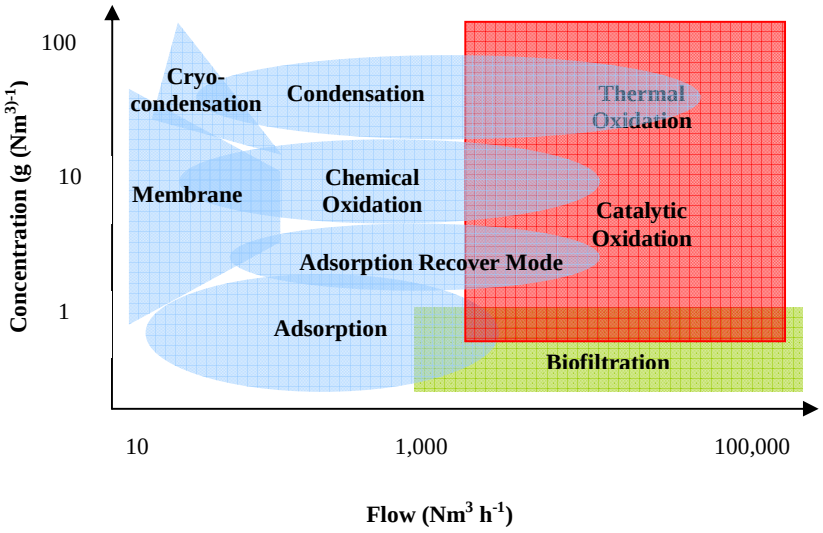

Figure 5. VOC removal (Waterleau – Belgium)

Condensation is generally suitable at high VOC concentrations, because of the low temperatures required as partial pressures fall. Oxidation, either over a catalyst (catalytic oxidation) or in a direct flame (thermal oxidation) has low capital costs but can be wasteful and costly to run. Adsorption, on activated carbon, is capital-intensive, but new progress promises to make adsorption more competitive. Control technologies are described and compared in more detail in the following sections based on functions, uses and limitations (AIChE, 2001; Moretti, 2002).

2.2.1. Condensation

Cryogenic or low temperature condensation is suitable for VOC emission control due to its capability in recovering practically any VOC under varying conditions. It can handle all organics and operate with changing concentrations and compositions over time. This flexibility renders cryogenic condensation predominantly appropriate for VOC emission control in wide-ranging plants with varying products.

The condensation process allows the recovery of VOCs for reprocessing. The process operates at very low temperatures to cool the organic vapours so the VOCs can

be condensed when the dew point is reached. The temperature of the process stream is decreased to lower the vapour pressure of the VOC thereby increasing its recovery in the liquid phase. With the phase out of the ozone-depleting chlorofluorocarbon (CFC) refrigerants, liquid nitrogen is used for example to condense the VOCs in this low-temperature condensation process.

Nitrogen is suitable for use since it is inert, abundantly used in the chemical industry and is commonly transported and stored in its liquid state at reduced temperature and elevated pressure. In addition, the low temperature capability of liquid nitrogen allows for the condensation of most organic compounds from their emission streams. The vented nitrogen can then be reused after its recycling.

Cryogenic condensation consists of a number of shell-and-tube heat exchangers. The VOC and the liquid nitrogen streams flow counter currently through the heat exchangers to enhance the heat transfer mechanism. The VOC condenses on the shell side of an exchanger then is collected into a tank. From this collection tank, the VOC can be recycled or recuperated for reuse or disposal.

2.2.2. Thermal oxidation

Thermal oxidation is the reaction of the air pollutants with oxygen under heat. By increasing the temperature of the pollutant above its auto-ignition point in the presence of oxygen, and maintaining it at high temperature for sufficient time to complete combustion, the VOCs are converted to carbon dioxide (CO_2), water vapour (H_2O), and usable heat. The combustion process is highly affected by the following parameters: exposure time, operating temperature, mixing rate and the availability of oxygen. These parameters shape the design of thermal oxidation systems. There are three main VOC oxidation systems: direct flame, recuperative, and regenerative.

Direct flame systems or flares oxidize the VOCs by the combustion of the polluted stream with a flame. These systems are the simplest thermal oxidizers and the cheapest to build. Except that they require the highest operating cost, as they necessitate the largest quantity of fuel to sustain the oxidation temperature.

Recuperative thermal oxidation, as it name implies, recovers part of the heat of combustion to preheat the stream going into the combustion chamber using tube or plate heat exchangers. Recuperative systems installation costs are higher than those of flares, but these recuperative systems operate at lower costs.

Regenerative thermal oxidation systems have higher heat recovery efficiencies than recuperative oxidizers requiring multiple heat exchanger beds to generate the heat efficiencies. As a result, the oxidation process starts in the beds of the heat exchangers and gets completed in the combustion chamber. These systems are the most expensive thermal oxidizers to install, but the saving in fuel balances the added investment.

2.2.3. Catalytic oxidation

Catalytic combustion is one of the important control technologies for the elimination of low concentration VOCs in polluted gas streams. Catalytic oxidation, similarly to other oxidation processes, converts the VOCs into CO_2 and H_2O. In catalytic oxidation, however, the added catalyst accelerates the rate of the reaction. Oxidation takes place at the catalyst surface where the oxygen and the VOCs react.

The catalytic oxidation takes place at a lower temperature than the one required for thermal oxidation due to the catalytic activity. Typical VOC catalytic oxidation temperatures range from 320°C to 540°C. The VOC polluted air is first preheated to reach a temperature necessary to initiate the catalytic oxidation. Then this preheated contaminated air is rapidly oxidized by passing through the catalyst beds (EPA, 1995).

Typical commercial VOC oxidation catalysts include metal oxides and noble metals supported on ceramic monoliths or pellets, and most of these catalysts have proprietary rights. Their life cycle is around five years and is prolonged with proper catalyst regeneration.

The advantages noted for the application of this technology are the complete oxidation of VOC, and the little formation of oxidation by-products, such as carbon monoxide (CO). In addition, this technology requires a low usage of fuel. The noted disadvantages, on the other hand, are catalyst poisoning and the sensitivity of the catalyst to elevated temperatures.

2.2.4. Absorption

Absorption is used as a product recovery technique for the disposal of VOCs from polluted gases, especially those VOCs that are water soluble. In this purification technique, the polluting VOCs are dissolved in water or a suitable liquid solvent. Absorption of the VOCs by the solvent takes place in counter current spray towers, scrubbers, or packed or plate columns (EPA, 1995).

The choice of absorption as the control system for the recovery of VOCs relies on the availability of a suitable liquid absorbent. The chosen absorbing solvent should have a high solubility for the organic vapours. Water is used to absorb water soluble VOCs. In addition, amphiphilic blocks added to water can make hydrophobic VOCs dissolve in water. On the other hand, hydrocarbon solvents such as oils are used for VOCs having low water solubility.

Another factor for determining the suitability of the absorption process as a purification technique lies in the treatment or disposal capacity of the material removed from the absorber. In general, the absorbing liquid containing the VOC is regenerated by stripping at high operating temperature and under vacuum to desorb the VOC from the absorbent liquid. The VOC is then condensed and recovered in its liquid form (EPA, 1995).

Absorption processes are widely used in industrial air purification for medium to highly concentrated gases (0.1 - 10 g m^{-3}) with medium flow rates (100 - 10,000 $m^3 hr^{-1}$). This control technique, however, is more suitable for controlling inorganic gases than for VOCs removal (EPA, 1995).

2.2.5. Biofiltration

Biological treatment, especially biofiltration, is an emerging air pollution control technology for treating VOCs in contaminated air. It is a cost effective oxidation process for certain polluted gas streams in comparison with other available VOC control technologies (Zhu, 2000). In biofiltration, the polluted waste gas stream is purified by its passage through a biologically active soil medium under aerobic conditions where the VOCs are biodegraded. Biofiltration uses microorganisms to degrade various pollutants.

The temperature and moisture of the air stream and biofilter bed are critical in design considerations (Zhu, 2000).

In recent years, new types of bioreactors and biofilters have been developed. Biofilters are bacteria or microorganisms supported filter beds. They are basically simple beds of dirt or drainage mud. Recently used biofilters have been bacteria carried on artificial supports (Kennes & Veiga, 2004). Biofiltration can achieve very high VOC removal efficiencies. This control technology is better suited for low VOC concentration and is appropriate for odour control.

2.2.6. Adsorption

In the low-concentration levels, adsorption on active carbon is the most commonly utilized control scheme for the recovery of VOCs from air streams with a broad range of flow rates (Crittenden, 1992; Ruddy & Carroll, 1993; Fuertes, *et al.*, 2003; Marban, *et al.*, 2006). Adsorption is used to explain the inclination of VOC molecules from a polluted gas phase to stick to the surface of the carbon, i.e. the VOC adsorbate molecules accumulate on the surface of the adsorbent solid.

Adsorption is a basic property of matter, due to the attractive forces between molecules. The force region creates an area of low potential energy near the adsorbing solid surface and, consequently, the adsorbed molecules are clustered on the solid surface. The molecular density close to the surface is generally greater than that in the bulk gas phase. Adsorption mainly depends on the difference in the affinity of the surface for different components. This difference in affinity is called selectivity. Adsorption due to its selectivity is a mean of purification of fluid mixture from trace components (Ruthven, 1984; Crittenden & Thomas, 1998).

Adsorption is categorized as chemical or physical adsorption (chemisorption or physisorption), depending on the nature of the surface forces. In physical adsorption the forces are fairly weak, involving largely van der Waals interactions. In chemisorption there is an important transfer of electrons between the adsorbate and the solid surface resembling the formation of a chemical bond. These chemical interactions are stronger

than the forces of physical adsorption and can involve only monolayer coverage, unlike in physical adsorption where many layers may form (Ruthven, 1984).

Adsorption of VOCs from polluted air streams onto activated carbon monoliths contribute to air emission control. This new technology can meet rigorous environmental regulations with two advantages: the first benefit is that air is purified, while the second benefit is that the VOCs can be recovered. This process for the recovery of VOCs from air streams is the subject of this thesis and will be covered in more detail in subsequent Chapters.

2.3. References

Allen, David T., 2004. Air Pollution. *Pages 787-815 of:* Seidel, A. (ed), *Kirk-Othmer Encyclopedia of Chemical Technology*, 5th ed., vol. 1. Hoboken, New Jersey: John Wiley & Sons, Inc.

American Institute of Chemical Engineers, 2001. Practical Solutions for Reducing and Controlling Volatile Organic Compounds and Hazardous Air Pollutants, *AIChE*, Center for Waste Reduction Technologies, New York, NY.

Crittenden, B.D & Thomas, W. J., 1998. *Adsorption Technology & Design.* Reed Education and professional publishing Ltd.

Crittenden, B.D., 1992. Selective adsorption – a maturing but poorly understood technology, in current best practice in separations technology, the R&D Clearing House, London, pp. 4.17/18.

Department of Environment, Food and Rural Affairs, 2011. Emissions of air pollutants in the UK, 1970 to 2010, Defra National statistics release.

EPA, 1995. U.S. EPA, Office of Air Quality Planning and Standards, "Survey of Control Technologies for Low Concentration Organic Vapor Gas Streams," EPA-456/R-95-003, Research Triangle Park, NC, May, 1995.

Fuertes, A. B., Marban, G. & Neveskaia, D. M., 2003. Adsorption of volatile organic compounds by means of activated carbon fiber-based monoliths. *Carbon*, 41, pp.87-96.

Kennes, C. & Veiga, M., 2004. Fungal biocatalysts in the biofiltration of VOC-polluted air. *Journal of Biotechnology*, 113 (1-3, 30), pp.305-319.

Marban, C., Valdés-Solís, T. & Fuertes, A. B., 2006. Modeling the breakthrough behavior of an activated carbon fibber monolith in *n*-butane adsorption from diluted streams. *Chemical Engineering Science***,** 61(14), pp.4762-4772.

Moretti, E., 2002. Reduce VOC and HAP Emissions. *Chemical Engineering Progress*, June, pp. 30-40.

Ruddy, E. N. & Carroll, L. A., 1993. Select the Best VOC Control Strategy. *Chemical Engineering Progress*, 89(7), pp.28.

Ruthven, D. M., 1984. *Principles of adsorption & adsorption processes*. John Wiley & sons, Inc.

Schneidemesser, E., Monks, P. S. & Plass-Duelmer, C., 2010. Global comparison of VOC and CO observation in urban areas. *Atmospheric Environment*, 44, pp.5053-5064.

Waterleau, *VOC Treatment Technology*. [Online] Belgium. Available at: http://www.water-leau.com/default2.aspx?PageId=162 [Accessed 8 May 2009].

Western Australian Department of Environmental Protection (2003) National Pollutant Inventory Perth Airshed Emissions Study 1998/1999.

Zhu, X., 2000. *A fundamental study of biofiltration process for VOC removal from waste gas streams*. Ph.D. dissertation. University of Cincinnati.

Chapter 3

Activated carbon monoliths

Activated carbons are porous carbons manufactured to exhibit large interior surface area and pore volume. These unique characteristics of activated carbon are responsible for its adsorptive properties in numerous industrial applications, especially the removal of impurities from gases. The surface of the activated carbon binds molecules from the gas phase by physisorption and chemisorption resulting in a high concentration at the interface (Ruthven, 1984). Activated carbon monoliths are suitable adsorbents of pollutants from gaseous streams due to the fact that the size and distribution of the pores within the carbon structure can be tailored through the manufacturing process to meet the requirements of promising markets (Gadkaree, 1998; Lee, *et al.*, 2000; Yates, *et al.*, 2000; Crittenden, *et al*., 2001; Botas Echevarria, *et al.*, 2003; Fuertes, *et al.*, 2003; Lapkin, *et al.*, 2004; Valdés-Solís, *et al.*, 2004; Crittenden, *et al*., 2005a).

Monoliths comprise solid integral bundles of channels that resemble a honeycomb structure, as illustrated in Figure 6. In cross section, the channels may be hexagonal, circular, square, triangular, *etc*, as demonstrated in Figure 7.

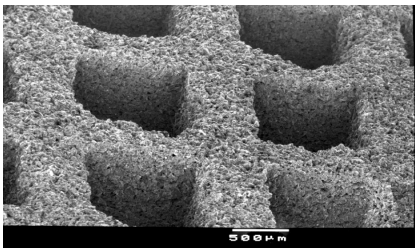

Figure 6. Honeycomb structure (Crittenden, *et al*., 2005a)

Figure 7. Activated carbon monolith (Crittenden, *et al.*, 2005b)

The internal structure of the monolithic channel wall is presented in Figure 8. The wall structure is formed of macro-particles, which in turn are composed of micro-domains. The polluted air flows in the gas channels, and the pollutant is adsorbed onto the wall structure where the adsorbent molecules are diffused. For low concentration VOCs, adsorption is predominantly attained in the micropores (< 2 nm) because of the relations among the attractive forces within the porous wall structure.

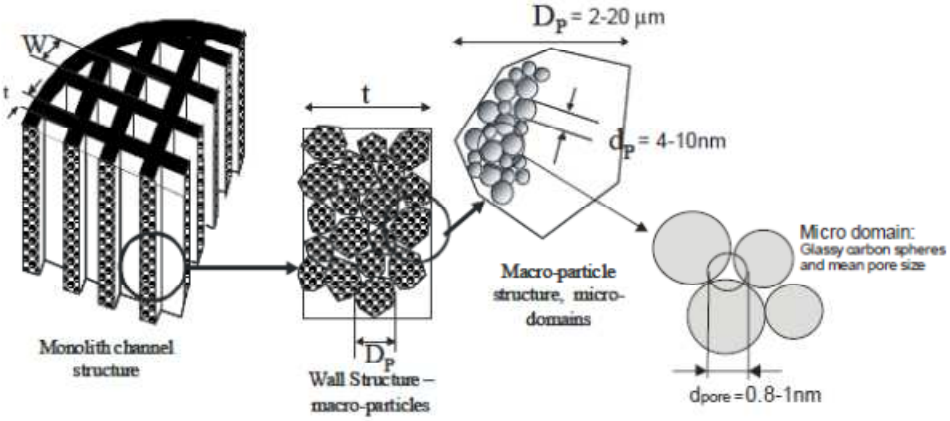

Figure 8. Monolith channel structure (Crezee, *et al*., 2005)

The geometry of the monolithic structures is categorized by three primary parameters, which are the form of the channels, the channel dimension and the wall width. Secondary factors, subsequently, are the cell density, the surface area and the

porosity, and these secondary parameters are calculated from the primary ones (Crittenden, *et al.*, 2005b). The primary parameters are illustrated in Figure 9.

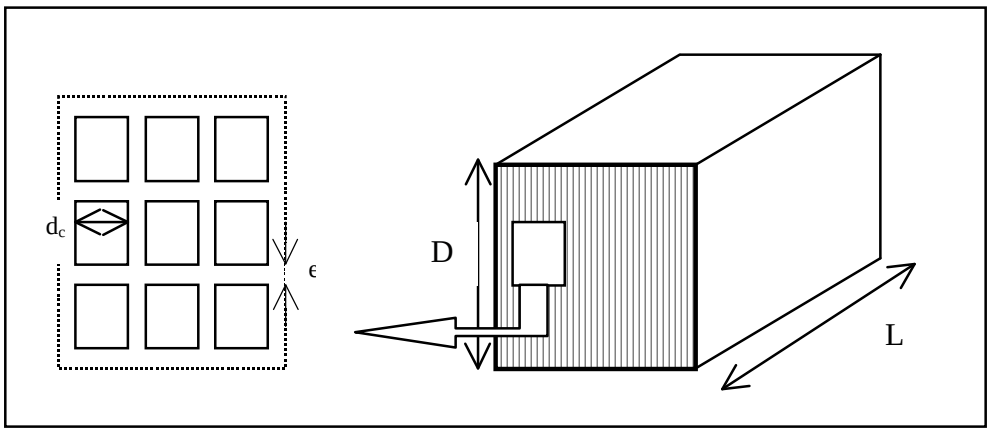

Figure 9. Monolithic primary parameters (Crittenden, *et al*., 2005b)

In addition to their high micro-porosity, activated carbon monoliths conduct electricity due to their continuous carbon skeletons and therefore can be heated more quickly for regeneration than by using convective heating from hot gases. Carbon monoliths, as a result, are being studied as a new generation of regenerable adsorbents. As can be seen in Figure 10, ACMs can be assembled to be electrically heated for regeneration in the desorption step to be used for subsequent adsorption.

The adsorption properties of the monoliths are influenced by both their binder content and their level of activation. Some ACMs have no binders, and that is the case for the monoliths studied in the current research. The monolith's density determines the electrical resistance, and hence the efficiency with which it can be heated for regeneration.

Figure 10. ACMs assembled into a module and electrically connected (Crittenden, 2011)

3.1. Monoliths vs. granules

The performance of the two forms of activated carbon, namely monoliths and a packed bed of pellets, can be compared. Several advantages of monoliths with regard to packed beds were noted (Crittenden, *et al*., 2005a; Valdés-Solis, *et al*., 2001; Crezee, *et al*., 2005; Li, *et al*., 1998b; Yates, *et al*., 2003).

Monoliths offer considerable reductions in pressure drop over their packed bed equivalents. The laminar flow of the gas passing through the monolith channels has a pressure drop advantage over the twisting passage of gas around adsorbent granules. Crittenden, *et al*. (2005a) demonstrated the possibility of manufacturing an activated carbon monolith with a capacity and mass transfer capability similar to an equivalent bed of granules having the same mass but with a pressure drop of only 6% of its equivalent bed of granules. Yates, *et al*. (2003) estimated a null pressure drop in the monolith adsorption bed caused by the open channel structures. Li, *et al*. (1998b) found that the pressure drop through a monolith was 3-5 times beneath that through its equivalent packed bed, and consequently the time required to pressurize the monolith was 3 - 5 times faster than that needed to pressurize the bed of pellets. Crezee, *et al*. (2005) demonstrated that the adsorption performance of the monoliths is close to that of an equivalent packed bed of spherical carbons but with $1/100^{th}$ of the pressure drop.

In addition to the negligible pressure drop that they create, another advantage of monoliths in comparison to packed beds is their superior resistance to abrasion. Monoliths also can be positioned in upright or horizontal arrangements or in moving setups without losing their forms. They are, additionally, simpler to deal with than packed beds.

Activated carbon monoliths which are electrically conducting can be regenerated with an order of magnitude faster than packed bed systems. The unique electrically conducting monolithic activated carbons that can be heated rapidly to the required regeneration temperature (150 - 200 ºC) allow cycle times of tens of minutes rather than the hours associated with conventional granular adsorbent beds. This results in an estimated 30 fold reduction in bed size with an associated reduction in energy demand of up to 10 fold. The small size of the units, the elimination of steam as the regenerant, and the low energy demand, will allow these units to be placed close to the source of the VOCs, rather than as an end of pipe treatment, which will then allow the direct recovery and recycle of the solvents (Crezee, *et al.*, 2005).

An additional advantage of monoliths over their counterpart granular packed beds is the monolithic activation process which advantageously creates micro-porous voidage, in contrast to the activation process utilised for packed beds. For ACMs, adsorption for low VOC concentration gases mostly takes place in the micropores (Valdés-Solis, *et al*., 2001). The activation method of the granular packed beds creates a fairly broad pore size distribution with sizes ranging from micropores (< 2 nm) to mesopores (2 – 50 nm).

Activated carbon monoliths provide capacity and kinetic properties that measure up well to the same mass of their granular counterparts based on the study of internal and external mass transfer coefficients. Therefore, the potential commercial, environmental, and health protection advantages of switching from packed beds to monolithic adsorbents seem to be favourable (Crittenden, *et. al*., 2005a).

3.2. Activated carbon monolith production

Activated carbon monoliths can be produced in a number of ways. Gadkaree (1998) and Valdés-Solís, *et al.* (2004) carbonised phenolic resin which had been

impregnated or dip-coated, respectively, on ceramic honeycomb supports, whilst Fuertes, *et al.* (2003) carbonised polymeric fibres. Yates, *et al.* (2000), on the other hand, extruded a mixture of silicate clay with activated carbon, a monolith type used by Yu, *et al.* (2002). Binder-less activated carbon monoliths, known as NovaCarb, are made by MAST Carbon Ltd from phenolic resin. They are produced via the sequential steps of resin curing, resin extrusion, carbonisation and activation (Tennison, *et al.*, 2001; Place, *et al.*, 2004; Crezee, *et al.*, 2005).

The procedure followed by Valdés-Solis, *et al*. (2001) for preparing carbon–ceramic monoliths consisted of dip-coating the ceramic monoliths in a phenolic novolac resin, disposing of the surplus impregnation solution, air curing and carbonizing. The cycle of dip-coating, curing and carbonizing was conducted twice to get a monolith with a superior quantity of carbon. The carbonized substance was then activated by steam to reach its highest adsorption capacity. The highest adsorption capacity was attained at an activation level of 30 wt%.

Yates, *et al.* (2000) prepared their monolith composites by mixing commercially available micro-porous activated carbons with a silicate clay binder. After mixing the dry powder with water, the blend was moulded into dough, which in turn was extruded into monoliths. The monoliths were then dried, heated and further heat-treated.

Rosas, *et al*. (2008) obtained activated carbon monoliths by the activation of hemp canes with phosphoric acid. The surface characteristics of the activated carbons were found to be greatly related to the carbonization temperature and the impregnation ratio.

3.3. Overview of MAST carbon monoliths manufacturing

The carbon monoliths NovaCarb used in this study have been supplied and manufactured by MAST Carbon Technology Ltd. These monoliths are fashioned in various lengths, diameters, channel shapes and cell densities. The manufacturing process is summarized in the subsequent sections and mainly involves resin curing, extrusion, carbonization and activation (Tennison, 1998). The overall process is divided into cold steps of curing, milling and extruding followed by hot steps of carbonization and

activation. The precursor material is phenolic resin, type Novolak produced by the polymerization reaction of phenol with formaldehyde under acidic conditions (pH 1 - 4).

3.3.1. Curing

In polymer chemistry, curing translates into the strengthening or the hardening of polymeric material by cross-linking of the polymer chains, due to chemical additives and or heat. The phenolic resin, a thermoplastic polymer, is cured by the addition of a curing agent (hardener) under thermal treatment and thereby is transformed into a highly cross linked resin.

The curing process is critical because temperature and time must be controlled to obtain a structure capable of resisting the subsequent thermal steps. If the resin is over cured then it tends to harden, and if it is under cured it melts. The ideal cure creates the adequate internal open porosity of the macrostructure.

3.3.2. Milling

The cured resin produces a solid "biscuit" which is first hammer milled to grain size and further milled to produce fine powder with the desired macropore structure. The second milling stage is carried out in a jet mill to minimize the presence of large particles. The milled powder is then moistened by the addition of lubricants and de-ionized water to be converted into dough for extrusion. A milling process is used to control the particle size, which is essential in creating the net pore structure, as shown in Figures 8 and 11. Macropores are created by the union of the largest phenolic resin particles exhibiting a mean particle size in the order of 10 – 70 μm giving rise to macropores with a mean macropore size in the range 2 - 20 μm. Microdomains, on the other hand, are formed by the union of the smallest micro sphere resins with a particle diameter of around 4 – 10 nm forming micropores of 0.8 to 1.0 nm in size (Sánchez-Liarte, 2009).

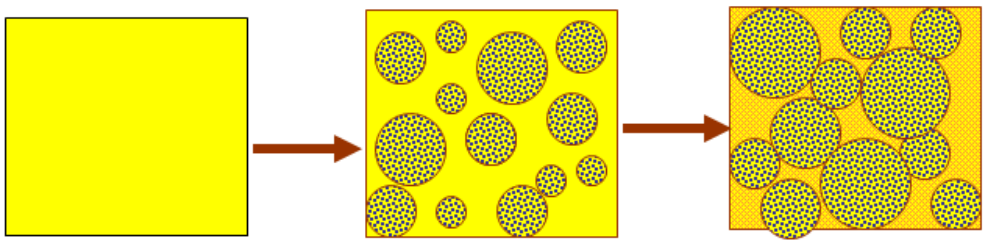

Figure 11. Net pore structure (Crittenden, 2011)

3.3.3. Extruding

The dough is sintered without the use of any binder. Powder sintering or sticking together is driven by pressure and moisture. This process is carried out by extrusion, whereby the powder is pushed through a die such as the ones presented in Figure 12, and the body of the monolith is shaped in the desired form. The rheology and the pressure applied are critical to the developing form. This is then said to be the unfired “green” state of the monolith, having a yellowish red colour arising from the colour of its phenolic precursor.

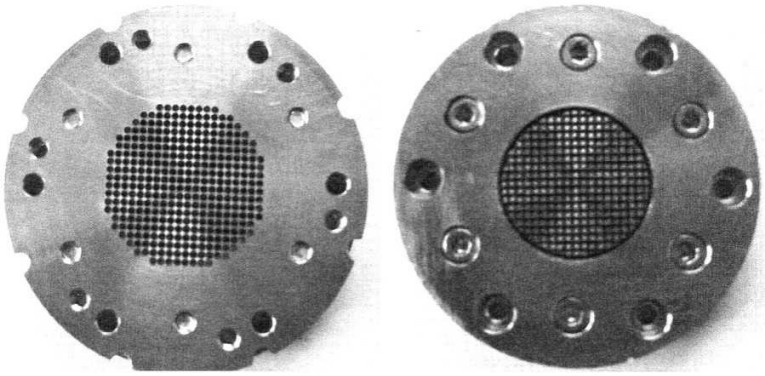

Figure 12. Dies for extrusion (Sánchez-Liarte, 2009)

3.3.4. Carbonization

The "green" body is then subjected to carbonization, where its yellowish red colour turns black. The carbonization process transforms the porous resins into the porous carbons and is usually carried out at 800ºC using a CO_2 stream. During this

process, the resin loses around 45% of its weight due to the removal of retained water and hydrocarbons from its structure, as illustrated in Figure 13. Carbonization of the high density cross-linked domains formed during curing results in glassy spherical carbon particles, and the low cross-linked density resins decompose into amorphous carbons.

Figure 13. Green and carbonised monoliths (Crittenden, 2011)

3.3.5. Activation

The activation process controls the pore size distribution. The carbonized monoliths are activated at 900ºC using a CO_2 stream in order in increase their surface areas. Crucial parameters, such as CO_2 flow rate, temperature and duration, are controlled to obtain the desired grade of activation and thereby the required pore structure. Finally, the activated monoliths are wrapped using a super-wool blanket to avoid any over-oxidation of the surface (Crezee, *et al.*, 2005).

3.4. Activated carbon monolith applications

There is an increasing interest in the use of monoliths as adsorbent devices. Potential applications include:

1 VOC control (Gadkaree, 1998; Lee, *et al.*, 2000; Yates, *et al.*, 2000; Yu, *et al.*, 2002; Botas Echevarria, *et al.*, 2003; Fuertes, *et al.*, 2003; Crittenden, *et al.*, 2001; Valdés-Solís, *et al.*, 2004, Yu, *et al*., 2007).

2 Air separation (Burchell, *et al.*, 1997; Li, *et al.*, 1998a). Onyestyak, *et al.* (2004) tested a honeycomb monolith that demonstrated sorption capacity and N_2/O_2

selectivity for air separation processes. The micropore diffusion of N_2 and O_2 was found to affect the process of mass transport in the adsorbent monolith.

3 Recovery of CO_2 from combustion gases (Brandani, *et al.*, 2004). Grande and Rodrigues (2008) proposed a mechanism that can be used to capture the carbon dioxide from flue gas streams containing low concentrations of CO_2 utilizing an activated carbon monolith.

4 Methane storage. Lozano-Castello (2002) studied the adsorption capacity of activated carbon monolith and noted that the monolith density was a critical factor for methane storage applications.

In addition, activated carbons are becoming important in heterogeneous catalysis, either as catalyst supports or as catalysts by themselves. Activated carbons are employed as three-way catalysts for the control of pollution from cars, and more recently as catalytic devices in multiphase flow and multifunctional reactors (Irandoust & Andersson, 1988; Kapteijn, *et al.*, 1999; Lebens, 1999; Nijhuis, *et al.*, 2001a, b). Carbon monoliths, when loaded with an appropriate catalyst, are extremely efficient in increasing chemical reaction rates. This is accomplished not only by the high surface area of the monoliths, but also by taking full advantage of the laminar flow characteristics associated with the parallel micro-channels. Opportunities exist in applying this technology to existing fuel reforming/processing systems and indeed wherever a catalyst support is required.

As demonstrated, ACMs are very useful adsorbents in many industrial applications as they meet the needs of emerging markets. Their main use, however, is the removal of impurities from gases through the adsorption process. Activated carbon monoliths have been utilized to absorb VOCs from air streams, and this is the application studied in this thesis.

3.5. References

Botas Echevarria, J.A., Perera, S. P. & Crittenden, B.D., 2003. Monolithic adsorbents, a comparison with their particulate counterparts. *4th European congress of Chemical Engineering*, Granada, Spain 21 - 25 September 2003.

Brandani, F., Rousse, A., Brandani, S. & Ruthven, D.M., 2004. Adsorption Kinetics and Dynamic Behavior of a Carbon Monolith. *Adsorption,* 10, pp.99-109.

Burchell T. D., Judkins, R.R., Rogers, M.R. & Williams, A.M., 1997. A novel process and material for the separation of carbon dioxide and hydrogen sulphide gas mixtures. *Carbon,* 35, pp.1279-1294.

Crezee, E., Tennison, S. R., Rawling, A. P., Place, R.N., Crittenden, B. D. & Perera, S. P., 2005. Electrically regenerable carbon monolithic adsorption system for the recovery and recycle of volatile organic chemicals (VOCs). *In: World Congress of Chemical Engineering, 7th,* July 10 - 14, 2005, Glasgow, United Kingdom.

Crittenden B. D., Perera S. P., Lee L. Y. & Gómez Crespo A., 2001. Monolithic adsorbents in environmental protection, *Proc of the 9th International summer school of chemical engineering*, Sozopol, Sapundzhiev, Ts. (Ed.), Bulgarian Academy of Sciences, Sofia, pp.247-267.

Crittenden, B. D., 2011. *Discussion on ACM* [email] (Personal communication, 5 December 2011).

Crittenden, B. D., Patton, A., Jouin, C., Perera, S. P. & Tennison, S., 2005a. Carbon Monoliths: a comparison with Granular materials. *Adsorption*, 11, pp.537-541.

Crittenden, B., Perera, S., Mays, T., Camus, O. & Tennison, S., 2005b. Monolithic adsorbents in sustainable development. *In*: *world Congress of Chemical Engineering, 7th*, 10 - 14 July, Glasgow.

Fuertes, A. B., Marban, G. & Neveskaia, D. M., 2003. Adsorption of volatile organic compounds by means of activated carbon fiber-based monoliths. *Carbon,* 41, pp.87-96.

Gadkaree, K. P., 1998. Carbon honeycomb structures for adsorption applications. *Carbon*, 36, pp.981-989.

Grande, C. A, & Rodrigues, A. E., 2008. Electric swing adsorption for CO2 removal from flue gases. *International Journal of Greenhouse Gas Control*, 2(2), pp.194-202.

Irandoust, S. & Andersson, B., 1988. Mass transfer and liquid-phase reactions in a segmented two-phase flow monolith catalytic reactor. *Chemical Engineering Science,* 43, pp.1983-1988.

Kapteijn, F., Heiszwolf, J. J., Nijhuis, T. A. & Moulijn, J. A., 1999. Monoliths in multiphase catalytic processes. *CATTECH*, 3(1)**,** pp.24-41.

Lapkin, A., Joyce, L. & Crittenden, B. D., 2004. Framework for evaluating the "greenness" of chemical processes: case studies for a novel VOC recovery technology. *Environment Science Technology*, 38, pp.5815-5823.

Lebens, P.J., 1999. *Development and design of a monolith reactor for gas–liquid countercurrent operation*. Doctoral Dissertation, Delft University of Technology.

Lee, L. Y., Perera, S. P., Crittenden, B. D. & Kolaczkowski, S. T., 2000. Manufacture and characterization for silicate monoliths. *Adsorption Science and Technology*, 18, pp.147-170.

Li, Y. Y., Perera, S. P. & Crittenden, B. D., 1998b. Zeolite monoliths for air separation, Part 2: Oxygen Enrichment, Pressure Drop and Pressurization. *Chemical Engineering Research and Design, Special issue: Separation Processes*, 76, pp.931-941.

Li, Y. Y., Perera, S. P., & Crittenden, B.D., 1998a. Zeolite monoliths for air separation, Part 1: Manufacture and characterization. *Trans IChemE*, 76 (Part A), pp.921-930.

Lozano-Castello, D., Cazorla-Amoros, D., Linares-Solano, A. & Quinn, D. F., 2002. Influence of pore size distribution on methane storage at relatively low pressure: preparation of activated carbon with optimum pore size. *Carbon*, 40, pp.989-1002.

Nijhuis, T. A., Beers, A. E. W., Vergunst, T., Hoek, I., Kapteijn, F. & Moulijn, J. A., 2001a. Preparation of monolithic catalysts, Catalysis Reviews. *Science and Engineering*, 43(4), pp.345-380.

Nijhuis, T.A., Kreutzer, M. T., Romijn, A. C, J., Kapteijn, F. & Moulijn, J. A., 2001b. Monolith catalysts as efficient three-phase reactors. *Chemical Engineering Science*, 56 (3), pp.823-829.

Onyestyak, G., Rees, L. V. & Laszlo, K., 2004. Molecular-Sieve Honeycomb for Air Separation from Picea abies. *Helvetica Chimica Acta*, 87(7), pp.1888-1893.

Place, R. N., Blackburn, A. J., Tennison, S. R., Rawlinson, A. R., Kozynchenko, O. P. & Crittenden, B. D., 2004. Method and equipment for removing volatile compounds from air. WO 02072240 to Carbon Technologies N.V.

Rosas, J.M., Bedia, J., Rodríguez-Mirasol, J. & Cordero, T., 2008. Preparation of Hemp-Derived Activated Carbon Monoliths. Adsorption of Water Vapour. *Industrial & Engineering Chemistry Research, 47* (4), pp.1288-1296.

Ruthven, D. M., 1984. *Principles of adsorption & adsorption processes*. John Wiley & sons, Inc.

Sánchez-Liarte, F., 2009. *Performance of electrically regenerable monolithic adsorbents for VOC control*. Ph.D. thesis: University of Bath.

Tennison, S.R., 1998. Phenolic-resin-derived activated carbons. *Applied Catalysis,* 173, pp.289- 311.

Tennison, S.R., Blackburn, A., Rawlinson, A., Place, R., Crittenden, B.D., & Fair, S., 2001. Electrically regenerable monolithic adsorption system for the recovery of solvent vapours, *AIChE Spring Meeting*.

Valdés-Solís, T., Linders, M., J. G., Kapteijn, F., Marban, G. & Fuertes, A. B., 2004. Adsorption and breakthrough performance of carbon-coated ceramic monoliths at low concentration of *n*-butane. *Chemical Engineering Science***,** 59(13), pp.2791-2800.

Valdés-Solis, T., Marban, G. & Fuertes, A. B., 2001. Preparation of microporous carbon-ceramic cellular monoliths. *Microporous and Mesoporous Materials*, 43, pp.113-126.

Yates, M., Blanco, J., Avila, P. & Martin, M. P., 2000. Honeycomb monoliths of activated carbons for effluent gas purification. *Microporous and Mesoporous Materials*, 37, pp. 201-208.

Yates, M., Blanco, J., Martin-Luengo M. A. & Martin, M. P., 2003. Vapour adsorption capacity of controlled porosity honeycomb monoliths. *Microporous and Mesoporous Materials*, 65(2-3), pp.219-231.

Yu, F. D., Luo, L. A. & Grevillot, G., 2002. Adsorption Isotherms of VOCs onto an Activated Carbon Monolith: Experimental Measurement and Correlation with Different Models. *Journal of Chemical Engineering Data*, 47 (3), pp.467-473.

Yu, F. D., Luo, L. A. & Grevillot, G., 2007. Electrothermal swing adsorption of toluene on an activated carbon monolith: Experiments and parametric theoretical study. *Chemical Engineering and Processing: Process intensification*, 46 (1), pp.70-81.

Chapter 4

Modelling

Mathematical modelling and simulation constitute the heart of this project. Modelling the adsorption and desorption of VOCs from polluted air stream onto activated carbon monoliths is the subject of this study. Mathematical modelling of the adsorption and desorption is performed based on established modelling equations using appropriate modelling software.

4.1. Adsorption/desorption

Adsorption of VOCs from polluted air onto activate carbon monoliths is followed by a desorption step to recover the VOCs and regenerate the monoliths for reuse. The adsorption/desorption process form a cycle that can be repeated several times. Figure 14 shows a schematic diagram of the cyclic adsorption/desorption process, where adsorption of VOCs onto the activated carbon monoliths takes place in a freshly regenerated monolithic column while the used column is regenerated by heating in the subsequent desorption step.

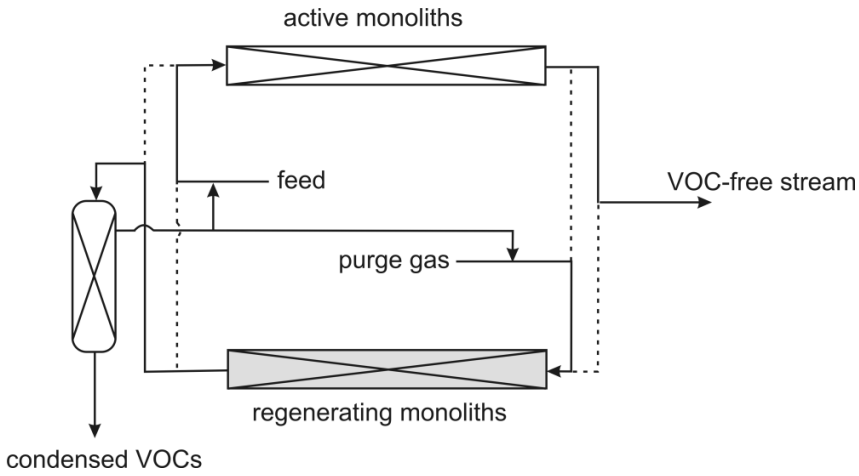

Figure 14. Schematic diagram of adsorption/desorption process (Place, *et al.*, 2005)

4.1.1. Adsorption methods

Adsorption of VOCs onto activated carbons is known to remove pollutants to virtually non-detectable levels (Shepherd, 2001) Adsorption is effective for single component removal as well as for mixtures of pollutants (Yu, *et al.*, 2002). In comparison to other technologies covered in an earlier Chapter, this technology had been considered the least expensive. It is simple to apply and operate and is mainly used in the treatment of off- gases from work areas or plants. VOC molecules attract and accumulate on the large surface area of the activated carbon monoliths. The adsorption process is most effective for high molecular weight and high boiling point VOCs. In general also, ACMs manufacturing, detailed in the previous Chapter, governs the adsorption selectivity.

4.1.2. Regeneration methods

In the chemical process industry, adsorption based processes are governed by the regeneration of the adsorbent. This regeneration step is time and energy consuming in comparison to the adsorption step. Two well-known regeneration methods are mainly utilized, and these are pressure swing adsorption (PSA) and temperature swing adsorption (TSA). PSA is suitable for weak adsorbates while TSA works better for stronger

adsorbed species. Also, PSA operates at high pressure during adsorption and low pressure during desorption. TSA processes, on the other hand, work at a reduced temperature during adsorption and an elevated temperature during desorption.

In a PSA system, regeneration is attained by decreasing the pressure. The adsorbed species is adsorbed onto the adsorbent at a high partial pressure and then desorbed at an inferior partial pressure. In order to adjust the partial pressure of the adsorbed species, the total pressure or the composition of the gas mixture can be manipulated. In the alternative TSA process, the adsorbent bed is heated by a hot gas or steam to desorb the adsorbed species and so regenerate the adsorbent bed. Once the bed is regenerated, it is cooled down for the next adsorption step to take place.

PSA and TSA have their distinctive advantages and disadvantages. TSA requires heat to regenerate the adsorbent bed; therefore, this process is energy intensive. While the PSA system does not require a high operating temperature, its characteristic short cycle time has a drawback. For the cyclic process, adsorption is followed by depressurization for regeneration and then repressurization to close the cycle. The gas feed is lost to the vent during the depressurization step. The short cycle time gives rise to this loss of feed gas. Therefore, repressurization should be conducted quickly to save the gas feed. This rapid process introduces instability in plant operation caused by the transitory deviations in the feed and product flow rates (Wright, *et al*., 2005).

The TSA process is generally more favourable than the PSA process for fluid purification, but still this process has a number of disadvantages. TSA requires a large amount of hot gas to regenerate the adsorbent bed. It has a long cycle time in comparison with PSA, as the heating and cooling steps are time consuming. Typical TSA cycles take hours while PSA requires minutes. Furthermore, the purge gas introduced during the regeneration step in TSA recovers the desorbed species in a diluted form.

4.1.3. Models of TSA cycles

With the goal of overcoming the disadvantages of TSA and PSA processes, research on novel regeneration techniques is developing, such as hybrid regeneration

cycles, heating through a peripheral heater, direct heating with an in-bed heat exchanger, electrothermal heating, etc.

For example, Wright, *et al*. (2005) developed a hybrid regeneration cycle known as temperature-pressure swing adsorption (TPSA) joining mutual PSA and TSA advantages but at the same time reducing their coupled expenses. The proposed TPSA process, similarly to TSA, needs to increase the temperature of the adsorbing bed for regeneration. The required heat for TPSA, however, is less than that needed for TSA. TSPA proposes thermal energy saving and considerable power reductions with no transient operating difficulties arising from the rapid cycle time.

Menard, *et al*. (2007) focused on thermal regeneration by means of an external heat exchanger. This regeneration methodology is more favourable than the use of a hot purge gas to regenerate the adsorbent bed. The purge gas dilutes the desorbed species.

Clausse, *et al*. (2004) and Bonjour, *et al.* (2005) investigated both numerically and experimentally the performance of the TSA process to purify polluted gases using an internal heat-exchanger for indirect heating and cooling. The authors highlighted the behaviour differences between an indirectly heated or cooled TSA adsorber and other adsorbers classified as adiabatic, near-adiabatic and isothermal. It was also shown that for a scaled-up adsorber, heat utilization was similar to normal TSA processes.

The initiative to regenerate the adsorbent bed by the mean of direct heating with electric current became public in the 1970s (Fabuss & Dubois, 1970). This regeneration process was referred to as "electrothermal" desorption, and it was known to be an effective approach to conduct desorption in a TSA cycle. Electrothermal swing adsorption (ESA) is a rather recent process (Sullivan, *et al*., 2004; Yu, *et al*., 2007) for basically a TSA cycle. The adsorbent bed in ESA is desorbed by flowing current through it thereby generating heat by the Joule effect. The ESA process is basically a TSA process where the heat source to regenerate the adsorbent bed is different. In TSA, a hot gas stream is usually used for heating the adsorbent bed, while in ESA the adsorbent bed is heated using the Joule effect by having electricity flowing through the adsorbent bed to increase its temperature.

A good example to compare the ESA and TSA processes is the abatement of VOCs. ESA has a better efficiency than TSA (Saysset, *et al*., 1999; Sullivan, 2003; Yu,

et al., 2007). The major divergences between ESA and TSA processes are as follows (Petkovska, *et al*., 2007; Burchell, *et al*., 1997; Saysset, *et al*., 1999; Yu, *et al.*, 2002; Sullivan, 2003; Crezee, *et al.*, 2005):

- The energy effectiveness is higher in ESA than TSA, since the energy for adsorbent regeneration is inputted straight into the adsorbent by passage of a current at low potential difference, thereby minimizing the energy spent to heat the column and its auxiliary equipment.
- The rate of heat introduced into the adsorbent bed of an ESA process is not a function of the heating gas stream but is directly related to the adsorbent bed itself as the heat is directly introduced into the bed.
- The adsorbate concentration is no longer diluted by the heating gas steam in the ESA process. The adsorbate concentration in the effluent stream is only affected by the purge gas flow rate regardless of the energy needed to heat the adsorbent bed.
- No water is used in an ESA process in comparison with the use of steam heating in a TSA process. Thereby corrosion and expensive water/steam handling systems are avoided in ESA.
- Heat and mass transfer are concurrent in ESA and counter current in TSA affecting the overall process kinetics.

Petkovska, *et al.* (2005, 2007) conducted a project for mathematical modelling of a TSA system with an electrothermal desorption step. The developed models described adsorption, electrothermal desorption and electrothermal desorption accompanied by condensation of the desorbed vapour, as well as the complete TSA cycle. These models were used for the prediction of velocity, pressure, concentration and temperature profiles in the adsorbers. The models are also used in calculation of the amount of collected liquid and electrical power utilized. In a later work, Petkovska, *et al.* (2007) presented a mathematical model of an ESA system with fixed-bed and in-vessel condensation. Mathematical modelling was conducted using COMSOL commercial software. Three models were developed to present the three steps of the complete ESA cycle: adsorption, desorption with and without condensation. The three developed models were integrated

using COMSOL Multiphysics and Matlab. These models were effectively utilized to replicate the three steps of the ESA cycle and then to simulate the overall ESA cycle. The influence of operating conditions was also investigated to evaluate process performance.

Yu, *et al*. (2002, 2007) regenerated the carbon monolith by heating carbon by the Joule effect. A number of parameters were studied experimentally and via modelling and simulation, especially since the process performance was heavily dependent on the operating conditions. The conductivity of the monolith decreased with increasing temperature and increasing the amount adsorbed onto it. The concentration of the desorbed VOC peaked upon initial desorption then decreased over time. The initial concentrations increased with current intensity and purge gas flow in a linear fashion and were also augmented with the duration of preheating. The purge gas flow rate diluted the desorbed VOC. Desorption efficiency represented by the percentage of desorbed VOC was not affected with varying preheating times but increased with the applied current and the purge gas flow rate.

4.2. Electrothermal swing adsorption (ESA)

Fundamental aspects of the ESA process for adsorption and desorption concern thermodynamics and kinetics. The thermodynamic approach studies adsorption equilibrium. The rate of adsorption and desorption in porous adsorbents, which is generally controlled by mass and heat transfer, takes into consideration the overall adsorption kinetics.

4.2.1. Adsorption equilibrium

Adsorption equilibrium relates the concentration in the gas phase to the concentration on the solid and is usually described by isosteres, isobars or isotherms. As their names imply, isosteres, isobars and isotherms describe the relation between adsorbent and adsorbate as functions of constant loading, pressure and temperature, respectively. Adsorption isosteres relate the equilibrium pressure to the temperature at

constant amount of adsorbent to adsorbate. Adsorption isobars, on the other hand, relate the amount of adsorbate on adsorbent to temperature at constant pressure. Finally, adsorption isotherms relate the adsorbate concentration on the adsorbent to its partial pressure at fixed temperature.

Commonly, isotherms are used to describe adsorption equilibrium. Six different types of isotherms describing gas-solid equilibrium are generally encountered, as classified by the International Union of Pure and Applied Chemistry (IUPAC). The isotherms are shown in Figure 15. The type I isotherm depicts monolayer adsorption and characterizes microporous adsorbents. The type II isotherm portrays the adsorption onto macroporous adsorbents with strong adsorbate-adsorbent interactions. The type III isotherm shows the formation of multilayers and describes macroporous adsorbents with weak interactions between adsorbent and adsorbate. Type IV and Type V isotherms describe adsorption with hysteresis and characterize mesoporous adsorbents with strong and weak attractions, respectively. Hysteresis shows a deviation between input and output. The type VI isotherm represents a stepwise multilayer adsorption. Gas-solid adsorption/desorption of VOCs on activated carbon monolith can be described by a very large number of isotherm equations of which only Langmuir, Freundlich and Tóth isotherms are presented now in their order of complexity.

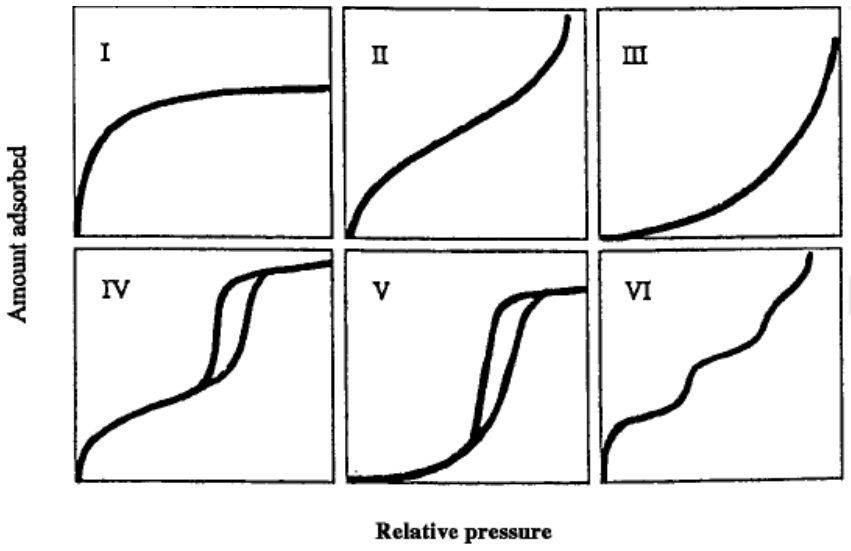

Figure 15. IUPAC classification for adsorption isotherms (IUPAC, 1985)

4.2.1.1. Langmuir equation

The Langmuir adsorption isotherm (Langmuir, 1916) demonstrates the increasing amount of adsorbate onto the adsorbent surface as a function of partial pressure. The isotherm is a curve in a form that gradually increases and then levels off at a fixed value of loading on the solid.

According to Yu, *et al*. (2002), the Langmuir isotherm equation is stated as:

$$q = q_m \frac{bp}{1+bp} \qquad \text{(eq. 1)}$$

where

q	=	amount of VOC adsorbed, mol kg $^{-1}$
q_m	=	maximum amount adsorbed, mol kg $^{-1}$
b	=	affinity coefficient, Pa^{-1}
p	=	partial pressure, Pa

The affinity coefficient is presented in the van't Hoff equation:

$$b = b_0 \exp\left(\frac{-\Delta H_{ads}}{RT}\right) \qquad \text{(eq. 2)}$$

where

b_0	=	affinity parameter, Pa^{-1}
$-\Delta H_{ads}$	=	isosteric heat of adsorption, J mol^{-1}
R	=	ideal gas law constant, m^3 Pa K^{-1} mol^{-1}
T	=	temperature, K

The Langmuir isotherm model is mainly compatible with monolayer coverage on a homogeneous adsorbent with minor intermolecular interactions.

Many adsorption processes are well described by the Langmuir isotherm. However, for many systems the Langmuir isotherm is not appropriate. For example, Figure 16 represents experimental vs. Langmuir adsorption isotherms in solid lines for toluene at four different temperatures (20, 60, 100 & 140ºC) (Yu, 2003).

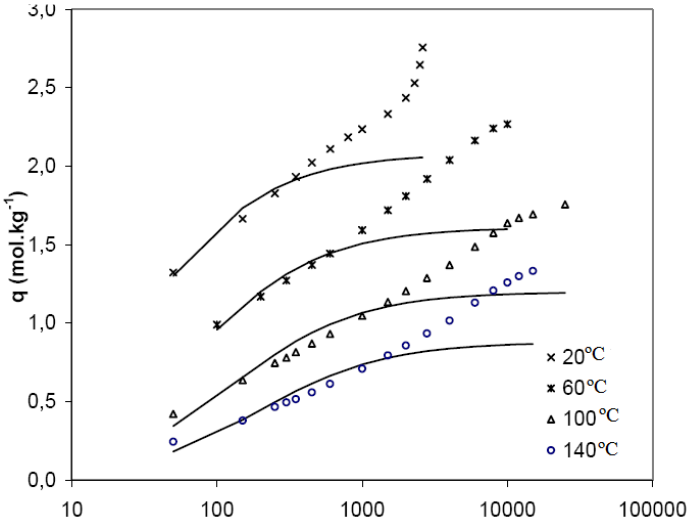

Figure 16. Experimental vs. Langmuir adsorption isotherms for toluene (Yu, 2003)

The Langmuir isotherm equation leads to two limiting conditions depending upon the pressure. At very low pressure, Henry's law can be deduced, when the amount adsorbed increases linearly with partial pressure. At high pressures, the saturation capacity of the monolayer is reached, corresponding to the total coverage of all the adsorption sites ($q = q_m$) where adsorption is independent of pressure (Bansal & Goyal, 2005).

4.2.1.2. Freundlich equation

The Freundlich equation (Freundlich, 1924) relates a species' concentration onto the adsorbent surface to its concentration in the fluid in which it is diluted. This equation is commonly used in the description of adsorption of organics systems onto heterogeneous surfaces. The Freundlich isotherm as described by Yu, *et al*. (2002) is:

$$q = kp^n \qquad \text{(eq. 3)}$$

where

q = amount of VOC adsorbed, mol kg $^{-1}$

k = constant for an adsorbate and an adsorbent at a fixed temperature, (units depend on the value of n)

p = partial pressure, Pa

n = constant for an adsorbate and an adsorbent at a fixed temperature.

This model is normally suitable for a large number of adsorption data but with narrow range, since this equation is not adequate for low and high pressures. Figure 17 represents experimental vs. Freundlich adsorption isotherms for toluene at four different temperatures (Yu, 2003). As can be seen in Figure 17, the modelled Freundlich isotherms fit the experimental data much better than the Langmuir isotherms presented in Figure 16 for the same set of experimental data.

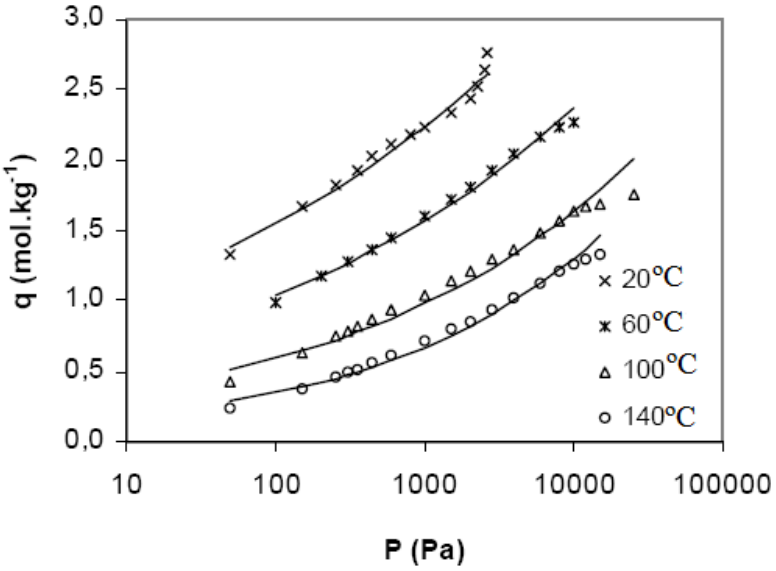

Figure 17. Experimental vs. Freundlich adsorption isotherms for toluene (Yu, 2003)

4.2.1.3. Tóth equation

The Tóth model (Tóth, 1962) is frequently used to represent isotherm data on heterogeneous adsorbents such as activated carbon. Yu, *et al.* (2002) use the Tóth equation to satisfy both low- and high-pressure ranges:

$$q = q_m \frac{bp}{[1+(bp)^t]^{(1/t)}} \qquad \text{(eq. 4)}$$

where

q = amount of VOC adsorbed, mol kg $^{-1}$

q_m	=	saturation solid loading, mol kg $^{-1}$
b	=	affinity coefficient, Pa^{-1}
p	=	partial pressure, Pa
t	=	parameter of Tóth model

The *b* and *t* parameters are explicit for certain adsorbate-adsorbent couples. The Tóth parameter is usually less than unity, and its large deviation from unity implies a strong degree of heterogeneity for the adsorption of adsorbate onto the activated carbon (Crezee, *et al*., 2005). Figure 18 represents experimental vs. Tóth adsorption isotherms for toluene at four different temperatures (Yu, 2003).

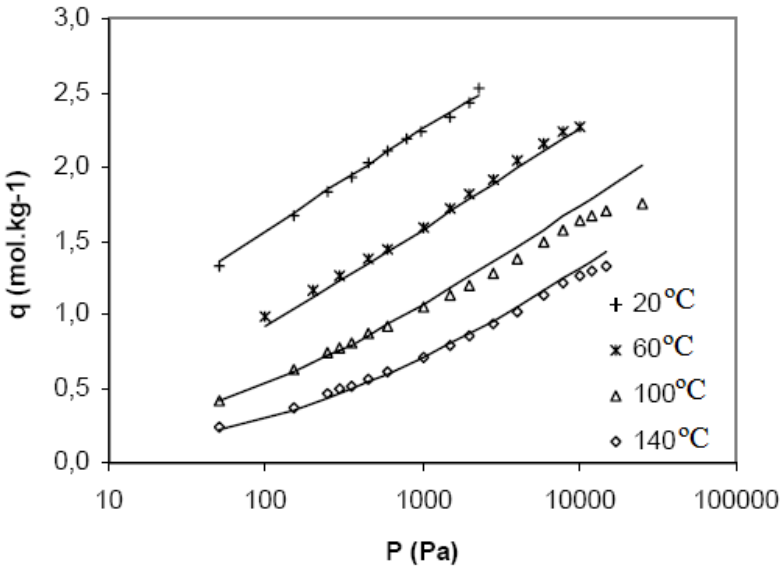

Figure 18. Experimental vs. Tóth adsorption isotherms for toluene (Yu, 2003)

Yu, *et al*. (2002) concluded that Tóth equations presented in Figure 18, in comparison to Langmuir (Figure 16) and Freundlich (Figure 17) isotherms, give a better fit for VOC adsorption onto activated carbon monolith at varying temperatures. The isotherms of toluene reveal a typical Type II shape distinctive of adsorbents having a broad range of pore sizes.

Crittenden, *et al*. (2011) also used the Tóth equation to explain the adsorption isotherm of DCM onto activated carbon monoliths, as shown in Figure 19. This figure shows that the Tóth equation provides a reasonable fit of DCM adsorption onto the

activated carbon samples at three different temperatures of 5, 10 and 20°C. The gas-solid adsorption/desorption of DCM on activated carbon monolith can be explained by a Type I isotherm which depicts monolayer adsorption and characterizes microporous adsorbents (Crittenden, *et al.*, 2011).

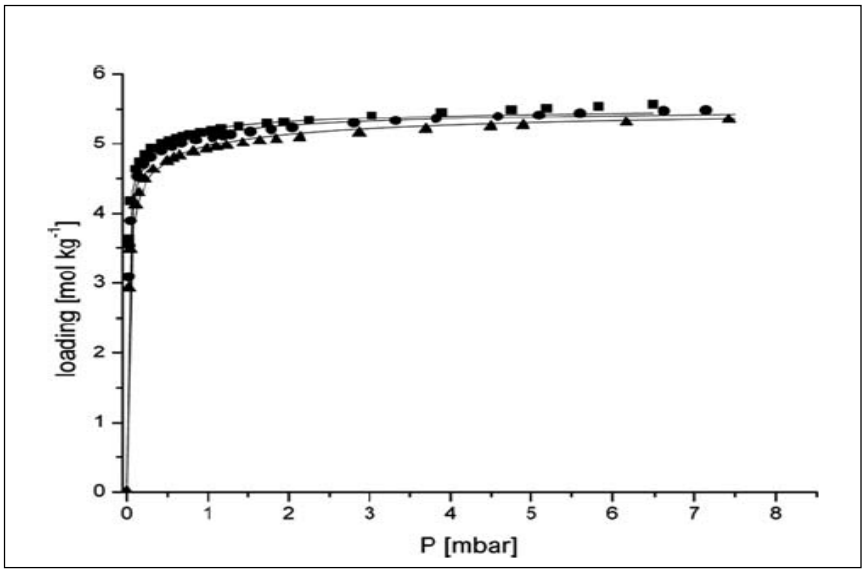

Figure 19. DCM adsorption isotherms on ACM samples at 5 (■), 10 (●) and 20 (▲)°C explained by the Tóth isotherm (solid lines) (Crittenden, *et al*., 2011)

4.2.2. Adsorption kinetics

Kinetics of adsorption is time dependant and can be determined from the breakthrough curve and viewed by the mass transfer zone. The adsorption kinetics are governed by the transport phenomena taking place, and these phenomena describe the transport of adsorbate from the carrier gas to the interior of the adsorbent.

4.2.2.1. Breakthrough curve

The breakthrough curve is a plot of adsorption column effluent concentration over time. This S-shaped curve is the relation over time of outlet VOC concentration to inlet VOC concentration in the gas steam. The steepness of the breakthrough curve determines the extent to which the capability of the adsorbent bed can be used.

The adsorption breakthrough fronts of Yu, *et al.* (2004) measured on a carbon monolith showed that it was effective for cleaning the gas. The carbon-coated ceramic monoliths of Valdés-Solís, *et al.* (2004) exhibited a very sharp breakthrough curve for low concentration VOCs. Figure 20 illustrates a breakthrough curve modelled by Crittenden, *et al.* (2011) for DCM adsorption onto MAST carbon monoliths. The simulations were capable of predicting the experimental breakthrough curve except at higher value of c/c_0.

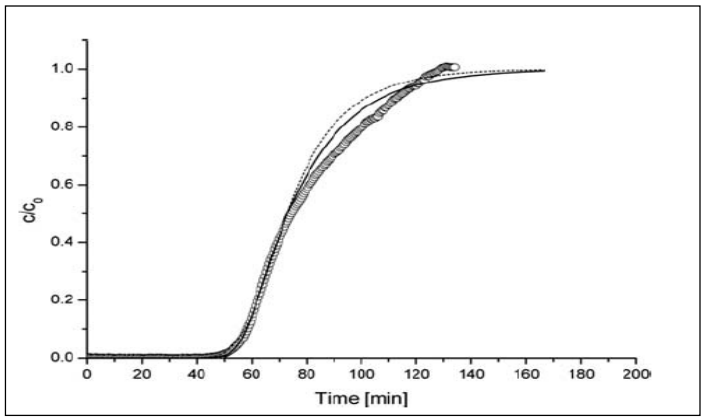

Figure 20. DCM breakthrough curve on activated carbon monolith: experimental vs. modelled data: experimental (○) and modelled (--) and (▬) (Crittenden, *et al.*, 2011)

4.2.2.2. Mass transfer zone

The adsorption process is a transient progression of the polluted gas through the monolithic bed. The amount of VOC adsorbed within the bed depends both on position and time. As the polluted gas enters the bed, it fills up the available sites on the adsorbent. Soon the adsorbent near the entrance gets saturated, and the fluid progresses farther into the bed before all the VOC is removed from the polluted air stream. Thus the active region moves down through the adsorption column as time goes on.

As illustrated in Figure 21, this wave front is better known as the mass transfer zone (MTZ) where mass transfer or active adsorption is actually occurring between the adsorbent and the adsorbate in a fraction of the monolithic bed. While the concentration wave moves through the column, the mass transfer zone moves down the bed, as illustrated in Figure 22. The air exiting the adsorption column has no VOC in it until the

MTZ reaches the exit. VOC starts appearing in the outlet gas stream at the breakthrough time that is when the MTZ reaches the exit. The adsorbing column is not completely saturated until the outlet concentration becomes equal to the initial inlet concentration.

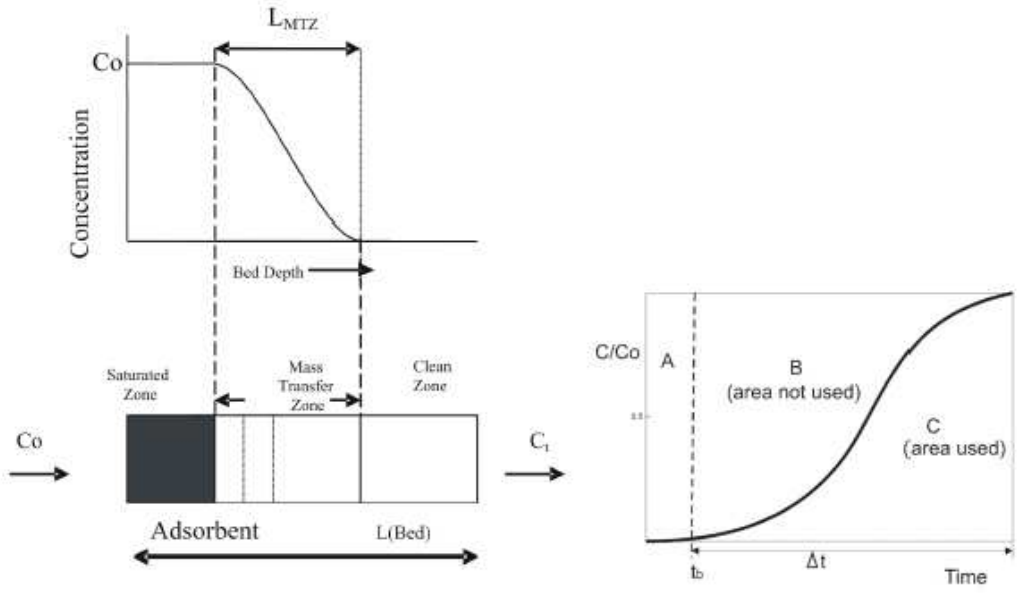

Figure 21. Mass transfer zone concentration profile and breakthrough curve (Sánchez-Liarte, 2009)

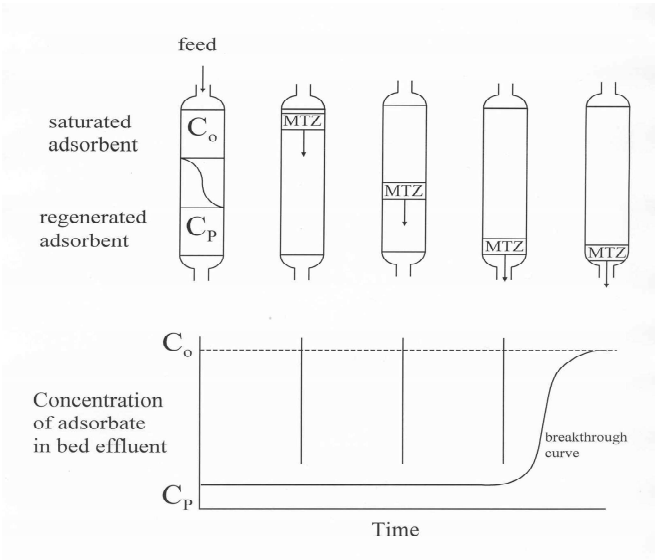

Figure 22. Mass transfer zone concentration profile (Crittenden, 2011)

In the adsorption step, the gas stream is purified by capturing its impurities onto the surface of the adsorbent bed. The concentration of the adsorbed species peaks at the upstream end of the adsorbing bed and reduces over the MTZ. This zone moves progressively downstream if the process is performed indefinitely until it breaks through at the bed's outlet. In industrial practice, regeneration of the adsorbent bed is necessary before this occurs.

The desorption or regeneration step restores the adsorbent bed for reuse. In a TSA process, desorption is attained by increasing the temperature of the system. Therefore, the overall adsorption/desorption process is a cyclic series of adsorption and desorption steps.

4.2.2.3. Transport Phenomena

Kinetics of adsorption can be determined from the breakthrough curve and is governed by the transport phenomena taking place. These phenomena describe the transport of adsorbate from the carrier gas to the interior of the adsorbent. The actual adsorption step at the surface is considered to be very fast. Three resistances are identified to control the overall adsorption kinetic rate:

- Inter-particle external mass transport of the adsorbate from the carrier gas through a thin film neighbouring to the external solid surface.
- Surface diffusion where molecules are transported along the adsorbent surface through the porous structure. Transport then occurs by the movement of the molecules over the surface in the direction of decreasing surface concentration.
- Intra-particle internal mass transport where diffusion inside the pore system is dominated by pore restrictions. Maxwellian and Knudsen diffusion may occur depending on process conditions and molecular dimensions. As the mean free path dimension of the gas molecules is considerably larger than that of the pore diameter, collisions between molecules in the gas are much less numerous than those between molecules and pore walls. Under these conditions the mode of transport is Knudsen diffusion. On the other hand, when the free passage dimension of the gas molecules is much smaller than the pore diameter, gaseous

collisions will be more frequent than collisions of the molecules with pore walls and under these circumstances ordinary bulk diffusion occurs.

Kinetics of adsorption will be discussed further in subsequent Chapters. In the next Chapter, the equations for calculating molecular, Knudsen and effective diffusion will be presented. Consequently internal and external mass transfer estimations will be covered and further discussed.

4.3. Modelling approach

Modelling of the adsorption/desorption process plays an important role in research. It contributes to the understanding of the experimental data and creates a vision of the phenomena taking place. Mathematical modelling of the adsorption and or desorption is addressed in the literature, and a number of numerical models have been developed for the adsorption/desorption of VOCs on activated carbon monolith (Shah, *et al*., 1996; Da silva, *et al*., 1999; Valdés-Solís, *et al*., 2001 & 2004; Patton, *et al*., 2004; Tomasic, *et al*., 2004; Ahn & Brandani, 2005; Grande, *et al*., 2006; Camus, *et al*., 2007; Yu, *et al*., 2007, Crittenden, *et al*., 2011, etc.). Mathematical modelling involves building a number of models, which are tested and validated individually. Individual models include the mass and energy balances of the adsorption and desorption steps. These individual models are then combined together and simulated at steady state conditions. Dynamic and cyclic operations are introduced at a later stage once all the elements of the overall process are in place.

The modelling of the ESA process can be performed in a three-dimensional matrix to account for the geometry of the monolithic channel illustrated in Figure 23 or by employing more simplified descriptions in one and two dimensional spaces. The proposed mathematical models involve dynamic mass and energy balances in the solid and the monolithic channel.

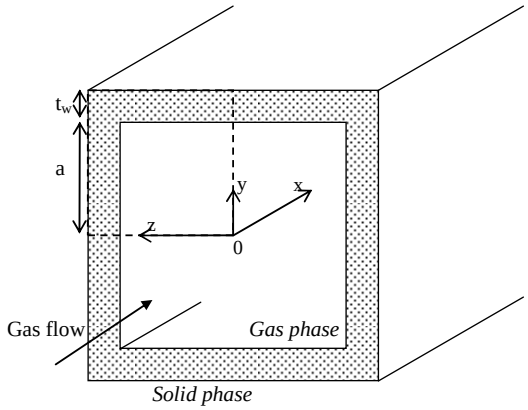

Figure 23. Three dimensional spaces in the solid and the monolithic channel (Camus, *et al.*, 2007)

4.3.1. 1D modelling

A large number of the TSA processes in the literature are modelled in a one-dimensional matrix. In general, the mass balance describes the diffusion in the channels of the monolithic device, the gas velocity in the monolithic channels and the adsorption in the monolith as a function of its porosity.

The model developed by Yu, *el al*. (2007) was for varying operating temperature with mass transfer throughout the adsorbent bed. The developed material balance expressed in mole fraction (y) is:

$$\rho_g \frac{\partial y}{\partial t} - D_{ax}\rho_g \frac{\partial^2 y}{\partial x^2} + u_m \frac{\partial y}{\partial x} + \frac{1-\varepsilon}{\varepsilon}\rho_s \frac{\partial q}{\partial t} = 0 \qquad \text{(eq. 5)}$$

where

D_{ax}	=	axial diffusion coefficient, m^2s^{-1}
q	=	amount of adsorbed toluene, mol kg^{-1}
t	=	time, s
u_m	=	specific molar flux, mol m^{-2} s^{-1}
y	=	toluene mole fraction in gas phase
x	=	axial axis in the column, m

ε = porosity of monolith

ρ_g = gas density, mol m^{-3}

ρ_s = solid density, kg m^{-3}

The experimental setup of Yu, *et al*. (2007) places the monolithic adsorbent in an adsorption cell. Accordingly, the energy balance equations for the gas phase, solid phase and the wall of adsorption cell are given by the following three equations, respectively:

$$\frac{\partial T_g}{\partial t} = \frac{K_{ax}}{c_{pg}\rho_g}\frac{\partial^2 T_g}{\partial x^2} - \frac{u_m}{\rho_g}\frac{\partial T_g}{\partial x} - \frac{h_s a_s}{c_{pg}\rho_g}\frac{1-\varepsilon}{\varepsilon}\left(T_g - T_s\right) \qquad \text{(eq. 6)}$$

$$\frac{\partial T_s}{\partial t} = \frac{h_s a_s}{c_{ps}\rho_s}\left(T_g - T_s\right) + \frac{h_w a_m}{c_{ps}\rho_s}\left(T_w - T_s\right) - \frac{\Delta H_{ads}}{c_{ps}}\frac{\partial q}{\partial t} + \frac{P_v}{c_{ps}\rho_s} \qquad \text{(eq. 7)}$$

$$\frac{\partial T_w}{\partial t} = \frac{h_w a_w}{c_{pw}\rho_w}\left(T_s - T_w\right) - \frac{h_a a_a}{c_{pw}\rho_w}\left(T_w - T_a\right) \qquad \text{(eq. 8)}$$

where

a_s, a_m, a_w = specific surface areas of different elements, m^{-1}

c_{pg} = specific heat capacity of gas, J kg^{-1} K^{-1}

c_{ps} = specific heat capacity of solid, J kg^{-1} K^{-1}

$-\Delta H_{ads}$ = isosteric heat of adsorption, J mol^{-1}

h_s = heat transfer coefficient between solid and gas, W m^{-2} K^{-1}

h_w = heat transfer coefficient from solid to wall, W m^{-2} K^{-1}

K_{ax} = axial thermal conductivity, W m^{-1} K^{-1}

T_g = temperature of the gas, K

T_s = temperature of the monolith, K

T_w = temperature of the vessel wall, K

P_v = electrical power per unit volume of carbon, W m^{-3}

h_a = heat transfer coefficient from wall to air, W m^{-2} K^{-1}

Bonjour, *et al*. (2005) and Clausse, *et al*. (2004) presented a 1D mass and energy model based on indirect heating and cooling using an internal heat-exchanger. Their component mass balance is written in the following form:

$$\frac{\partial c}{\partial t} = -\frac{\partial uc}{\partial x} + D_{ax}\frac{\partial^2 c}{\partial x^2} - \frac{1-\varepsilon}{\varepsilon}\rho_s \frac{\partial q}{\partial t} \qquad \text{(eq. 9)}$$

And the energy balance is given by this equation:

$$(1-\varepsilon)\rho_s c_{ps}\frac{\partial T}{\partial t} = -\varepsilon\sum c_{pg}\frac{\partial(ucT)}{\partial x} + \eta h_s \sum (T_w - T) + (1-\varepsilon)\rho_s \Delta H_{ads}\frac{\partial q}{\partial t} \qquad \text{(eq. 10)}$$

where

η = fins efficiency of the internal heat-exchanger

4.3.2. 2D modelling

A number of studies in the literature (Bonjour, *et al*., 2005; Clausse, *et al*., 2004; Yu, *et al*., 2007) have claimed that under characteristic conditions used in the monolithic column, a one-dimensional (1D) model was adequate to describe the experimental data due to relatively insignificant effect of concentration in the other gradients (radial, y or z directions). However, a 2D model has been used in some studies to represent mainly the solid phase influenced by the diffusion rate.

The model of Shim, *et al*. (2006) described the adsorption breakthrough curve in 1D and 2D based on the transport of VOCs in the gas phase, active layer, and adsorption on adsorbent. The gas phase was modelled as axially dispersed plug flow while the solid phase contained both the axial and radial dimensions (Shim, *et al*., 2006).

Grande and Rodrigues (2008) modelled the electric swing adsorption for CO_2 abatement from flue gases using a MAST activated carbon monolith. Their equation for the mass balance in the gas phase is expressed in 1D by:

$$\frac{\partial c}{\partial t} + a_s\left(\frac{1-\varepsilon}{\varepsilon}\right)k_f\left(c - c_p\right) = -\frac{\partial\left(u_{ave}c\right)}{\partial x} + D_{ax}\left(\frac{\partial^2 c}{\partial x^2}\right) \qquad \text{(eq. 11)}$$

where

k_f = film mass transfer resistance in the boundary layer, s^{-1}

c_p = concentration at gas solid interface, mol m^{-3}

While in the carbon monolith, they considered gas diffusion inside the pore network and the amount adsorbed in the monolith using the following equation:

$$\varepsilon\frac{\partial c_p}{\partial t} + \rho_s\frac{\partial q}{\partial t} = \varepsilon D_{eff}\left(\frac{\partial^2 c_p}{\partial r^2}\right) \qquad \text{(eq. 12)}$$

They employed three energy balances, the first for the gas phase, the second one for the solid phase and the third for the wall. The energy balance equation for the gas phase is:

$$\varepsilon\rho_g c_{pg}\frac{\partial T_g}{\partial t} - \varepsilon R_g T_g\frac{\partial c}{\partial t} = \lambda\left[\frac{\partial^2 T_g}{\partial x^2}\right] - \varepsilon\rho_g c_{pg}u_{ave}\frac{\partial T_g}{\partial x} - (1-\varepsilon)a_s h_f\left(T_g - T_s\right) \qquad \text{(eq. 13)}$$

The energy balance for the monolithic channels is:

$$\rho_s c_{ps}\frac{\partial T_s}{\partial t} = (1-\varepsilon)a_s h_f\left(T_g - T_s\right) + \rho_s\sum\left(-\Delta H_{ads}\right)\frac{\partial q}{\partial t} + \vartheta_{eff}\left(\frac{I}{L_c R_m}\right)^2 \qquad \text{(eq. 14)}$$

Finally, the energy balance for the wall is:

$$\rho_w C_{pw}\frac{\partial T_w}{\partial t} = a_w h_w\left(T_g - T_w\right) - a_a h_a\left(T_w - T_\infty\right) \qquad \text{(eq. 15)}$$

where

h_f = film mass transfer coefficient, s^{-1}

λ = thermal conductivity, W m^{-1} K^{-1}

ϑ_{eff} = effective electrical resistance of the solid

Valdés-Solís, *et al*. (2004) also presented a simulation model with gas diffusion in both the axial and radial directions. The mass balance model was devised for a single, square channel with a flat carbon coating on the wall. The mass balance in the monolithic channel was presented in the axial direction as follows (Valdés-Solís, *et al*., 2001):

$$\frac{\partial c}{\partial t} = -u_{ave}\frac{\partial c}{\partial x} + D_{ax}\frac{\partial^2 c}{\partial x^2} - a_s\frac{1-\varepsilon}{\varepsilon}k_f\left(c - c^*\right) \qquad \text{(eq. 16)}$$

where

c^* = average concentration at the gas solid interface

The mass balance in the channel wall, conversely, was given in the radial direction by the following equation:

$$\left(\frac{\partial q}{\partial c_w} + \varepsilon\right)\frac{\partial c_w}{\partial t} = D_{eff}\left[\frac{\partial^2 c_w}{\partial r^2}\right] \qquad \text{(eq. 17)}$$

where

c_w = concentration in the channel wall

Flow is complex in the experimental setup of Petkovska, *et al*. (2007). Here, the gas flows in the axial direction through the central tube and in the axial direction through the annular space, and in the radial direction through the adsorbent bed, whereas the electric current is passed through the adsorbent bed in the axial direction. As a result, Petkovska, *et al*. (2007) noticed that the concentration and temperature change both in the axial and the radial direction in both the adsorbing bed and the tubes. Hence, using a 1D model, which neglects the deviations in the radial direction and assumes perfect mixing of the gas in the tubes would not be justified (Petkovska, *et al*., 2005). Therefore, Petkovska, *et al*. (2007) built their models in a 2D space taking advantage of the axial symmetry.

4.3.3. 3D modelling

Modelling in 3D is briefly covered in the literature mainly due its computing-intensive nature. However, due to the advancement in computing capabilities and numerical analysis tools, 3D models have been developed lately in the literature for adsorption in rectangular or square channels of monolithic columns (Ahn & Brandani, 2005), in zeolite monoliths (Grande, *et al*., 2006), in slim zeolite films supported on a monolith structure (Perdana, *et al*., 2007), and in binder-less activated carbon monoliths (Crittenden, *et al*., 2011).

Ahn and Brandani (2005) studied the breakthrough dynamics and validated their analytical solution against a full 3D numerical model. The 3D model took into consideration the four corners of the adsorbent monolith wall which was defined as a separate domain and captured the mass transfer resistance accurately.

Later on, Grande, *et al*. (2006) developed a comprehensive 3D mathematical model for propylene adsorption in a square honeycomb monolith encompassing zeolite crystals. The mathematical model was devised in 3D for the bulk phase, the monolith wall and the spherical zeolite crystal to preserve the 3D description of the process.

Perdana, *et al*. (2007) used 2D and 3D models for kinetic modelling of NOx adsorption. The use of a 2D model was adequate for the study of adsorption transport and kinetics. The 3D model, in comparison with the 2D one, gave similar concentration profiles but in a 3D view despite its greater computational demands.

Recently, for non-isothermal operation, fully developed parabolic flow and 3D convection-diffusion equations, Crittenden, *et al*. (2011) applied a model to the adsorption of dichloromethane (DCM) from a polluted air stream passing through a binder-less activated carbon monolith. This model, to a certain extent, is the base case for the current research study aimed towards modelling the complete cyclic process (Crittenden, *et al*., 2011).

4.3.4. Cyclic process

Little has been found in the literature on the modelling of the complete cyclic process of adsorption and desorption. The reason can be attributed to the limitation of the

modelling software used in the simulation. This is addressed in the next section on modelling software. Mostly, adsorption is modelled separately from desorption as indeed are the experimental measurements of the two steps.

Petkovska, *et al*. (2007) modelled the complete ESA cycle of adsorption with electrothermal desorption developed for the recovery of hazardous VOCs onto activated carbon fibre cloth. Desorption was carried out by direct heating of the adsorbent particles based on the Joule effect using an electric current. Modelling was performed using COMSOL Multiphysics and Matlab to integrate the mathematical models of the whole ESA cycle. The models were effectively utilized for the simulation of the different steps of the process and of the whole ESA cycle (Petkovska, *et al*., 2007).

A mathematical model was developed by Grande and Rodrigues (2008) to forecast the behaviour of an ESA process for CO_2 removal from flue gas employing activated carbon honeycomb monolith supplied by MAST carbon (UK). The ESA cycle was projected to detain the CO_2 using an ESA process consisting of feed, electrification, desorption and purge. The proposed model was solved using gPROMS, and it predicted the cyclic behaviour observed experimentally with good accuracy. This model was then utilized in cyclic trials to enhance the overall process performance and achieve superior CO_2 purity and recovery and in assessing the effects of operating conditions (Grande & Rodrigues, 2008).

Based on the findings in the literature, process modelling in 3D of the ESA cycle for the recovery of VOC on activated carbon monoliths is considered in the current research. Even so, 1D modelling will be studied as a building block towards the complete 3D model.

4.4. Modelling software

Mathematical modelling of the ESA process can be performed by using different software. The models are used for the simulation of the ESA process, plus for the examination of the effects of the key operational parameters on the process performance (Petkovska, *et al*., 2007; Crittenden, *et al*., 2011; Zabka, *et al*., 2007).

The selection of the modelling software, such as gPROMS, COMSOL and/or MATLAB, is of critical consequence to the outcomes of the project. The features and limitations of each software are investigated for the sake of selection.

The modelling problem at hand is tackled in a three dimensional matrix. MATLAB is presented as modelling software in the time domain and two dimensions only. Hence this eliminates MATLAB from the current research on three dimensions.

Petkovska, *et al*. (2007) reports the use of COMSOL and MATLAB in combination to simulate the TSA cycle, due to the COMSOL limitation in solving the integral process. Even though different COMSOL models can theoretically be executed successively, shifting from one model to another automatically, by verifying whether certain conditions are met, is not possible in COMSOL (Petkovska, *et al*., 2007).

Grande and Rodrigues (2008) used gPROMS in solving a mathematical model for CO_2 removal from flue gas streams. A model was developed and validated to portray the cyclic ESA process. The ESA cycle consisted of four basic steps: adsorption, electrification, desorption and purge. A number of cyclic simulations were performed by modifying the operating conditions such as the step durations and the flow rates in order to improve the CO_2 purity and recovery.

COMSOL Multiphysics software is based on the finite element method (FEM). The finite element method (FEM) is a numerical approach for locating estimated answers to partial differential equations (PDEs). The estimated solution is approximated based on eliminating the differential equations or on transforming these PDEs into ordinary differential equations (ODEs). FEM is a reasonable option for solving PDEs over complicated domains.

gPROMS, on the other hand, uses the finite difference method (FDM) for resembling the solution to the differential equations. The finite difference method uses finite difference equations to approximate the derivatives by replacing derivative expressions with roughly equal difference quotients. Finite difference methods relate a grid to the tested region and solve the PDEs by estimating the derivatives using the Taylor series expansion and by using differences as approximation. For this approach the utilization of a uniform grid over the tested region is crucial in order to decrease the errors resulting from the differencing approach. Therefore, the finite difference method

is considered inadequate for irregular shapes in comparison to the finite element method which divides the tested region into separate elements covering the whole region and solves the PDE. The FD method has a number of benefits among which are the facts that they are easy to understand, to describe, and to program. The mesh resulting from applying a uniform grid is simple, and the error is estimated from the remainder of the Taylor series expansion of the derivatives.

The differences between FEM and FDM comes from the way in which the variables are approximated and the discretization processes. FDM involves approximating derivatives in a PDE and then solving the algebraic equations. In FEM, the integral equation derived from the differential equation is solved by assuming a piecewise continuous function over the domain.

As a result, gPROMS is proposed as the desired modelling software for the study at hand for its capability of handling cyclic processes. gPROMS is a general process modelling software licensed by Process Systems Enterprise Ltd. It is an object-oriented modelling and simulation tool that enables equation-based modelling, and includes a wide range of algebraic equations, ordinary differential equations (ODE) and partial differential equations (PDE) solvers and optimization routines.

Mathematical modelling of the ESA process involves building a number of models, which are then combined together as a gPROMS process and simulated at steady state conditions. After having all the elements of the overall process in place, dynamics and cyclic operations are introduced. The cyclic operation can be introduced in gPROMS using tasks, which are utilized to introduce and simulate different scenarios. The flexibility provided in gPROMS is that model development is established incrementally from the simpler models toward the overall goal of modelling the complete cyclic steady state incorporating the steps of adsorption and desorption.

4.5. References

Ahn, H. & Brandani, S., 2005. Analysis of breakthrough dynamics in rectangular channels of arbitrary aspect ratio. *AIChE Journal*, 51(7), pp.1980-1990.

Bansal, R. C. & Goyal, M., 2005. *Activated Carbon Adsorption*. CRC Press.

Bonjour, J., Clausse, M. & Meunier, F., 2005. A TSA process with indirect heating and cooling: parametric analysis and scaling-up to practical sizes. *Chemical Engineering and Processing*, 44, pp.969-977.

Burchell T. D., Judkins, R.R., Rogers, M.R. & Williams, A.M., 1997. A novel process and material for the separation of carbon dioxide and hydrogen sulphide gas mixtures. *Carbon,* 35, pp.1279-1294.

Camus, O., Crittenden, B., Perera, S., Mays, T., Sánchez-Liarte, F., Patsos, A., Tennison, S. R. & Crezee, E., 2007. Non-uniformities in adsorbent monoliths, *In: 9th International conference on Fundamentals of Adsorption,* 20 - 25 May. Giardini Naxos, Sicily.

Clausse, M., Bonjour, J. & Meunier, F., 2004. Adsorption of gas mixture in TSA adsorbers under various heat removal conditions. *Chemical Engineering Science,* 59, pp.3657-3670.

Crezee, E., Tennison, S. R., Rawling, A. P., Place, R.N., Crittenden, B. D. & Perera, S. P., 2005. Electrically regenerable carbon monolithic adsorption system for the recovery and recycle of volatile organic chemicals (VOCs). *In: World Congress of Chemical Engineering, 7th*, July 10 - 14, 2005, Glasgow, United Kingdom.

Crittenden, B. D., 2011. *Discussion on ACM* [email] (Personal communication, 5 December 2011).

Crittenden, B. D., Camus, O., Perera, S. P., Mays, T. J., Sánchez-Liarte, F., Tennison, S. R. & Crezee, E., 2011. Nonuniform channels in adsorbent monoliths. *AIChE Journal*, 57(5), pp.1163-1172.

Da Silva, D.F.A., Silva, J. A. & Rodrigues, A. E., 1999. A General Package for the Simulation of Cyclic Adsorption Processes. *Adsorption*, 5 (3), pp.229-244.

Fabuss B.M. & Dubois, W.H., 1970. Carbon adsorption-electrodesorption process. *In: Proceedings of the 63rd Annual Meeting of the Air Pollution Control Association*, 70 - 68, St. Louis, Missouri, June 14-18, 1970, p.18.

Freundlich, H, 1924. *The element of Colloidal Chemistry*, translated by George Barger, Dutton and Company Publishers, New York, pp.58-61.

Grande, C. A, & Rodrigues, A. E., 2008. Electric swing adsorption for CO2 removal from flue gases. *International Journal of Greenhouse Gas Control*, 2(2), pp.194-202.

Grande, C. A., Cavenati, S., Barcia, P., Hammer, J., Fritz, H.G. & Rodrigues, A.E., 2006. Adsorption of propane and propylene in zeolite for a honeycomb monolith, *Chemical Engineering Science*, 61, pp.3053-3067.

Langmuir, I., 1916. The constitution and fundamental properties of solids and liquids. Part I. Solids. *Journal of American Chemical Society*, 38, pp.2221-95.

Menard, D., Py, X. & Mazet, N., 2007. Activated carbon monolith of high thermal conductivity for adsorption processes improvement Part B. Thermal regeneration. *Chemical Engineering and Processing*, 46(6), pp.565-572.

Patton, A., Crittenden, B. D. & Perera, S. P., 2004. Use of the linear driving force approximation to guide the design of monolithic adsorbents. *Chemical Engineering Research Des*., 82, pp. 999-1009.

Perdana, I., Creaser, D., Made Bendiyasa, I. & Rochmadi, Tyoso, B. W., 2007. Modelling NOx adsorption in a thin NAZSM-5 film supported on a cordierite monolith. *Chemical Engineering Science*, 62(15), pp.3882-3893.

Petkovska, M, Antov, D. & Sullivan, P., 2005. Electrothermal desorption in an annual-radial flow-ACFC adsorber-mathematical modeling. *Adsorption,* 11(1Suppl.), pp.585-590.

Petkovska, M., Antov-Bozalo, D., Markovic, A. & Sullivan, P., 2007. Multiphysics modeling of electric-swing adsorption system with in-vessel condensation. *Adsorption*, 13(3-4), pp.357 -372.

Place R. N., Blackburn, A. J. Tennison S. R., Rawlinson A. P. & Crittenden B. D., 2005. Method and equipment for removing volatile compounds from air. US Patent 6964695, European Patent 1372917.

Sánchez-Liarte, F., 2009. *Performance of electrically regenerable monolithic adsorbents for VOC control*. Ph.D. thesis: University of Bath.

Saysset, S., Grevillot, G. & Lamine, A.S., 1999. Adsorption of Volatile Organic Compounds on Carbonaceous Adsorbent and Desorption by Direct Joule Effect.

Recent Progress in Génie des Procèdes, No. 68. *Proceedings of the 2nd European Congress of Chemical Engineering*, Montpellier, France, pp.389-396.

Shah, D. B., Perera S. P., & Crittenden, B. D., 1996. Adsorption dynamics in a monolithic adsorbent. In: M.D. LeVan, Editor, *Fundamentals of Adsorption*, Kluwer Academic Publishers, Boston, USA, 1996.

Shepherd, A., 2001, Activated Carbon Adsorption for treatment of VOC Emissions, 13th Annual EnviroExpo, Boston Massachussets.

Shim**,** W. G., Moon, H and Lee**,** J. W., 2006. Performance evaluation of wash-coated MCM-48 monolith for adsorption of volatile organic compounds and water vapors. *Microporous and Mesoporous Materials*, Volume 94, Issues 1-3, pp.15-28.

Sullivan, P. D., Rood, M. J., Grevillot, G., Wander J. D. & Hay, K. J., 2004. Activated carbon fiber cloth electrothermal swing adsorption system. *Environment Science Technology*, 38, pp.4865-4877.

Sullivan, P.D., 2003. *Organic vapor recovery using activated carbon fiber cloth and electrothermal desorption*. Ph.D. Thesis. University of Illinois at Urbana-Champaign.

Tomasic V., Zrncevic S. & Gomzi Z., 2004. Direct decomposition of NO in a monolith reactor: comparison of mathematical models. *Catalysis Today*, 90(1-2), pp.77-83.

Tóth, J., 1962. Gas-(Dampf-) adsorption an festen Oberflachen in homogener Aktivitat, I. *Acta Chimica Academiae Scientiarum Hunngaricar*, 30, pp. 415.

Valdés-Solís, T., Linders, M., J. G., Kapteijn, F., Marban, G. & Fuertes, A. B., 2004. Adsorption and breakthrough performance of carbon-coated ceramic monoliths at low concentration of *n*-butane. *Chemical Engineering Science***,** 59(13), pp.2791-2800.

Valdés-Solis, T., Marban, G. & Fuertes, A. B., 2001. Preparation of microporous carbon-ceramic cellular monoliths. *Microporous and Mesoporous Materials*, 43, pp.113-126.

Wright, A. D., Kalbassi, M. A. & Golden, T. C., 2005. Prepurification of Air Using an Advanced Thermal-Pressure Swing Adsorption (TPSA) Cycle. *The 2005 Annual Meeting.* Cincinnati, OH.

Yu, F. D., 2003. *Adsorption de composés organiques volatils sur un monolithe de charbon actif avec régénération thermique par effect Joule*. Ph.D. Thesis, Ecole Nationale Superieur des industrie chimiques, Laboratoire des Sciences du Génie Chimique, L'institut National Polytechnique de Lorraine, France.

Yu, F. D., Luo, L. A. & Grevillot, G., 2002. Adsorption Isotherms of VOCs onto an Activated Carbon Monolith: Experimental Measurement and Correlation with Different Models. *Journal of Chemical Engineering Data*, 47 (3), pp.467-473.

Yu, F. D., Luo, L. A. & Grevillot, G., 2007. Electrothermal swing adsorption of toluene on an activated carbon monolith: Experiments and parametric theoretical study. *Chemical Engineering and Processing: Process intensification*, 46 (1), pp.70-81.

Zabka, M., Minceva, M. & Rodrigues, A. E., 2007. Experimental characterization and modelling of analytical monolithic column. *Journal of Biochemical and Biophysical Methods*, 70, pp. 95-105.

Chapter 5

One dimensional modelling

In advance of studying three dimensional modelling which is described in Chapters 7 and 8, mass and energy balances are developed firstly in a one dimensional matrix in this Chapter and the results of 1D modelling are described in Chapter 6. The parameters used in the developed models are also presented and discussed in this Chapter. The values of these parameters are based on experimental data from the University of Bath and estimated data from the literature. The assumptions made in terms of geometry and equations pertain to the University of Bath's particular conditions. The performance of the monoliths of different scale (bench scale and pilot scale) has been tested.

5.1. Geometrical presentation

The monoliths NovaCarb^{TM} used at the University of Bath in the bench and pilot scale apparatuses have been provided and manufactured by MAST Carbon Technology Ltd. Details on the manufacturing procedure of the MAST activated carbon monolith have been presented in Chapter 3. The monolithic activated carbons used are cylindrical in shape and extruded in square channels, as illustrated in Figure 24. This monolith is about 19 mm in diameter with a nominal channel dimension of 0.7 mm. This bench scale monolith is 103 mm long. Visually, as can be observed in the Figure, the channels in the centre of the monolith have a bigger cross sectional area than those at the edge, which are somewhat irregular in shape.

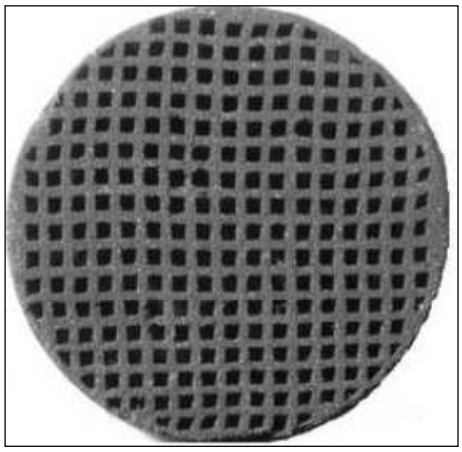

Figure 24. Cross sectional area of bench scale activated carbon monolith (Camus, *et al*., 2007)

Otherwise, the channels are square in shape, with two main characteristic dimensions: the channel wall thickness (*e*) and the channel width (*d*), shown in Figure 25.

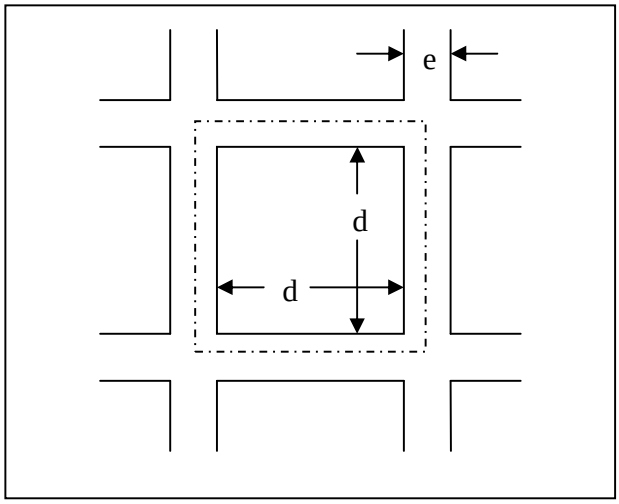

Figure 25. Scheme of the cell considered in the simulation

The physical properties of the bench-scale monolith used in the study at hand are summarized in Table 1.

Table 2. Physical properties of ACM bench scale model (Crittenden, *et al*., 2011)

Monolith overall length, *L*	103 mm
Monolith overall diameter, *D*	18.6 mm
Monolith total mass	13.2 g
Nominal channel size, *d*	0.7 mm
Nominal wall thickness, *e*	0.35 mm
Fractional free cross section, ε	0.44
Cell density	90 cell cm^{-2}

The monolith comprises a bundle of parallel channels forming the honeycomb structure. The assumption of complete uniformity in the channels (Groppi, *et al*., 2000) is assumed for the current modelling where the internal diameter and wall thickness are uniform throughout the length of the monolith and are the same for all the channels.

Most models in the literature are restricted to a single channel monolith and necessitate the evaluation of some of the model parameters to fit the experimental data. Crittenden, *et al*. (2011), on the other hand, accounted for the overall performance of an activated carbon monolith which has channels of varying dimensions by comparing two approaches: the uniform channel model (UCM) and the non-uniform channel model (NUCM).

5.2. ESA model development

5.2.1. Assumptions

A number of assumptions were made in the development of the model, and these assumptions are listed as follows:

- Gas phase is assumed ideal and so the ideal gas law is utilized.
- Gas is distributed uniformly in all the channels at the monolith entrance.
- Flow is plug flow.
- Only a single channel is modelled.

- Pressure drop is negligible.
- Purge gas (N_2) is not adsorbed.
- Internal mass transfer is represented by the linear driving force (LDF) approximation (Yang, 1987).
- Gradients of concentration and velocity within the channels at right angles to the direction of flow are negligible.
- Solid phase is considered to be homogenous.

5.2.2. Mass and energy equations for adsorption & desorption

The literature, as presented in the previous Chapter, supplies a large spectrum of models that describe the TSA process, but each model is specific to the experimental setup used by the different authors, the assumptions made for simplification, and the objective of the studies conducted. These previously published models have been very helpful in the model development of the mass and energy balances in the present study.

5.2.2.1. Mass balance equations

In general, the mass balance should describe the molecular diffusion in the monolith (Valdés-Solís, *et al*., 2004**)**, the gas velocity in the channels of the monolith, the porosity and void fraction in the monolith, the uniform or non-uniform channel model (Crittenden, *et al*., 2011), the density of the solid, and the different types of adsorption isotherm. Different equations, such as Tóth, Langmuir, Freundlich, presented in the previous Chapter, describe the vapour-solid adsorption isotherms of VOCs onto activated carbon monolith. Various zones of the adsorption process are identified and compared, such as external and internal mass transfer, the mass balance in the bulk phase or in the channel wall.

The mass balance model developed in this study is for only one VOC component (dichloromethane, DCM) being adsorbed in a single square channel. The single phase flow regime in monolithic channels is laminar flow, and axially dispersed plug flow through the channel is assumed with mass transfer to the wall.

Based on the assumptions made, the mass balance is constructed by taking a differential section of the monolith perpendicular to the flow of the gas between x and $x+dx$ for an adsorbent at time t and for a duration of dt, as presented in the following equations.

Entrance:

$$\varepsilon A\left[u_{ave}c(x) - D_{ax}\frac{\partial c(x)}{\partial x}\right]dt \qquad \text{(eq. 18)}$$

Exit:

$$\varepsilon A\left[u_{ave}c(x+dx) - D_{ax}\frac{\partial c(x+dx)}{\partial x}\right]dt \qquad \text{(eq. 19)}$$

Accumulation in the gas phase:

$$\varepsilon A dx\frac{\partial c(x)}{\partial t}dt \qquad \text{(eq. 20)}$$

Accumulation in the solid phase:

$$(1-\varepsilon)\rho_s A dx\frac{\partial q(x)}{\partial t}dt \qquad \text{(eq. 21)}$$

The simplest one-dimensional model material balance for a single VOC in the gas phase then amounts to:

$$\frac{\partial c}{\partial t} - D_{ax}\frac{\partial^2 c}{\partial x^2} + u_{ave}\frac{\partial c}{\partial x} + \frac{1-\varepsilon}{\varepsilon}\rho_s\frac{\partial q}{\partial t} = 0 \qquad \text{(eq. 22)}$$

where

c	=	gas phase concentration, mol m^{-3}
t	=	time, s
D_{ax}	=	axial diffusion coefficient, $m^2 s^{-1}$
x	=	axial position of column, m
u_{ave}	=	interstitial velocity, m s^{-1}
ε	=	porosity of monolith
q	=	amount of VOC adsorbed, mol kg^{-1}
ρ_s	=	solid density, kg m^{-3}
A	=	gas channel surface area, m^2

The mass transfer kinetics between the gas and the solid phase are expressed by the linear driving force (LDF) approximation (Yang, 1987):

$$\frac{\partial q}{\partial t} = k\left(q^* - q\right) \qquad \text{(eq. 23)}$$

where q^* is the quantity adsorbed in equilibrium with the gas of concentration c and calculated by the Tóth equation which provided the best fit for DCM data based on the previous Chapter:

$$q^* = q_m \frac{bPc/\rho_g}{\left(1+\left(bPc/\rho_g\right)^t\right)^{1/t}} \qquad \text{(eq. 24)}$$

where

b	=	affinity coefficient, Pa^{-1}
k	=	mass transfer coefficient, s^{-1}
P	=	total pressure, Pa
ρ_g	=	gas density, mol m^{-3}
q	=	amount of VOC adsorbed, mol kg^{-1}
q^*	=	loading in equilibrium with gas, mol kg^{-1}
q_m	=	maximum solid loading, mol kg^{-1}
t	=	parameter of Tóth model

As will be seen later, the mass transfer coefficient k is related to the geometry of the adsorbent and an effective diffusion coefficient D_{eff}. This coefficient has to account for the various types of diffusion which take place within the adsorbent. These aspects will be discussed later. This mass balance of equation (eq. 22) accounts for the molecular diffusion in the axial direction, the interstitial velocity, the porosity of monolith and VOC adsorbed onto the solid monolith.

5.2.2.2. Energy balance equations

The energy balance is not fully explored in the literature, as few authors have included the energy balance in their studies (Clausse, *et al.*, 2004; Bonjour, *et al.*, 2005; Menard, *et al.*, 2007; Petkovska, *et al.*, 2007; Yu, *et al.*, 2007). Some of the important

parameters to be accounted for in the heat balances of the gas and solid phases are the configuration of the monolithic adsorber, the thermal conductivity of the monolith, the surface area, the porosity of the monolith, density of gas and solid, temperatures of the gas and solid, the heat capacity of the adsorbent, the heat transfer between the gas and the solid, etc. In addition, the sensitivity of the performances to the regeneration temperature and purge flow rates is to be considered.

The energy balance consists of heat transfer between the gas phase and the solid, heat of adsorption and finally heat generated by the Joule effect. The energy balance can then be written in a similar fashion to that of the mass balance, as follows:

Entrance:

$$\varepsilon A\left[u_m c_{pg} T_g(x) - \frac{K_{ax}}{MW}\frac{\partial T_g(x)}{\partial x}\right]dt \qquad \text{(eq. 25)}$$

Exit:

$$\varepsilon A\left[u_m c_{pg} T_g(x+dx) - \frac{K_{ax}}{MW}\frac{\partial T_g(x+dx)}{\partial x}\right]dt \qquad \text{(eq. 26)}$$

Accumulation in the gas phase:

$$\varepsilon A dx c_{pg}\rho_g \frac{\partial T_g(x)}{\partial t}dt \qquad \text{(eq. 27)}$$

Exchange between the gas phase and the solid:

$$\frac{h_s a_s (1-\varepsilon) A dx (T_g - T_s) dt}{MW} \qquad \text{(eq. 28)}$$

The resulting heat balances for VOC amount to:

$$\frac{\partial T_g}{\partial t} = \frac{K_{ax}}{c_{pg}\rho_g MW}\frac{\partial^2 T_g}{\partial x^2} - \frac{u_m}{\rho_g}\frac{\partial T_g}{\partial x} - \frac{h_s a_s}{c_{pg}\rho_g MW}\frac{1-\varepsilon}{\varepsilon}(T_g - T_s) \qquad \text{(eq. 29)}$$

$$\frac{\partial T_s}{\partial t} = \frac{h_s a_s}{c_{ps}\rho_s}(T_g - T_s) - \frac{\Delta H_{ads}}{c_{ps}}\frac{\partial q}{\partial t} + \frac{P_v}{c_{ps}\rho_s} \qquad \text{(eq. 30)}$$

where

a_s = specific surface area, m^{-1}

c_{pg} = specific heat capacity of gas, J kg^{-1} K^{-1}

c_{ps} = specific heat capacity of solid, J kg^{-1} K^{-1}

$-\Delta H_{ads}$ = isosteric heat of adsorption, J mol^{-1}

h_s = heat transfer coefficient between solid and gas, W m^{-2} K^{-1}

K_{ax} = axial thermal conductivity, W m^{-1} K^{-1}

T_g = temperature of the gas, K

T_s = temperature of the solid, K

u_m = specific molar flux, mol m^{-2} s^{-1}

MW = molecular weight of the gas, kg mol^{-1}

x = axial position of column, m

P_v = volumetric power, W m^{-3}

The difference between conventional TSA and ESA processes is the volumetric power term P_v in the energy equation. The volumetric power (P_v) is defined as the power per unit volume of the carbon monolith, at constant intensity, and is given by:

$$P_v = \rho(T,q)\left(1+\frac{\varepsilon}{1-\sqrt{\varepsilon}}\right)(1-\varepsilon)^{-1}\frac{4I^2}{\pi D^2 L} \qquad \text{(eq. 31)}$$

where

P_v = volumetric power, W m^{-3}

ρ = electrical resistivity of the monolith as a function of temperature and amount of VOC adsorbed, Ω

I = electrical intensity, A

L = length of the monolith, m

D = diameter of the monolith, m

The volumetric power cannot be provided experimentally from the University of Bath. Therefore, the energy balances are simplified further by omitting the volumetric

power term. The energy balances for the gas and solid phases amount then to the following format:

$$\frac{\partial T_g}{\partial t} = \frac{K_{ax}}{c_{pg}\rho_g MW}\frac{\partial^2 T_g}{\partial x^2} - \frac{u_m}{\rho_g}\frac{\partial T_g}{\partial x} - \frac{h_s a_s}{c_{pg}\rho_g MW}\frac{1-\varepsilon}{\varepsilon}\left(T_g - T_s\right) \qquad \text{(eq. 32)}$$

$$\frac{\partial T_s}{\partial t} = \frac{h_s a_s}{c_{ps}\rho_s}\left(T_g - T_s\right) - \frac{\Delta H_{ads}}{c_{ps}}\frac{\partial q}{\partial t} \qquad \text{(eq. 33)}$$

where

a_s = specific surface area, m^{-1}

c_{pg} = specific heat capacity of gas, J kg^{-1} K^{-1}

c_{ps} = specific heat capacity of solid, J kg^{-1} K^{-1}

$-\Delta H_{ads}$ = isosteric heat of adsorption, J mol^{-1}

h_s = heat transfer coefficient between solid and gas, W m^{-1} K^{-1}

K_{ax} = axial thermal conductivity, W m^{-1} K^{-1}

T_g = temperature of the gas, K

T_s = temperature of the solid, K

u_m = specific molar flux, mol m^{-2} s^{-1}

MW = molecular weight of the gas, kg mol^{-1}

x = axial position of column, m

Equation (eq. 33) should be extended to account for heating and cooling by the addition of the heating or cooling rates to the equation. The heating rate should produce the same effect of the volumetric power term.

5.2.3. Initial and boundary conditions

The initial and boundary conditions are set as follows:

For adsorption, the monolith at the entrance is VOC free, and the temperatures of the gas and solid are at ambient temperature:

At $t = 0$, $c = c_0$ and $q = 0$. $T_g = T_s = T_a$

$$\text{At } t > 0,\ D_{ax}\left.\frac{\partial c}{\partial x}\right|_{x=0} = u_{ave}\left(c - c_0\right) \text{ and } \left.\frac{\partial c}{\partial x}\right|_{x=L} = 0 \qquad \text{(eq. 34)}$$

$$\text{At } t > 0,\ K_{ax}\left.\frac{\partial T_g}{\partial x}\right|_{x=0} = u_m c_{pg} MW\left(T_g - T_s\right) \text{ and } \left.\frac{\partial T_g}{\partial x}\right|_{x=L} = 0 \qquad \text{(eq. 35)}$$

For desorption, the monolith at the entrance requires regeneration. The inlet gas is VOC free, and the temperatures of the gas and solid are at regeneration temperature of 200ºC:

At $t = 0$, $c = 0$ and $q = q_0$. $T_g = T_s = T_a$

$$\text{At } t > 0,\ D_{ax}\left.\frac{\partial c}{\partial x}\right|_{x=0} = u_{ave}\left(c - c_0\right) \text{ and } \left.\frac{\partial c}{\partial x}\right|_{x=L} = 0 \qquad \text{(eq. 36)}$$

$$\text{At } t > 0,\ K_{ax}\left.\frac{\partial T_g}{\partial x}\right|_{x=0} = u_m c_{pg} MW\left(T_g - T_s\right) \text{ and } \left.\frac{\partial T_g}{\partial x}\right|_{x=L} = 0 \qquad \text{(eq. 37)}$$

5.2.4. Mass and energy balance parameters for adsorption and desorption

Parameters used in the mass and energy balances are described as follows and are calculated according to the supplied equations. Some of these parameters are temperature dependent and thereby differ for adsorption and desorption. Adsorption is conducted at ambient temperature whereas desorption takes place at around 200ºC.

The adjustment of temperature dependent parameters for adsorption and desorption adds to the accuracy of the developed model. In another study, the authors chose to simplify their model by considering most of their physical and transport parameters as constants, although these parameters change with temperature. Supposedly, these parameters add to the complexity of the model with the introduction of overlapping equations (Pekovska, *et al*., 2007).

In addition, the accuracy of calculating these parameters has an impact on the predicted breakthrough curve. Some of these parameters have a minor effect on the breakthrough curve whereas others can dramatically change the shape of this curve.

The values of the mass and energy balances parameters are summarized in Table 3. These parameters are described and calculated as follows and are used in modelling the adsorption and desorption processes on the bench-scale apparatus.

Table 3. Values of University of Bath parameters used in mass balance for adsorption and desorption at the bench scale

Description	Parameter	Value	Unit
Initial concentration	c_0	2000	ppmv
Axial diffusion coefficient (adsorption)	D_{ax}	2.536×10^{-4}	$m^2\ s^{-1}$
Axial diffusion coefficient (desorption)	D_{ax}	2.074×10^{-4}	$m^2\ s^{-1}$
Density of gas (adsorption)	ρ_g	43.15	$mol\ m^{-3}$
Density of gas (desorption)	ρ_g	25.7	$mol\ m^{-3}$
Interstitial velocity	u_{ave}	1	$m\ s^{-1}$
Specific molar flux (adsorption)	u_m	40.9	$mol\ m^{-2}\ s^{-1}$
Specific molar flux (desorption)	u_m	23.19	$mol\ m^{-2}\ s^{-1}$
Flow rate	Q	7.2	$l\ min^{-1}$
Porosity of monolith	ε	0.44	
Density of solid	ρ_s	842.2	$kg\ m^{-3}$
Maximum amount adsorbed	q_m	4680	$mol\ m^{-3}$
Affinity parameter (adsorption)	b	0.13	Pa^{-1}
Affinity parameter (desorption)	b	8.3E-5	Pa^{-1}
Tóth parameter	t	0.463	
Mass transfer coefficient	k	3.26×10^{-3}	s^{-1}
Length of monolith	L	0.103	m
Diameter of monolith	D	0.0186	m
Channel dimension	d	0.0007	m
Channel wall thickness	e	0.00035	m
Temperature (adsorption)	T	25	ºC
Pressure	P	101325	Pa
Affinity parameter	b_o	2.615×10^{-6}	$m^3\ mol^{-1}$
Isosteric heat of adsorption	ΔH_{ads}	46,169	$J\ mol^{-1}$
Molecular diffusion coefficient	D_{mol}	1.04976×10^{-5}	$m^2\ s^{-1}$
Effective diffusion coefficient	D_{eff}	4.5×10^{-11}	$m^2\ s^{-1}$
Axial thermal conductivity (adsorption)	K_{ax}	23	$W\ m^{-1}\ K^{-1}$
Axial thermal conductivity (desorption)	K_{ax}	18	$W\ m^{-1}\ K^{-1}$
Heat transfer coefficient (adsorption)	h_s	6.16	$W\ m^{-2}\ K^{-1}$
Heat transfer coefficient (desorption)	h_s	4.36	$W\ m^{-2}\ K^{-1}$
Heat capacity of nitrogen	c_{pn}	1040	$J\ kg^{-1}\ K^{-1}$
Heat capacity of air	c_{pa}	1000	$J\ kg^{-1}\ K^{-1}$
Heat capacity of solid	c_{ps}	1000	$J\ kg^{-1}\ K^{-1}$
Specific surface area	a_s	4571.4	m^{-1}

5.2.4.1. Concentration (*c*)

For the experimental runs carried out by others at the University of Bath, the concentration of VOC in the air stream at the outlet of the monolith was measured using a flame ionization detector (FID) for total hydrocarbons. This analyzer ionizes the molecules contained in the sample gas using a combustion process created with a hydrogen flame. The amounts of hydrocarbons are then measured in an electrode and a signal is produced. The initial concentration (c_0) of the polluted gas entering the monolithic adsorption column amounts to 2000 ppmv. This concentration is converted to mole fraction by multiplying one part per million volume (ppmv) by 10^{-6}. The concentration can also be obtained in mol m^{-3} by multiplying the concentration in mole fraction by the density of the gas.

5.2.4.2. Interstitial velocity (u_{ave})

The interstitial velocity is defined as the amount of gas that flows through the cross sectional area of the monolith per unit time. The interstitial velocity or the average channel velocity (u_{ave}) and the molar flux (u_m) are given consecutively in the following two equations:

$$u_{ave} = \frac{QF}{\varepsilon A} = \frac{QF}{\varepsilon * \left(\frac{\pi D^2}{4} \right)} \qquad \text{(eq. 38)}$$

$$u_m = \frac{PQ}{RTA\varepsilon} = \frac{Pu_{ave}}{RT} \qquad \text{(eq. 39)}$$

where

u_{ave}	=	interstitial velocity, m s^{-1}
u_m	=	molar flux, mol m^{-2} s^{-1}
Q	=	flow rate, litre min^{-1}
D	=	monolith diameter, m
A	=	monolith area, m^2
F	=	factor to convert l min^{-1} to m^3 s^{-1}

5.2.4.3. Density of the gas (ρ_g)

For adsorption, the density of the polluted gas is assumed to be that of air at 25°C with a value of 43.15 mol m^{-3}. This assumption is realistic since the treated gas predominantly consists of air. For desorption, the density of gas is that of nitrogen at 200°C, that is 25.7 mol m^{-3}. Nitrogen is the purge gas used in desorption.

5.2.4.4. Porosity (ε)

The porosity or voidage of a monolith is defined to be its fractional free space that is the volume of all the channels divided by the overall volume. Clearly, the porosity is also the fractional free cross-sectional area available for gas flow. The geometry of the monolithic structures can be categorized by three primary parameters, which are the shape of the channels or cells, the channel size and the wall thickness. Other characteristic parameters, like cell density and the void fraction or porosity can be calculated from these primary parameters (Crittenden, *et al.*, 2005). Crittenden, *et al*. (2005) calculated the monolith porosity (ε) for a square channel as follows. The porosity of the square-channel monolith studied having a channel size of 0.7 mm and wall thickness of 0.35 mm amounts to 0.44:

$$\varepsilon = \frac{d^2}{(d+e)^2} \qquad \text{(eq. 40)}$$

where

e	=	wall thickness, m
d	=	channel size, m
ε	=	fractional free cross-section or porosity

5.2.4.5. Cell density (n_D)

Crittenden, *et al*. (2005) also calculated the cell density for a square channel monolith as follows. The density of the solid amounts to 90 cell cm^{-2} for the monolith of this study having a channel size of 0.7 mm:

$$n_D = \frac{\varepsilon}{d^2} \qquad \text{(eq. 41)}$$

where

d = channel size, m

ε = fractional free cross-section or porosity

5.2.4.6. Maximum amount adsorbed (q_m)

The maximum adsorption capacity of the activated carbon for DCM is determined from the adsorption isotherm using the IGA (Intelligent Gravimetric Analyzer) in the laboratory of the University of Bath. The analyzer takes readings of mass uptake at regular intervals of pressure. The analyzer uses a gravimetric technique to measure the change in weight of a sample. The mass uptake of the sample is measured as a function of time at an equilibrium pressure and temperature. When the equilibrium is established at a determined pressure point, the pressure increases up to the next set pressure point to reach equilibrium and the uptake is measured.

5.2.4.7. Affinity coefficient (b)

The affinity coefficient is a measure of how strongly the adsorbate is attracted onto the monolithic surface, and it is dependent on the temperature of activated carbon as presented in the van't Hoff equation:

$$b = b_0 \exp\left(\frac{-\Delta H_{ads}}{RT}\right) \qquad \text{(eq. 42)}$$

where

b_0 = affinity parameter, Pa^{-1}

$-\Delta H_{ads}$ = enthalpy of adsorption, J mol^{-1}

R = ideal gas law constant, m^3 Pa K^{-1} mol^{-1}

T = temperature, K

The affinity coefficient decreases as the temperature of adsorption increases, and the larger the affinity coefficient the more molecules are attached to the surface of the activated carbon. This can be explained thermodynamically from the Gibbs equation:

$$\Delta G = \Delta H - T\,\Delta S < 0 \qquad \text{(eq. 43)}$$

The physisorption is a spontaneous process where the free energy decreases. The molecules lose their free degrees as they are adsorbed, and entropy is lowered. The enthalpy change then becomes negative resulting in an exothermic process ($\Delta H < 0$).

5.2.4.8. Isosteric heat of adsorption (ΔH_{ads})

The isosteric heat of adsorption gives a measurement of the infinitesimal change in the adsorbate enthalpy with respect to an infinistesimal change in the amount adsorbed. During the adsorption process, heat is released and part of this heat is absorbed by the adsorbent, increasing its temperature and increasing the kinetics of adsorption at which adsorption takes place.

Adsorption isosteres are obtained from the adsorption isotherm using the van't Hoff equation when the amount adsorbed is fixed. The value of the energy of adsorption is obtained when the multiple fit to the Tóth model is carried out on the isotherm data. The isosteric heat of adsorption corresponds with the value of the energy of adsorption when the amount adsorbed is zero (Do, 1998).

The van't Hoff equation relates the change in temperature to the change in the affinity coefficient given the standard enthalpy change for the process. The variation of the isosteric heat with the amount adsorbed suggests an energetically heterogeneous surface for the activated carbon as reported by Yun (2001) and Do (1998) for adsorption of DCM onto activated carbon fibre.

5.2.4.9. Diffusion coefficients

Of relevance to the model are five diffusion coefficients, namely the molecular diffusion coefficient, the axial diffusion coefficient, the Knudsen diffusion coefficient,

the surface diffusion and the effective diffusion coefficient. In line with other research, the phenomenon of surface diffusion is assumed not to occur.

Molecular (Maxwelian) diffusion coefficient (D_{mol})

Diffusion describes the net flux of molecules from a high concentration region to one of lower concentration. The consequence of diffusion is a gradual mixing of material. Predictive equations for the calculation of gas-phase diffusivity are available in the literature. A useful and reasonably accurate theoretical equation based on the kinetic theory of gases was suggested by Chapman and by Enskog (Cussler, 1997). The diffusion coefficient D_{AB} strongly depends upon binary interaction parameters of the A-B pair. The molecular diffusion coefficient for a binary mixture of gases may be obtained theoretically from the Chapman-Enskog equation (Cussler, 1997), and this equation is used to calculate the value of molecular diffusion coefficient for the air/DCM mixture.

$$D_{mol} = 0.0018583 T^{3/2} \frac{\sqrt{\left(\frac{1}{M_A} + \frac{1}{M_B}\right)}}{P \sigma_{AB}^2 \Omega} \qquad \text{(eq. 44)}$$

$$\sigma_{AB} = 1/2(\sigma_A + \sigma_B) \qquad \text{(eq. 45)}$$

where

P	=	pressure in atmospheres, Pa
M_A, M_B	=	molar masses of A and B, g mol^{-1}
T	=	temperature, K
σ_{AB}	=	collision parameter
Ω	=	parameter of the interaction of the 2 species

Sánchez-Liarte (2009) used this expression to calculate the molecular diffusion coefficient at ambient conditions. The parameters used in the equation for an air-DCM gas mixture are given in Table 4. The calculated molecular diffusion coefficient is 1.14 x 10^{-5} m^2 s^{-1} (Sánchez-Liarte, 2009).

Table 4. Values of parameters to calculate the molecular diffusion coefficient (Cussler, 1997)

Parameter	Value	Parameter	Value
$\sigma_{A\ (air)}$ [A]	3.711	T [K]	293
$\sigma_{B\ (DCM)}$ [A]	4.182	σ_{AB} [A]	3.9465
M_A [g mol^{-1}]	28.97	Ω	1.128
M_B [g mol^{-1}]	84.93	D_{mol} [m^2 s-^{1}]	1.14 x 10^{-5}

Crittenden, *et al*. (2011) used an empirical equation suggested by Fuller, Schettler and Giddings (1966) to calculate the molecular diffusion coefficient (D_{mol}). The calculated value of D_{mol} for DCM in air at 298K and 101 kPa was 1.05 x 10^{-5} m^2 s^{-1}, and this value is used in the current study. The Fuller, Schettler and Giddings (FSG) method is not only simple to use but also reasonably accurate in predicating binary gas-phase diffusivity up to moderate pressures. This method is based on the following formula:

$$D_{mol} = \frac{1.0133x10^{-7}T^{1.75}}{P\left[(\sum v)_A^{1/3} + (\sum v)_B^{1/3}\right]^2}\left[\frac{1}{M_A} + \frac{1}{M_B}\right]^{1/2} \qquad \text{(eq. 46)}$$

where

M_A, M_B = molar mass of A and B, respectively, g mol^{-1}

T = temperature, K

P = total pressure, Pa

V_A, V_B = molar volumes of air and the gas, mol m^{-3}

Axial dispersion coefficient (D_{ax})

The axial dispersion coefficient must be considered if plug flow with axial dispersion is assumed. The axial dispersion coefficient for laminar flow can be calculated from the molecular diffusion coefficient by means of the Taylor relation (Valdes-Solis, *et al*., 2004; Sánchez-Liarte, 2009):

$$D_{ax} = D_{mol} + \frac{1}{192}\frac{u^2 d^2}{D_{mol}} \qquad \text{(eq. 47)}$$

Knudsen diffusion (D_K)

Knudsen diffusion is related to the transport of molecules in the pores when the pore radius is less than the mean free path of fluid molecules. The flow in the pore decreases because of the resistance of the wall (Yang, 1987) and the Knudsen diffusivity is given by:

$$D_K = 97 r_{pore} \left(\frac{T}{MW} \right)^{\frac{1}{2}} \qquad \text{(eq. 48)}$$

where

r_{pore}	=	pore radius, m
T	=	temperature, K
MW	=	molar mass of the diffusing species, g mol^{-1}

Sánchez-Liarte (2009) calculated the Knudsen diffusion coefficient for DCM (having a molar mass of 84.93 g mol^{-1}) and obtained a value of 7.21×10^{-7} m^2 s^{-1} for a mean pore diameter of 0.8 nm for ACM and a temperature of 293K. This Knudsen diffusion coefficient (7.21×10^{-7} m^2 s^{-1}) is, as expected, lower than the molecular diffusivity of 1.14×10^{-5} m^2 s^{-1} calculated by Sánchez-Liarte (2009) and that of 1.05×10^{-5} m^2 s^{-1}obtained by Crittenden, *et al*. (2011).

Effective diffusion coefficient (D_{eff})

The effective diffusion coefficient or diffusivity (D_{eff}) lumps together the mechanisms of intra-particle mass transport (molecular & Knudsen), as it explains diffusion through the pore space of the monolithic porous media. It takes place at the macroscopic level, because it is not the individual pores but the entire pore space that is considered. Internal diffusion depends on the structure of the pores as molecules move randomly and takes place in the pore space.

The effective diffusion coefficient is normally the combination of the two mechanisms of intra-particle mass transport and depends on the structure of the pores. Both Knudsen diffusion and bulk flow can be described adequately for homogenous media. However, for a porous mass of solid containing pores of non-uniform cross

section, the flow follows a very tortuous path. Thus the flux for bulk and Knudsen diffusion is multiplied by a geometric factor which takes into account the tortuosity given the fact that the flow is obstructed by a fraction of the solid. An approximation of the effective diffusion coefficient (D_{eff}) given by Froment and Bischoff (1990) is calculated on the basis of a flux resulting from a concentration gradient in a homogeneous medium which is equivalent to a heterogeneous porous mass taking into account the geometric factor. This expression is called the Bosanquet equation (Shen, *et al*., 2011):

$$\frac{1}{D_{eff}} = \left(\frac{1}{D_{mol}} + \frac{1}{D_K} \right) \frac{\tau_p}{\varepsilon} \qquad \text{(eq. 49)}$$

where

τ_p = tortuosity factor

ε = void fraction

Tortuosity, as explained, is included because diffusion follows a zig-zag path. Taking into consideration a tortuosity of 65 (Chi, 1994) and a voidage of 0.44, the effective diffusion coefficient calculated for square channel monolith is 4.59 $x10^{-9}$ m^2 s^{-1}, using D_{mol} = 1.14$x10^{-5}$ m^2 s^{-1} and D_k = 7.21$x10^{-7}$ m^2 s^{-1} (Sánchez-Liarte, 2009). D_{eff} is equal to 4.57 $x10^{-9}$ m^2 s^{-1}, using D_{mol} = 1.05$x10^{-5}$ m^2 s^{-1} and D_k = 7.21$x10^{-7}$ m^2 s^{-1} (Crittenden, *et al*., 2011).

These values of D_{eff} are much higher that the value of D_{eff} which was obtained by using the LDF equation to interpret the rate of uptake of DCM on a monolith sample using an Intelligent Gravimetric Analyser at the University of Bath (Sánchez-Liarte, 2009). The D_{eff} was found to be equal to 4.5$x10^{-11}$ m^2 s^{-1}, that is, two orders of magnitude lower than the theoretically calculated values. The value of 4.5$x10^{-11}$ m^2 s^{-1} will be used for the time being.

5.2.4.10. Mass transfer coefficient (*k*)

A mass transfer coefficient correlates the mass transfer rate, mass transfer area and concentration gradient as the driving force. A mass transfer coefficient can be

estimated from many different theoretical equations and correlations. The criterion for selection of the most appropriate model is dependent on the material and the system. The mass transfer coefficient is introduced in the linear driving force expression of equation (eq. 23). The effective mass transfer coefficient to be used in equation (eq. 23) is comprised of a mass transfer coefficient internal to the adsorbent, namely k_e, and the film mass transfer coefficient external to the adsorbent, namely k_c. Both k_e and k_c are now presented for a monolith and will be discussed further in Chapter 6.

Internal mass transfer coefficient (k_e)

The internal mass transfer coefficient used in equation (eq. 23) is based on linear driving force assumptions, being approximated for the monolith by either slab geometry or by a geometric transformation from the square channel to a hollow cylinder impervious to mass at its outer radius. These two approximations are presented as follows:

(i) The mass transfer coefficient (k_e) is calculated for slab geometry according to the method of Glueckauf (1955) as presented by Yu, *et al.* (2007). For an isothermal slab geometry, the calculation is performed based on the following equation:

$$k_e = \frac{10 D_{eff} a_s}{e} \qquad \text{(eq. 50)}$$

where

k_e = mass transfer coefficient, s^{-1}

D_{eff} = effective carbon diffusion coefficient, $m^2 s^{-1}$

a_s = specific surface area, m^{-1}

e = wall thickness of the channel, m

(i) Patton, *et al.* (2004) obtained an expression derived from the LDF approximation to transform a monolith square channel geometry into that of an equivalent circular duct. The authors assumed that a square channel has the same surface area and wall volume per unit length as a cylindrical

channel. The geometry of the square channel was transformed into an equivalent hollow cylinder. The dimensions of the cylindrical channel, inner radius r_i and outer radius r_o, with an insulated external surface are shown in Figure 26. For the transformation, the wall thickness of the square channel is taken as half of the total wall thickness as diffusion into the channel occurs from all its sides.

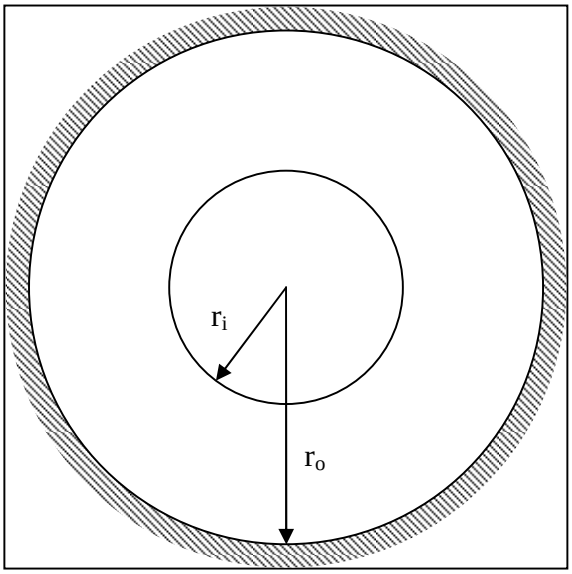

Figure 26. Hollow cylinder with insulated external surface (Patton, *et al*., 2004)

The mass transfer coefficient for the equivalent hollow cylinder for square channel with an insulated external surface is given by the following expression as developed by Patton, *et al*. (2004).

$$\frac{d\bar{q}}{dt} = \frac{4D_{eff}\left(q^{*}-\bar{q}\right)}{\left(\left(\left(r_o/r_i\right)-1\right)\left(r_o^2-r_i^2\right)-\left(1/r_i\left(r_o-r_i\right)\right)x\left[\left(1/2\right)\left(r_o^4-r_i^4\right)-\left(4r_o/3\right)\left(r_o^3-r_i^3\right)+r_0^2\left(r_{oi}^2-r_i^2\right)\right]\right)} \quad \text{and} \quad \text{(eq. 51)}$$

$$r_i = \frac{2d}{\pi} \quad \text{(eq. 52)}$$

$$r_o = \sqrt{\frac{4t_w}{\pi}\left(t_w+d\right)+r_i^2} \quad \text{(eq. 53)}$$

$$t_w = \frac{e}{2} \qquad \text{(eq. 54)}$$

where

r_i	=	internal radius of hollow cylinder, m
r_o	=	external radius of hollow cylinder, m
d	=	side length of channel, m
t_w	=	half wall thickness of the channel, m

The values calculated by the two methods will be presented and discussed later in Chapter 6.

External mass transfer coefficient (k_c)

The external mass transfer coefficient, that is for flow in the channel is obtained from correlations for the Sherwood number (*Sh*). Valdes-Solis, *et al*. (2004) and Grande and Rodrigues (2008) calculated the external mass transfer coefficient from the Sherwood number using the correlation proposed by Hawthorn (1974) for square channels:

Hawthorn: $$Sh = 2.976\left(1 + 0.095\,\mathrm{Re}\,Sc\frac{d}{L}\right)^{0.45} \qquad \text{(eq. 55)}$$

where

d	=	channel diameter, m
L	=	channel length, m
Re	=	Reynolds number
Sc	=	Schmidt number

Other equations are available for the calculation of external mass transfer coefficients such as the ones by Votruba, *et al.* (1975) (eq 56) and Bennett, *et al.* (1991) (eq. 57). Generally the correlation developed by Hawthorn (1974) is used for monoliths. Several studies demonstrated the suitability of the Hawthorn equation with monoliths as it

produced the best fit with the experimental data (Valdes-Solis, *et al*., 2004; Grande & Rodrigues, 2008; Sánchez-Liarte, 2009).

Votruba: $$Sh = 0.705\left(\mathrm{Re}\frac{d}{L}\right)^{0.43} Sc^{0.56} \qquad \text{(eq. 56)}$$

Bennett: $$Sh = 0.0767\left(1 + \mathrm{Re}\, Sc\frac{d}{L}\right)^{0.829} \qquad \text{(eq. 57)}$$

The Reynolds number (*Re*) measures the ratio of inertial forces to viscous forces and consequently characterizes the flow regimes whether laminar or turbulent. With a Reynolds number of 44, we conclude that the fully developed flow is laminar.

$$\mathrm{Re} = \frac{du_{ave}\rho_g}{\mu} \qquad \text{(eq. 58)}$$

where

μ = viscosity, kg s^{-1} m^{-1}

The Schmidt number (*Sc*) correlates the ratio of momentum diffusivity (viscosity) to mass diffusivity. It is utilized to describe fluid flows in which there are simultaneous momentum and mass diffusion convection processes. It physically relates the relative thickness of the hydrodynamic layer and the mass transfer boundary layer.

$$Sc = \frac{\mu}{\rho_g D_{mol}} \qquad \text{(eq. 59)}$$

The Sherwood number (*Sh*) is a dimensionless number utilized in mass transfer operations to represent the ratio of convective to diffusive mass transport as given by the following equation:

$$Sh = \frac{k_c d}{D_{mol}} \qquad \text{(eq. 60)}$$

The external mass transfer performance of a monolith can be enhanced by reducing the channel size, whereas, the internal mass transfer performance can be enhanced by reducing the wall thickness. Therefore, the objective is to make thin walled monoliths with high cell densities. Although, there will be manufacturing limitations in doing this.

5.2.4.11. Specific surface area (a_s)

The specific surface area is defined as the surface area of the solid-gas interface over the volume of the solid. The specific surface area for the whole monolith then amounts to:

$$a_s = \frac{4dL}{\left((d+e)^2 - d^2\right)L} \qquad \text{(eq. 61)}$$

$$a_s = \frac{4d}{e(e+2d)} \qquad \text{(eq. 62)}$$

where

a_s = specific surface area, m^{-1}

e = wall thickness of the channel, m

d = side length of channel, m

5.2.4.12. Thermal conductivity (λ)

The thermal conductivity indicates the ability of a material to conduct heat, and it depends on humidity and temperature. For MAST activated carbon monoliths which are structures with a bunch of channels full of air, the thermal conductivity coefficient decreases exponentially with an increase in temperature. The thermal conductivity coefficient of MAST ACM at 25ºC is 23 $Wm^{-1}K^{-1}$ while that of graphite is in the range of 50 - 150 $Wm^{-1}K^{-1}$ (Sánchez-Liarte, 2009). Kuwagaki, *et al*. (2003) measured the thermal conductivity of graphite activated carbon and obtained a very poor value of 0.17 W m^{-1} K^{-1}. Sánchez-Liarte (2009) reported the thermal conductivity (λ) for MAST activated carbon monolith to be equal to be 23 W $m^{-1}K^{-1}$ at 25°C and 18 W m^{-1} K^{-1} at 125°C.

5.2.4.13. Heat transfer coefficient between solid and gas (h_s)

The evaluation of the heat transfer coefficient between a fluid and solid has been the subject of much research especially in the domain of catalytic chemical reactions. A lot of correlations exist and are available in the literature. The choice of equation is important for the simulation of the adsorption process. The gas-solid thermal transfer coefficient is mainly expressed as a function of Nusselt number. The Nusselt number is the relation of convective to conductive heat transfer analogous with the Sherwood number, the dimensionless number for mass transfer.

$$Nu = \frac{h_s d}{\lambda_g} \qquad \text{(eq. 63)}$$

where

λ_g = thermal conductivity of the gas (pure nitrogen)

Yu, *et al.* (2007) used the correlation equation of Bennett, *et al.* (1991) that studied the oxidation in a monolithic catalyst and which is expressed as:

$$Nu = 0.0767\left(1 + \mathrm{Re}\,\mathrm{Pr}\frac{d}{L}\right) \qquad \text{(eq. 64)}$$

$$\mathrm{Re} = \frac{d u_{ave} \rho_g}{\mu} \qquad \text{(eq. 65)}$$

$$\mathrm{Pr} = \frac{c_p \mu \rho_g}{\lambda} \qquad \text{(eq. 66)}$$

The Nusselt correlation, presented in equation (eq. 63) is the heat transfer version of an analogous equation of the Sherwood number for mass transfer presented earlier in equation (eq. 60). For heat transfer, the Nusselt number (*Nu*) is written in term of the Reynolds number (*Re*) and the Prandtl number (*Pr*); while for mass transfer, the Sherwood number is a function of the Reynolds number (*Re*) and the Schmidt number

(*Sc*). The Schmidt number (*Sc*) for mass balance is analogous to a dimensionless number for heat transfer, the Prandtl number (*Pr*).

5.2.4.14. Heat capacity of solid (c_{ps})

The heat capacity is defined as the quantity of heat (in Joules) that is added or removed from a unit mass of that substance to alter its temperature by one degree. There is very little information about values of the specific heat for activated carbon. This value may be considered to range from 700 J kg^{-1} K^{-1} for carbon to 1000 J $kg^{-1}K^{-1}$ for an ACM with a binder (Yu, *et al.*, 2007).

The heat capacity of the solid c_{ps} is not constant according to Yu, *et al*. (2007). This heat capacity can increase by up to 70% at high loading. For the sake of simplification, the heat capacity of the solid c_{ps} is assumed to be constant for the current study and is assumed to be that of the carbon. From the literature, the heat capacity of carbon (graphite) is c_{pc} = 711 J kg^{-1} K^{-1}. Yu (2003) and Yu, *et al.* (2007) reported a value of 1000 J kg^{-1} K^{-1} from Bonnissel (1997).

5.2.4.15. Heat capacity of gas (c_{pg})

According to Yu (2003) and Yu, *et al*. (2007), the heat capacity of the gas c_{pg} is dependent on the concentration of its constituents. Again for the sake of simplification, the heat capacity of the gas (c_{pg}) is assumed to be constant and to be that air (c_{pa}) for adsorption and that of nitrogen (c_{pn}) for desorption.

5.2.5. Cyclic process equations

Based on the findings in the literature, process modelling of the ESA cycle for the recovery of VOC on activated carbon monoliths can be considered to be one element of the novelty of the present study. Mathematical modelling of the cyclic process involves executing the adsorption and desorption equations in sequence from start-up. Results will be provided in Chapter 6.

Two factors, time and concentration, can be considered limiting in the cyclic process. Both adsorption and desorption processes can be executed consecutively, for example, for a duration of 30 minutes for each step.

In addition to the equations presented above for adsorption and desorption and the limiting factor that ensures the transition between the two processes, other parameters have to be set for the cyclic process to run smoothly. These parameters include the ones that have to be reset after each cycle. The modelling software imposes the modelling structure as described in the following section.

The cyclic process is complete if heating is conducted after adsorption and a cooling process is conducted after desorption. For the heating process by passing electric current, the monolith needs to reach a maximum temperature of 200°C. The cooling time, on the other hand, is relatively slow in comparison to the heating time.

5.3. gPROMS presentation

Mathematical modelling involves building a number of models which are tested and validated individually. Individual models are combined together and simulated at steady state conditions. After having all elements of the overall process in place, dynamics and cyclic operations are introduced. The flexibility provided in gPROMS is that model development is established incrementally from the simpler models towards the overall goal of modelling the complete cyclic steady state and dynamic processes.

5.3.1. Project

The first step taken in modelling the ESA process is to create a gPROMS "Project". Within the created project, a tree of entities is opened, and to get started three entries are needed: variable types, model, and process. Other entries are added and/or explored upon the first building block. Figure 27 shows the overall presentation of gPROMS.

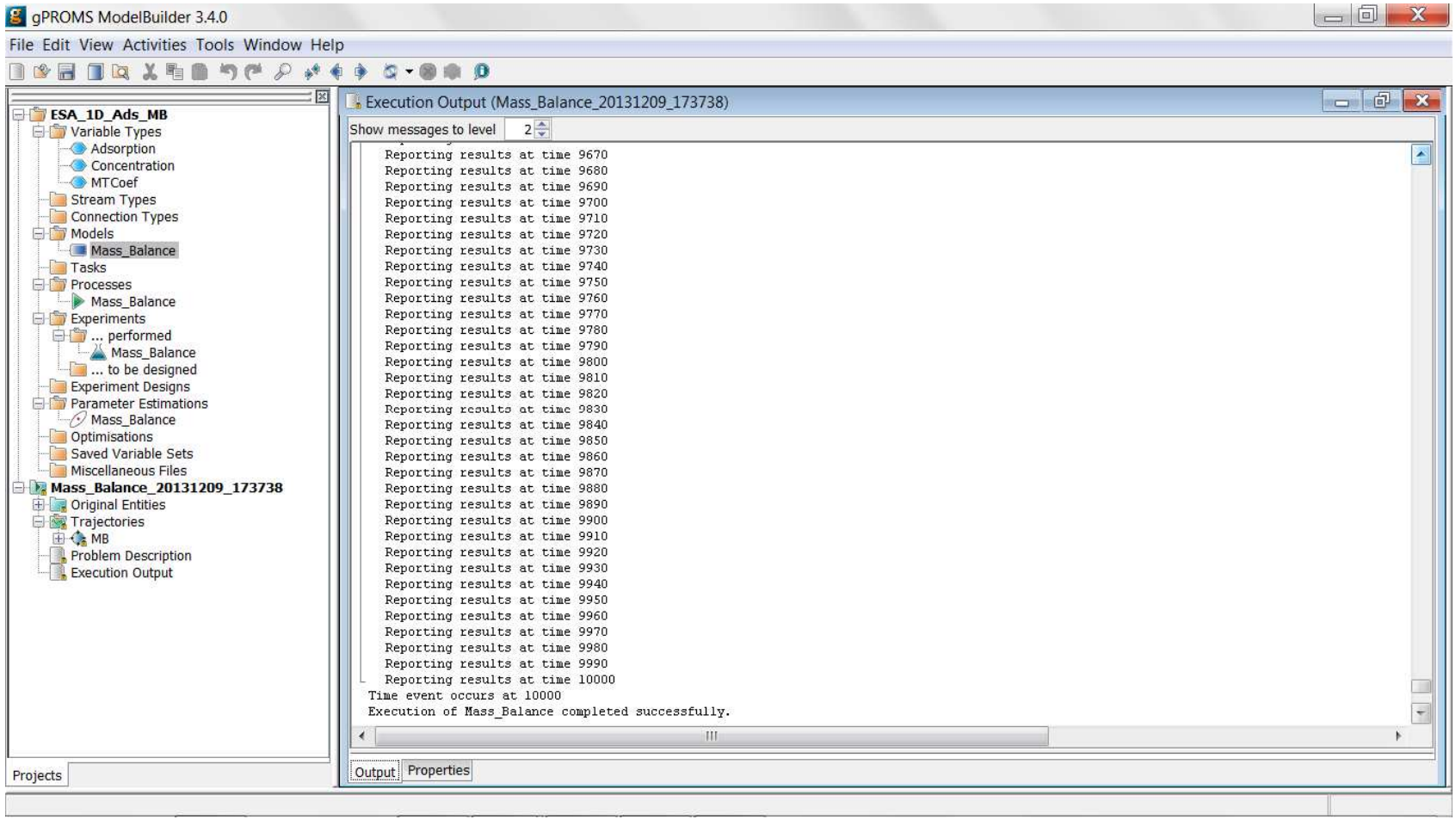

Figure 27. Overall presentation of gPROMS

5.3.2. Variable types

The "Variable Types" is the first entity in the gPROMS project. This entry lists the variables used in the model. Each variable is declared to be of a particular type, and it is user-defined. For the illustrated project for example, two variables are defined: concentration in the gas phase and adsorption in the solid.

5.3.3. Model

The Model contains a mathematical description of the physical behaviour of the ESA process and comprises a number of sections, each containing a different type of information regarding the system being modelled. The Model performs the following functions for the tested Process:

- Set the constant parameters used in the modelling equations.
- Identify the variables that will be calculated by the modelling equations.
- Describe the distribution domain over which the calculation will be made.
- Set the boundary conditions.
- Write out the equations used in the model.

In the Model entry, the physical behaviour of the system is defined. But a Model can be used to study the behaviour of the system under many different circumstances. Each specific situation is called a simulation activity. The coupling of model with a dynamic simulation activity is done in the Process entity.

5.3.4. Process

A Process is partitioned into sections. Each section contains information required to define the corresponding dynamic simulation activity such as:

- Set up a dynamic simulation activity by specifying the unit section of a process.
- Set appropriate values to all the parameters of the model.
- Determine the initial values for the system variables at time equals to zero before the dynamic simulation can commence.

- Provide the information on the external manipulations that are to be simulated in the schedule section of the process.

For the separate adsorption and desorption processes, a Model and a Process were defined for each in order for the separate processes to run independently. The two processes can be run separately for parametric estimation and operation condition studies. These two processes then are combined to simulate the integral cyclic process using Tasks.

5.3.5. Task

The cyclic operation is introduced in gPROMS using tasks, which are utilized to simulate different scenarios. For the cyclic process, in addition to the model and the process, two Tasks were defined. One defines how a cycle should proceed in sequence while, the other defines column operation. The Task is a model of an operating procedure that can be considered as a recipe that defines periods of undistributed operation along with external disturbances to the system. A Task

- Can be re-used multiple times during a dynamic simulation.
- Can involve other tasks and thus complex operating procedures can be defined in a hierarchical manner.

5.3.6. Parameter estimation

Parameter estimation is also performed using gPROMS project. A detailed gPROMS process model is developed from equations describing the physical and chemical phenomena that occur in the system. These equations typically engage parameters that can be attuned to make the model predictions match the experimental data. The accuracy of these parameters enhances model performance in predicting real data. The fitting of these parameters to experimental data obtained from the laboratory or the plant is named parameter estimation.

Parameter Estimation problem makes use of the data gathered from a set of experimental data. The Performed Experiment entity is used to specify the full details of

an experiment using both dynamic and steady state experimental data. In the Performed Experiment the controlled variables and measured data are specified. The Performed Experiment is then simulated.

The complete specification of a Parameter Estimation requires some additional information such as the unknown parameters to be estimated, define the experiment used and the sensor specifications.

Based on the gPROMS presentation for the different entities, the modelling of adsorption, desorption and cyclic processes are executed using the modelling equations and parameters. The resulting output is discussed in the Chapters that follow.

5.4. References

Bennett, C. J., Kolaczkowski, S. T. & Thomas, K. M., 1991. Determination of heterogeneous reaction kinetics and reaction rates under mass transfer controlled conditions for a monolith reactor. *Trans. I. Chem. E.*, 69(B), pp.209-220.

Bonjour, J., Clausse, M. & Meunier, F., 2005. A TSA process with indirect heating and cooling: parametric analysis and scaling-up to practical sizes. *Chemical Engineering and Processing*, 44, pp.969-977.

Bonnissel, M. 1997. Adsorption de Gaz Modulée en Température par des Eléments Thermoélectrique à Effet Peltier, Thèse de L'INPL, Nancy.

Camus, O., Crittenden, B., Perera, S., Mays, T., Sánchez-Liarte, F., Patsos, A., Tennison, S. R. & Crezee, E., 2007. Non-uniformities in adsorbent monoliths, *In: 9th International conference on Fundamentals of Adsorption*, 20 - 25 May. Giardini Naxos, Sicily.

Chi, T. 1994. *Adsorption calculation and modelling*. Butterworth-Heinemann.

Clausse, M., Bonjour, J. & Meunier, F., 2004. Adsorption of gas mixture in TSA adsorbers under various heat removal conditions. *Chemical Engineering Science*, 59, pp.3657-3670.

Crittenden, B. D., Camus, O., Perera, S. P., Mays, T. J., Sánchez-Liarte, F., Tennison, S. R. & Crezee, E., 2011. Nonuniform channels in adsorbent monoliths. *AIChE Journal*, 57(5), pp.1163-1172.

Crittenden, B., Perera, S., Mays, T., Camus, O. & Tennison, S., 2005. Monolithic adsorbents in sustainable development. *In*: *world Congress of Chemical Engineering*, *7th*, 10 - 14 July, Glasgow.

Cussler, E. L. 1997. Diffusion: mass transfer in fluid systems. Cambridge University Press.

Do, D. D. 1998. *Adsorption analysis: Equilibria and Kinetics*. Volumn 2. Imperial College Press. London.

Froment, G. F. & Bischoff, K. B. 1990. *Chemical reactor for analysis and design* Wiley.

Fuller E. N., Schettler, P. D. & Giddings, J. C. 1966. A new method for prediction of binary gas phase diffusion coefficient. *Ind. Eng. Chem.*, 58, pp.19-27.

Glueckauf, E. 1955. Part 10 – Theory of chromatography. Formula for diffusion into spheres and their application to chromatography. *Trans Faraday Soc*, 51, pp.1540-1551.

Grande, C. A, & Rodrigues, A. E., 2008. Electric swing adsorption for CO2 removal from flue gases. *International Journal of Greenhouse Gas Control*, 2(2), pp.194-202.

Groppi, G., Tronconi, E., Berg, M., Forzatti, P., 2000. Development and application of mathematical models of pilot-scale catalytic combustors fuelled by gasified biomass. *Industrial and engineering Chemistry Research*, 39, 00. 4106 – 4113.

Hawthorn, R. D. 1974. Afterburner catalysts-effects of heat and mass transfer between gas and catalyst surface. *AIChE Symp. Ser. Recent Advances in Air Pollution Control*, 137 (70), pp.428-438.

Kuwagaki, H., Meguro, T., Tatami, J., Komeya, K. & Tamura, K. 2003. An improved of thermal conduction of activated carbon by adding graphite. *Journal of Materials Science*, 38 (15), pp.3279-3284.

Menard, D., Py, X. & Mazet, N., 2007. Activated carbon monolith of high thermal conductivity for adsorption processes improvement Part B. Thermal regeneration. *Chemical Engineering and Processing*, 46(6), pp.565-572.

Patton, A., Crittenden, B. D. & Perera, S. P., 2004. Use of the linear driving force approximation to guide the design of monolithic adsorbents. *Chemical Engineering Research Des.*, 82, pp. 999-1009.

Petkovska, M., Antov-Bozalo, D., Markovic, A. & Sullivan, P., 2007. Multiphysics modeling of electric-swing adsorption system with in-vessel condensation. *Adsorption*, 13(3-4), pp.357 -372.

Sánchez-Liarte, F., 2009. *Performance of electrically regenerable monolithic adsorbents for VOC control*. Ph.D. thesis: University of Bath.

Shen, C., Yu, J., Li., P. Grande, C. A. & Rodrigues, A. E., 2011. Capture of CO2 from gas by vaccum pressure swing adsorption using activated carbon beads. *Adsorption*, 17(1), pp. 179-188.

Valdés-Solís, T., Linders, M., J. G., Kapteijn, F., Marban, G. & Fuertes, A. B., 2004. Adsorption and breakthrough performance of carbon-coated ceramic monoliths at low concentration of *n*-butane. *Chemical Engineering Science***,** 59(13), pp.2791-2800.

Votruba, J., Mikus, O., Nguen, K., Hlavacek, V. & Skrivanek, J., 1975. Heat and mass transfer in honeycomb catalyst II. *Chemical Engineering Science*, 30 (2). pp.201-206.

Yang, R. T. 1987. Gas separation by adsorption process, Butterworth, Boston.

Yu, F. D., 2003. *Adsorption de composés organiques volatils sur un monolithe de charbon actif avec régénération thermique par effect Joule*. Ph.D. Thesis, Ecole Nationale Superieur des industrie chimiques, Laboratoire des Sciences du Génie Chimique, L'institut National Polytechnique de Lorraine, France.

Yu, F. D., Luo, L. A. & Grevillot, G., 2007. Electrothermal swing adsorption of toluene on an activated carbon monolith: Experiments and parametric theoretical study. *Chemical Engineering and Processing: Process intensification*, 46 (1), pp.70-81.

Yun, J. H., 2001. Equilibrium Isotherms of Dichloromethane, Trichloroethylene, and 1,1,1-Trichloroethane on activated Carbon Fibre. 46. pp.156-159.

Chapter 6

One-dimensional modelling result

This Chapter presents the results obtained using the one dimensional model described in the previous Chapter. The modelled adsorption and desorption breakthrough curves are then compared with the experimental breakthrough curves obtained at the bench and pilot scales of the University of Bath for validation. The modelled breakthrough curves are also validated for another VOC namely toluene using the experimental data obtained from Yu (2003) and Yu, *et al*. (2007). Based on the validated adsorption and desorption breakthrough curves, the cyclic process is modelled, and the effects of varying the cycle time, the initial concentration and the regeneration temperature are studied.

6.1. Adsorption process simulation

6.1.1. Validation of adsorption on the bench scale

The mass balance model presented in the previous Chapter produces the breakthrough curve related to adsorption. The resulting breakthrough curve is compared with that produced experimentally at the University of Bath and both curves are illustrated in Figure 28. Details of the monolith, operating conditions and other parameters are provided in Tables 2 and 3 of Chapter 5.

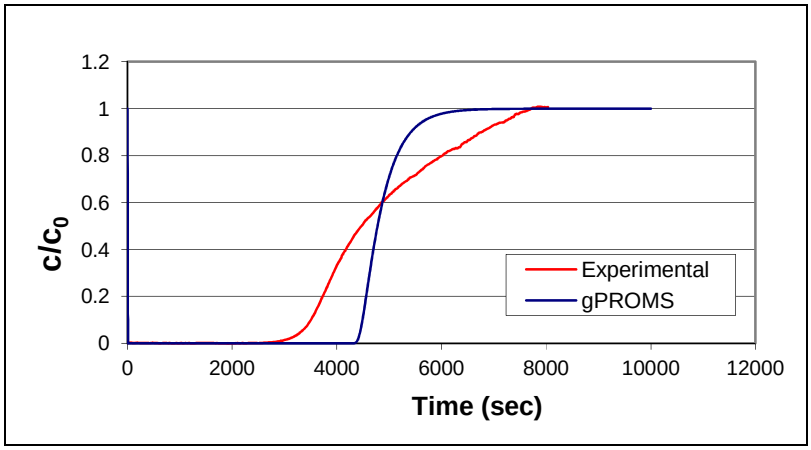

Figure 28. Experimental vs. gPROMS modelled breakthrough curves at bench scale

The experimental breakthrough curve is obtained from the bench scale apparatus using a 10.3 cm in length square channel monolith. The modelled breakthrough curve is obtained based on the mass and energy balance equations presented in Chapter 5. It is clear that the gPROMS modelled curve does not produce a good fit with the experimental data. Accordingly, an investigation of various parameters is required in order to obtain a better fit of the experimental data.

6.1.1.1. Statistical analysis

The deviation between the experimental and modelled breakthrough curve is quantified using the coefficient of determination R^2. In statistics, R^2 provides a measure of how well experimental data are likely to be predicted by the model. In general, the experimental data has values of y_i, each of which has an associated modelled value f_i. Here, the modelled values f_i are those resulting from gPROMS modelling. The variability of the data set is measure through different sums of squares. The total sum of squares is given by the following equation:

$$SS_{tot} = \sum_i \left(y_i - \bar{y}\right)^2 \qquad \text{(eq. 67)}$$

The sum of squares of the residuals is calculated as follows:

$$SS_{err} = \sum_i (y_i - f_i)^2 \qquad \text{(eq. 68)}$$

where the mean of the experimental data is expressed by the following equation in which *n* is the number of observations:

$$\bar{y} = \frac{1}{n}\sum_i^n y_i \qquad \text{(eq. 69)}$$

The most general definition of the coefficient of determination then amounts to the following expression:

$$R^2 = 1 - \frac{SS_{err}}{SS_{tot}} \qquad \text{(eq. 70)}$$

The coefficient of determination for the curve presented in Figure 28 has a value of 0.831. The deviation of this coefficient from one shows its weakness. Values close to one, in the range of 0.9 and higher for example, are more acceptable and demonstrate a better fit to the experimental data being modelled.

6.1.1.2. Parametric study

The mass balance developed in equations (eq. 22 and 23) is presented now as equation (eq. 71). The parametric study involves the study of all the important parameters involved in the mass balance equation in order to assess their impact and analyze the results of their variation. Some parameters have a minor impact on the breakthrough curve whereas others can dramatically change the shape of this curve.

$$\frac{\partial c}{\partial t} - D_{ax}\frac{\partial^2 c}{\partial x^2} + u_{ave}\frac{\partial c}{\partial x} + \frac{1-\varepsilon}{\varepsilon}\rho_s k\left[\left(q_m \frac{bPc/\rho_s}{\left(1+(bPc/\rho_s)^t\right)^{1/t}}\right) - q\right] = 0 \qquad \text{(eq. 71)}$$

All the parameters of the mass balance equation (D_{ax}, u_{ave}, ε, ρ_s, q_m, b, t, k) are considered for the parametric study as follows.

It is observed in Figure 29 that any change in the axial dispersion coefficient (D_{ax}) has no impact on the breakthrough curve. Indeed, the breakthrough curves for the tested D_{ax} values are all superimposed. The interstitial velocity (u_{ave}), on the other hand, is an operating condition. Basically, changing the velocity affects the time to breakthrough. The faster the gas flows inside the monolithic channel the shorter is the time to breakthrough. Due to the faster gas flow, the monolith gets saturated faster causing the time to breakthrough to decrease. The change in the gas flow is nonlinear to the change in the time to breakthrough, as illustrated in Figure 30. For the slower flow rates, the deviation in the time to breakthrough becomes longer.

The porosity (ε) and the density of the solid (ρ_s) are characteristic parameters of the studied monolith. Even though it is outside the scope of this work to change the tested monolith, optimisation of ACM manufacturing detailed in Chapter 3 remains of primary importance to the current research. The effect of the porosity and the density of the solid are illustrated in Figures 31 and 32, respectively. As expected the more porous the activated monolith is, the time to breakthrough is observed to be shorter. The surface area increases with increasing porosity resulting in a higher capacity to adsorption, and breakthrough is achieved in a shorter time, as illustrated in Figure 31. An estimated 10% increase or decrease in the porosity results in a shift of breakthrough time by around 15 minutes. This relationship, however, is nonlinear as the increase in porosity is not proportional to the decrease in time to breakthrough. On the other hand, the density of the solid is linearly proportional to the breakthrough time, as observed in Figure 32. The higher the solid density, the time to breakthrough is observed to be longer, as the adsorption capacity of a less dense solid is lower than that of a denser solid.

The maximum amount adsorbed (q_m), the affinity (b) and Tóth (t) parameters are parameters of the Tóth adsorption isotherm. These values are obtained experimentally from the IGA of the laboratory of the University of Bath (Crittenden, *et al*., 2011). These parameters are interrelated, but their effects are considered separately. The maximum amount adsorbed is linearly proportional to the increase of time to breakthrough. Higher capacity of adsorption translates into an increase in time to breakthrough, as observed in Figure 33. The affinity parameter also has an impact on the time to breakthrough. However, a larger affinity parameter results in a longer time to breakthrough, as the

larger the affinity coefficient the more molecules are attached to the surface of the activated monolith which delays breakthrough. However the impact of the affinity parameter is minimal as can be observed in Figure 34. Similarly to the affinity parameter, a larger Tóth coefficient results in a longer time to breakthrough. However, the relationship between Tóth coefficient and time to breakthrough is nonlinear as shown in Figure 35.

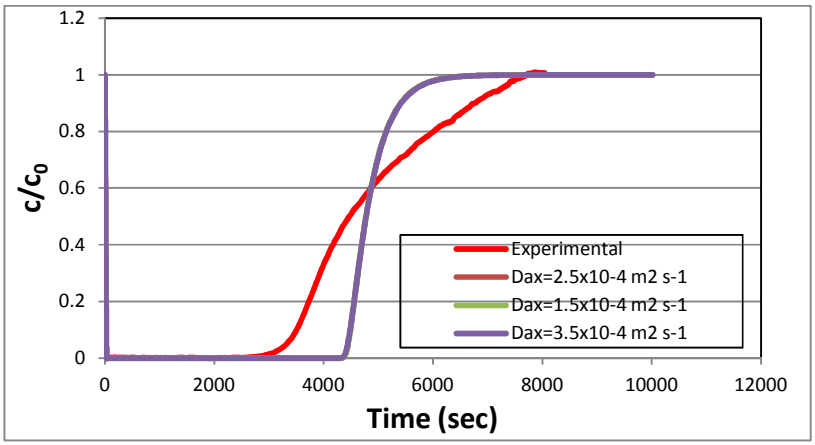

Figure 29. Effect of axial dispersion coefficient on modelled breakthrough curve

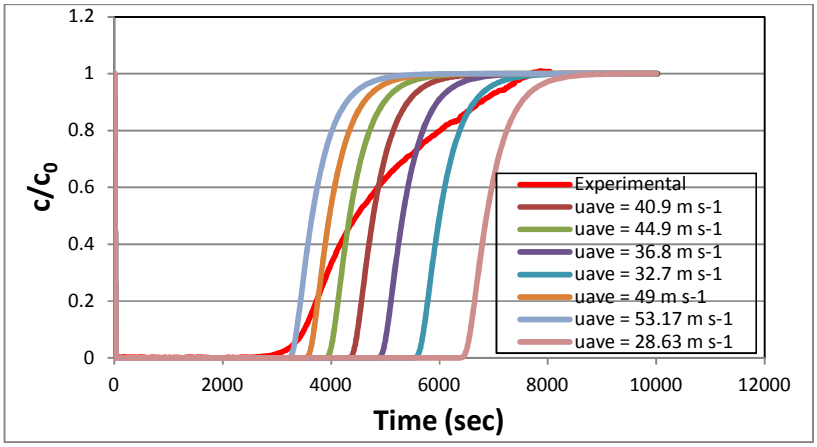

Figure 30. Effect of interstitial velocity on modelled breakthrough curve

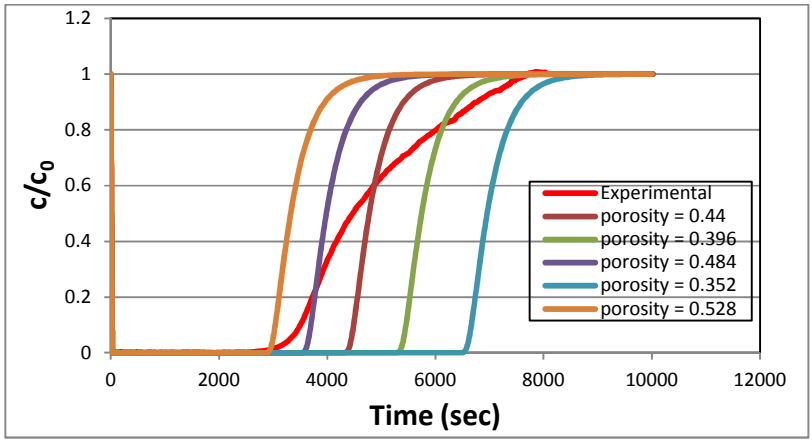

Figure 31. Effect of porosity on modelled breakthrough curve

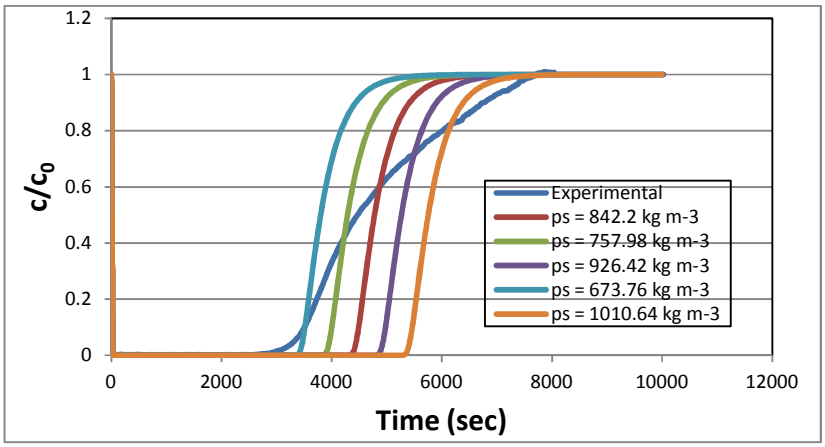

Figure 32. Effect of density on modelled breakthrough curve

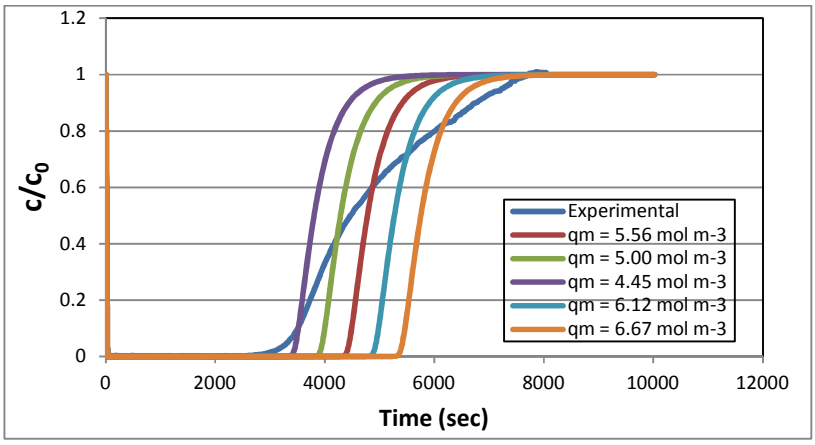

Figure 33. Effect of maximum amount adsorbed on modelled breakthrough curve

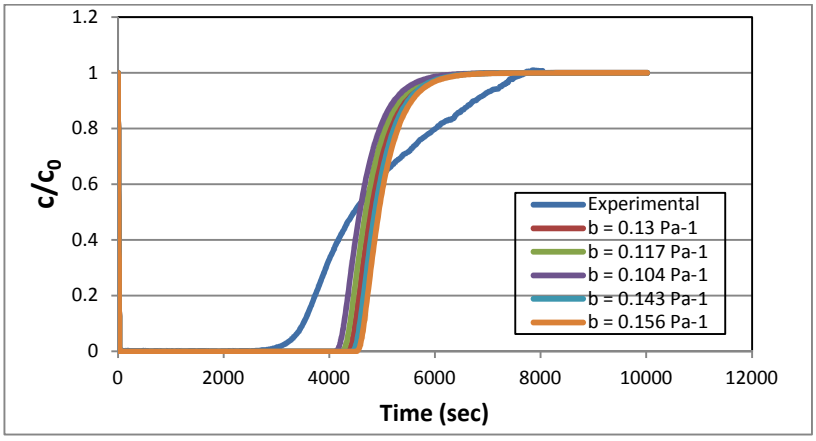

Figure 34. Effect of affinity coefficient on modelled breakthrough curve

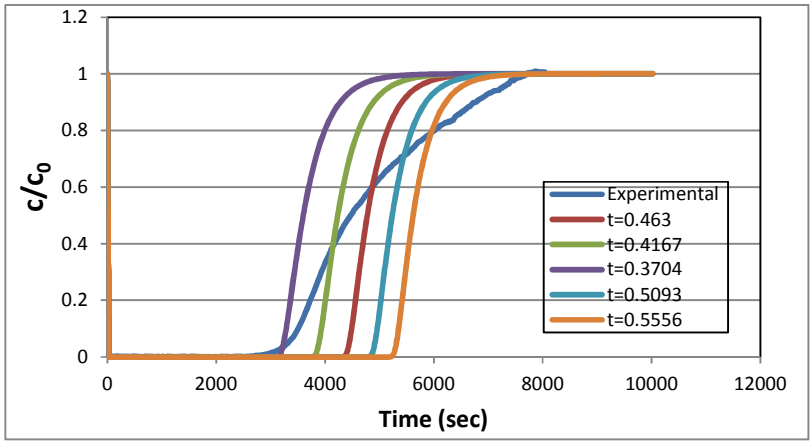

Figure 35. Effect of Tóth parameter on modelled breakthrough curve

Because all parameters associated with the design of the monolith and the experimental operating conditions cannot be altered arbitrarily, the only parameter whose value is uncertain is the mass transfer coefficient, *k*. Background research reveals that the principal term that has a major impact on the breakthrough curve is indeed the mass transfer coefficient. Brosillon, *et al*. (2001) confirmed that a good agreement between experimental and numerical results is found when an adjustable value of the internal mass-transfer coefficient is used. Brandani, *et al*. (2004) also observed that dispersion in monoliths is shown to be controlled by mass transfer resistance rather than by axial mixing. Therefore, the mass transfer coefficient (*k*) will be studied in more detail in the sections that follow.

6.1.1.3. Parameter estimation and evaluation of mass transfer coefficient (*k*)

Parameter estimation is a study that evaluates the parameters used in the equation in order for this equation to produce a breakthrough curve that can match the experimental data using the tested monolith at the operating condition of the experiment. Based on the parametric study, the mass transfer coefficient has the greatest impact on the breakthrough curve and can influence its shape. The mass transfer coefficient k comprises resistances to mass transfer external and internal to the adsorbent. The coefficients for these resistances are k_c and k_e, respectively.

Two values for the internal mass transfer coefficients (k_e) were calculated in the last Chapter and are shown in Table 5. These coefficients were calculated based on the predictions presented by Patton, *et al*. (2004) and Glueckauf (1955 cited in Yu, *et al*., 2007). The effect of using these two values on the breakthrough curve is shown in Figure 36. In addition, two arbitrary other values (0.0005 and 0.0008) were tested to see their effects.

Table 5. Values of mass transfer coefficients

Method	k_e **(s^{-1})**
Patton *et al*. (2004)	0.00326
Glueckauf (1955)	0.00588

As can be seen in Figure 36, the effect of altering the internal mass transfer coefficient has a great impact on the shape of the predicted breakthrough curve. For a mass transfer coefficient of 0.0008 s^{-1}, the resulting breakthrough curve compared best with the experimental curve.

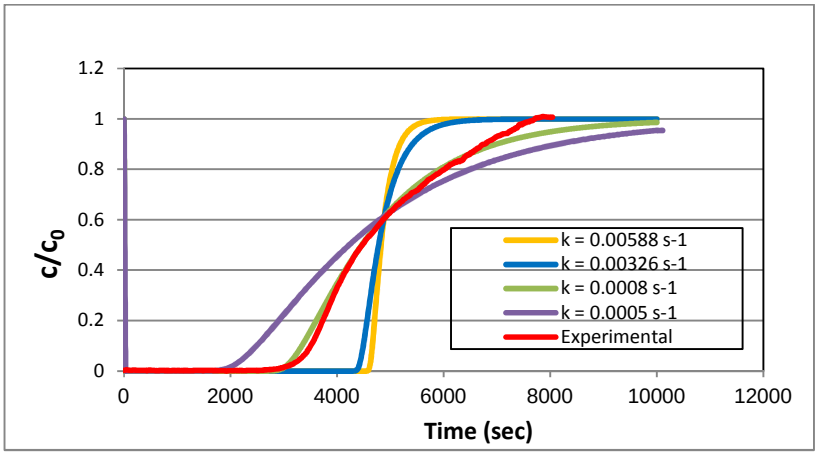

Figure 36. Effect of mass transfer coefficient

The deviation from experimental data is quantified in Table 6 using the coefficient of determination R^2. The R^2 values for the different values of k_e are shown in Table 6 and confirm the fact that a k_e value of 0.0008 s^{-1} produces a breakthrough curve that compares best with the experimental breakthrough curve. The coefficient of determination resulting from a k_e value of 0.0008 s^{-1} values 0.972 and is the closest to 1.0 in comparison to the other coefficients studied.

Table 6. Coefficient of determination

s^{-1}	k_e = 0.0058	k_e = 0.0033	k_e = 0.0008	k_e = 0.0005
R^2	0.806	0.831	0.972	0.909

6.1.1.4. Sensitivity analysis of mass transfer coefficient (*k*)

Although correlations are available to estimate the value of the mass transfer coefficient, other researches have also considered *k* to be an adjustable parameter. For example, Clause *et al*. (2004) studied the numerical and experimental breakthrough curves for different values of mass transfer coefficient (from 0.005 to 1 s^{-1}). As shown in Figure 37, the numerical breakthrough curves for k = 0.01 and 0.005 s^{-1} are too dispersive when compared with the experimental ones. For higher values, the numerical curves agree well with the experimental measurements. A higher value of *k* corresponds to a stiff numerical problem. The effect of mass transfer coefficient is only noticeable for

small values. This is because for the experimental setup of Clause, *et al*. (2004), the cycle times are long for which the sensitivity to global pellet mass transfer is usually much stronger (Clause, *et al*., 2004).

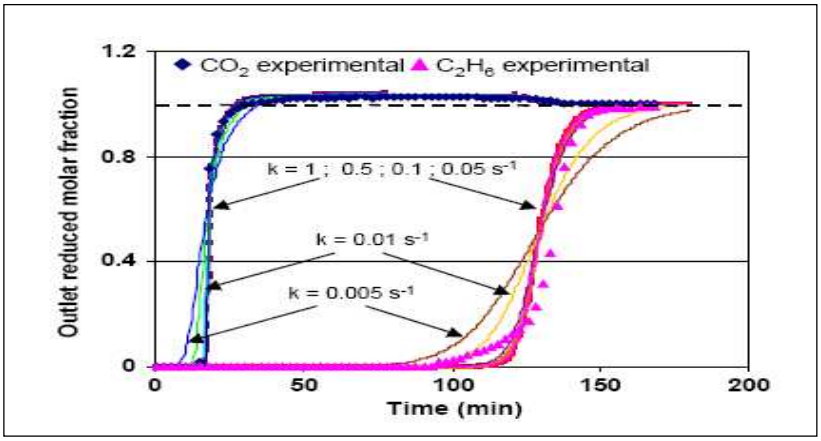

Figure 37. Influence of the mass transfer coefficient on the breakthrough prediction (Clause, *et al*., 2004)

Based on the sensitivity analysis, a *k* value of 0.0008 s^{-1} is chosen for the current study. Later, it will be shown that parameter estimation using gPROMS will provide a more precise value of *k*.

6.1.1.5. Validation of mass transfer coefficient at different operating conditions

As was shown in Figure 36, the mass transfer coefficient has a major impact on the breakthrough curve and can dramatically alter its shape. A value of 0.0008 s^{-1} was chosen based on the figure. To validate the chosen value, it is tested at different operating conditions in order to ensure that the modelled data fit the experimental results. The mass transfer coefficient value of 0.0008 s^{-1} was tested on three operating conditions with flow rates of 5 l min^{-1}, 7 l min^{-1} and 9 l min^{-1}. The comparisons are shown in Figures 38, 39, and 40, respectively. The parameters used for the three operating conditions are shown in Table 7.

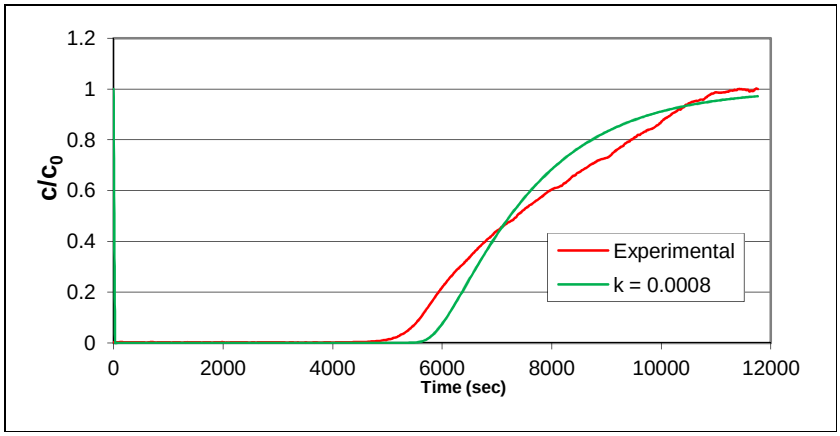

Figure 38. Experimental vs. modelled breakthrough curves at Q = 5 l min^{-1} using k_e = 0.0008 s^{-1}

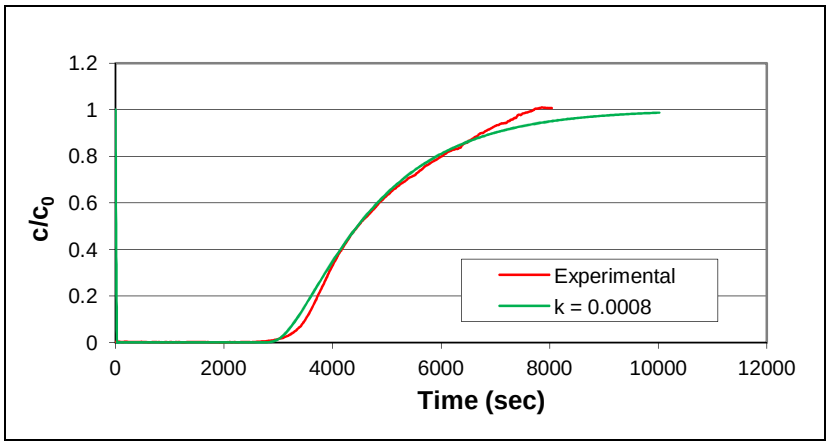

Figure 39. Experimental vs. modelled breakthrough curves at Q = 7 l min $^{-1}$ using k_e = 0.0008 s^{-1}

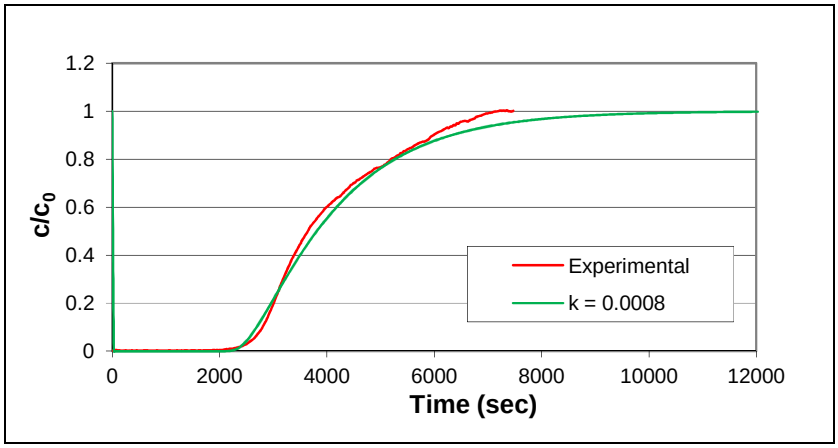

Figure 40. Experimental vs. modelled breakthrough curves at Q = 9 l min^{-1} using k_e = 0.0008 s^{-1}

Figures 38, 39 and 40 show that when k_e = 0.0008 s^{-1}, the fits for the higher flow rates of 7 l min^{-1} and 9 l min^{-1} are good while the fit for a flow rate of 5 l min^{-1} is poorest.

Table 7. Operating conditions

Parameters	**Q = 5 l min^{-1}**	**Q = 7 l min^{-1}**	**Q = 9 l min^{-1}**
Actual Q (l min^{-1})	4.7	7.2	8.7
u_m (mol m^{-2} s^{-1})	26.6	40.9	49
c_0 (ppmv)	1950	2000	1910

Figures 41, 42 and 43 show that when k_e= 0.00033 s^{-1} as calculated by Patton, *et al.*, (2004), the fits to the experimental data are very poor when compared with the chosen value of k_e = 0.0008 s^{-1}.

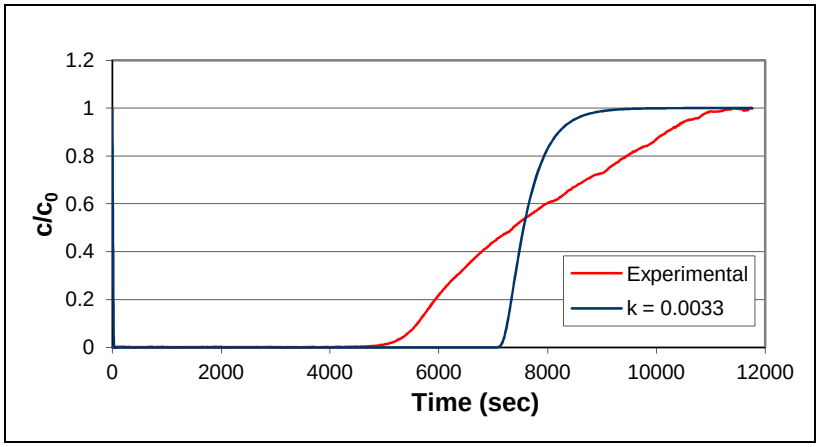

Figure 41. Experimental vs. modelled breakthrough curves at Q = 5 l min^{-1} using k_e = 0.0033 s^{-1}

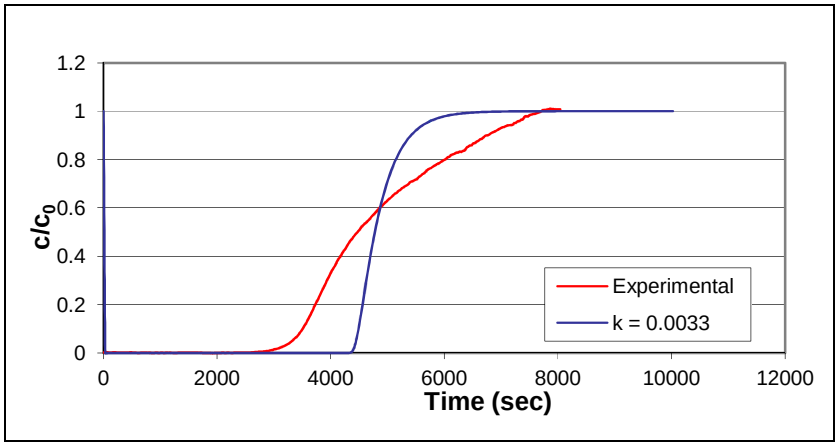

Figure 42. Experimental vs. modelled breakthrough curves at Q = 7 l min^{-1} using k_e = 0.0033 s^{-1}

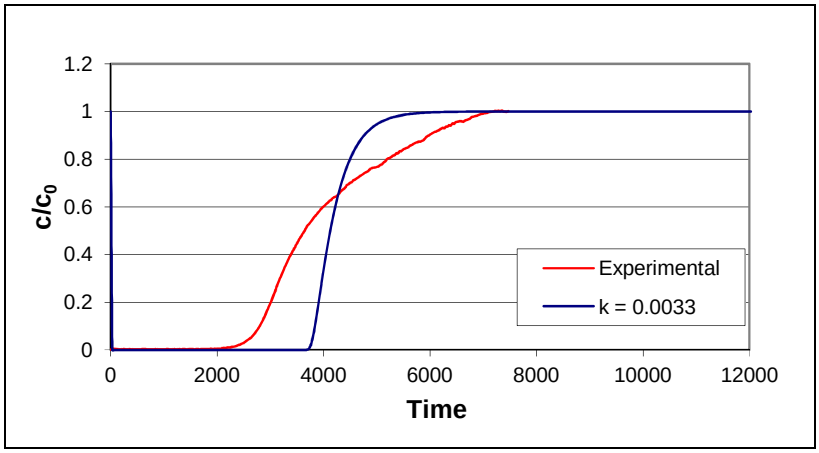

Figure 43. Experimental vs. modelled breakthrough curves at Q = 9 l min^{-1} using k_e = 0.0033 s^{-1}

The coefficients of determination (R^2) are shown in Table 8 for the three different flow rates in l min^{-1} (5, 7 & 9) using the two values of mass transfer coefficient (0.0033 & 0.0008 s^{-1}). The coefficient (R^2) shows which mass transfer coefficient provides a better prediction of the experimental data. As can be seen in the Table, the mass transfer coefficient of 0.0033 s^{-1} provided by Patton, *et al*. (2004) gives a poorer prediction in comparison to a mass transfer coefficient of 0.0008 s^{-1}. Based on these findings, it can be concluded that Patton's correlation for mass transfer coefficient is not suitable for the 1D mass balance model.

Table 8. Coefficient of determination

R^2	Q = 5 l min^{-1}	Q = 7 l min^{-1}	Q = 9 l min^{-1}
k_e = 0.0033	0.792	0.831	0.798
k_e = 0.0008	0.961	0.972	0.969

6.1.1.6. gPROMS parameter estimation of mass transfer coefficient

In addition, parameter estimation for k_e was conducted for the 1D model using gPROMS. This estimation is established using the experimental breakthrough data for the flow rate of 7 l min^{-1}. Under the performed experiment entry, the controlled variable and measured data are specified. Upon simulating this experiment, a new process is

generated using the initial conditions and controls defined in the experiment. Under the parameter estimation entry, the parameter to be estimated is identified. Upon the execution of the estimation, a parameter estimation report is generated displaying the final value of the parameter to be estimated along with the calculation of the variance and the goodness of fit.

The gPROMS parameter estimation report gave a final predicted value of 0.00087459 s^{-1} for the mass transfer coefficient (k_e). For this value, the modelled 1D curve is presented in Figure 44. The predicted curve compares well with the experimental one with a 0.9738 coefficient of determination for the operating condition of 7 l min^{-1}.

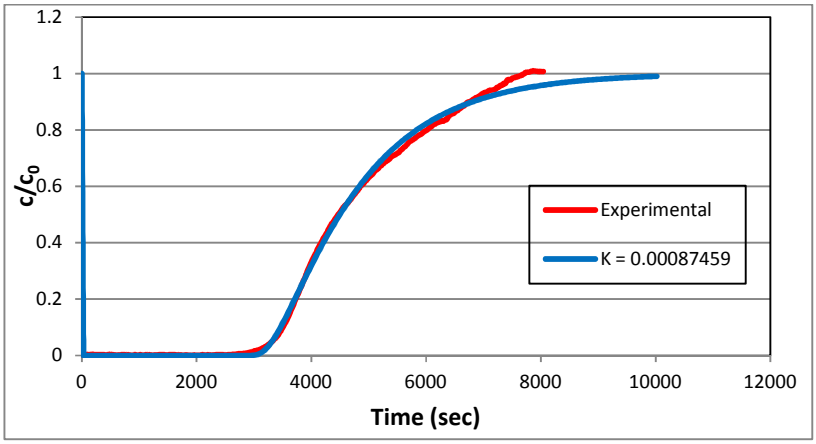

Figure 44. 1D breakthrough curve at 7 l min^{-1} (k_e = 0.00087459)

The predicted value of mass transfer coefficient obtained by gPROMS parameter estimation (k_e = 0.00087459 s^{-1}) is tested with the other operating conditions of 5 l min^{-1} and 9 l min^{-1}. The resulting breakthrough curves are presented in Figures 45 and 46, respectively. As concluded earlier, this mass transfer coefficient of 0.00087459 s^{-1} is best suited for the breakthrough curve resulting from a flow rate of 7 l min^{-1}. The fit is slightly poorer for 9 l min^{-1} (Figure 46), and the fit is worse for 5 l min^{-1} (Figure 45).

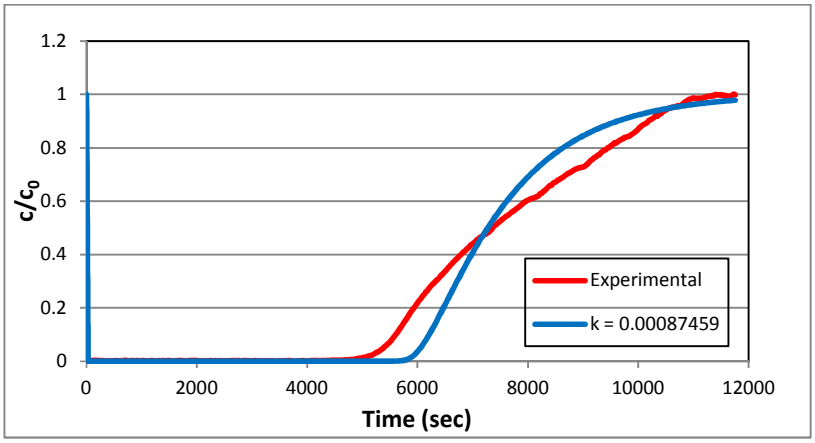

Figure 45. 1D breakthrough curve at 5 l min^{-1} (k_e = 0.00087459)

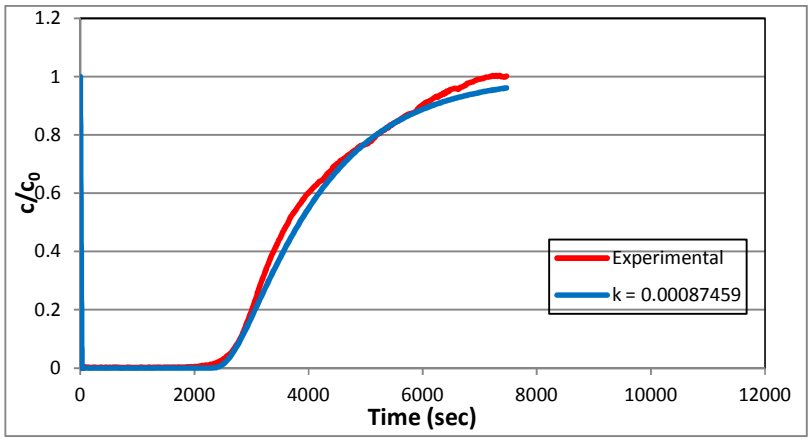

Figure 46. 1D breakthrough curve at 9 l min^{-1} (k_e = 0.00087459)

Now gPROMS is used to estimate k_e for 5 and 9 l min^{-1}. Table 9 shows the values of mass transfer coefficients obtained from gPROMS for the different flow rate conditions. The table also lists the parameters involved in establishing the goodness of fit test. The comparisons with experimental data are shown in Figures 47 and 48 for two flow rates 5 l min^{-1} and 9 l min^{-1}, respectively.

Table 9. Parameter estimation using gPROMS for different operating conditions

R^2	Q = 5 l min^{-1}	Q = 7 l min^{-1}	Q = 9 l min^{-1}
k_e	0.00061552	0.00087459	0.0008597
Weighted Residual	407.96	247.04	239.87
χ^2 **–value (95%)**	438.11	306.11	285.73
Comment	Good fit: weighted residual less than χ^2	Good fit: weighted residual less than χ^2	Good fit: weighted residual less than χ^2

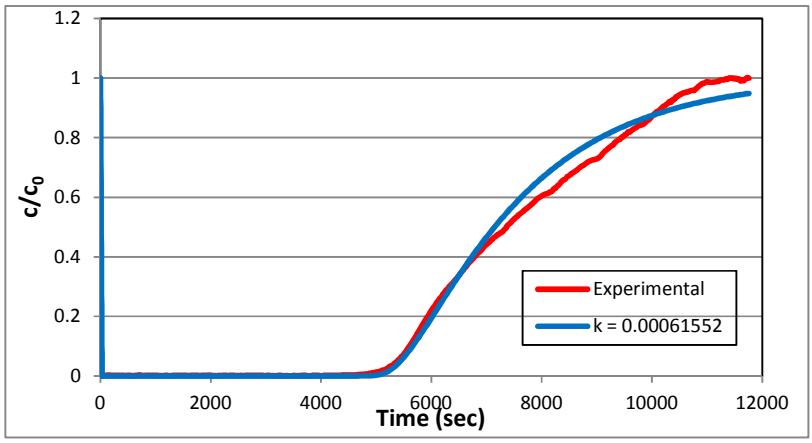

Figure 47. 1D breakthrough curve at 5 l min^{-1} (k_e = 0.00061552)

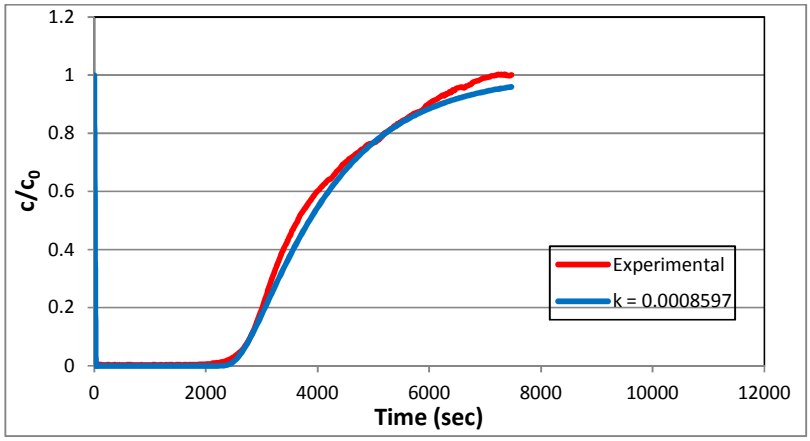

Figure 48. 1D breakthrough curve at 9 l min^{-1} (k_e = 0.0008597)

It has been seen that the best values of k_e, as obtained from gPROMS, depend on gas flow rate down the monolith channel. The dependency is small at the higher flow rate of 9 l min^{-1} and more pronounced at the lowest flow rated of 5 l min^{-1}. In principle, though, an internal mass transfer coefficient cannot be a function of the flow rate down the gas channel. Therefore, it is now necessary to study the impact of mass transfer external to the adsorbent.

6.1.1.7. Internal vs. external mass transfer coefficient (k_e vs. k_c)

The effect of mass transfer coefficient on the breakthrough curve has been investigated in the literature. Crittenden, *et al.* (2011) used the expression of Patton, *et al.* (2004) derived from the LDF approximation to determine the internal mass transfer coefficient of a monolith square channel geometry transformed into equivalent circular ducts. Yu, *et al.* (2007) calculated the internal mass transfer coefficient for a slab geometry according to the method of Glueckauf (1955) for a spherical adsorbent. Bonjour, *el al.* (2005) and Clausse, *et al.* (2004) used sensitivity analysis to find the suitable mass transfer parameter. Grande, *et al.* (2006) and Valdes-Solis, *et al.* (2004) both used the Sherwood expression for the calculation of external mass transfer coefficient.

Vis-à-vis the findings presented in the previous section, an insight into mass transfer parameters is necessary. The mechanism of adsorption is often described by two steps: mass transfer from the bulk to the monolithic surface and mass transfer within the internal structure of the monolith. The influence of external mass transfer is noticeable particularly at low fluid flow rates due to diffusion of the pollutant from bulk gas to the monolithic surface. While on the other hand, the internal mass transfer resistance results from the diffusion of organic molecules within the porous monolith. In addition to the external mass transfer, the internal mass transfer may play a dominant role.

In the literature, two-resistances (internal and external) are modelled for the diffusion and reaction in catalytic monoliths. With the linear driving force (LDF) approximation, internal and external mass transfer effects can be contained in a single overall coefficient (k) in equation (eq. 72). The external and internal mass transfer

resistances are coupled in series for a spherical crystalline adsorbent as given by Ruthven's expression (Ruthven, 1984). This relationship provides an extension of the Glueckauf approximation for systems in which more than one mass transfer resistance is significant.

$$\frac{1}{kK} = \frac{R_p}{3k_f} + \frac{R_p^2}{15\varepsilon_p D_p} + \frac{r_c^2}{15KD_c} \qquad \text{(eq. 72)}$$

where

k	=	mass transfer coefficient, s^{-1}
K	=	Henry's law adsorption constant, dimenssionless
R_p	=	adsorbent pellet radius, m
k_f	=	external fluid film mass transfer coefficient, s^{-1}
ε_p	=	porosity of adsorbent particle
D_p	=	pore diffusivity, $m^2\ s^{-1}$
r_c	=	crystal or microparticle radius, m
D_c	=	intracrystalline diffusivity, $m^2\ s^{-1}$

An equivalent expression now needs to be developed for the monolith. First of all, carbon is not crystalline and hence the third resistance in Ruthven's equation is zero. Next, the geometric factor for external mass transfer in Ruthven's expression ($\frac{R_p}{3k_f}$) needs to be adapted for the monolith and this becomes ($\frac{1}{a_s k_c}$). Then the term accounting for the internal diffusivity ($\frac{R_p^2}{15\varepsilon_p D_p}$) is taken into account in the internal mass transfer coefficient (k_e). The value of k_e presented in Table 10 was estimated to be 0.0008 s^{-1}.

$$\frac{1}{k\ K} = \frac{1}{a_s k_c} + \frac{1}{k_e} \qquad \text{(eq. 73)}$$

Based on the equation parameters presented in Chapter 5, the external mass transfer coefficient was calculated using Hawthorn correlation. The calculated value of

k_c corresponds very well to the one calculated earlier (0.04958 m s^{-1}) by Sánchez-Liarte (2009).

Table 10. Values of internal & external mass transfer coefficients

Method	**Mass transfer coefficient**
Internal – parameter estimation	k_e = 0.0008 s^{-1}
External – Hawthorn (1974)	k_c = 0.045 m s^{-1}

It can be seen from Table 11 that the external mass transfer coefficient has no influence on the overall mass transfer coefficient.

Table 11. Parameters used in equation (eq. 73)

Parameter	**Value (s^{-1})**
k_e	0.0008
$a_s k_c$	205.71
kK	0.0008

In general, the external resistance to mass transfer is smaller than the internal pore diffusional resistance, but in some cases it may still be large enough to have some impact (Karger & Ruthven, 1992). Nonetheless, in the current study based on equation (eq. 73) and using the parameters shown in Table 11 the effect of the external resistance seems to be negligible in comparison to the internal one, and hence the overall mass transfer coefficient is essentially a function of the internal one only. Therefore, the value of k in equation (eq. 23) is 0.0008 s^{-1}. It is different from that obtained using equation (eq. 50) (0.00588 s^{-1}) of Glueckauf (1955) and from that obtained using equation (eq. 51) (0.00326 s^{-1}) of Patton, *et al*. (2004). These differences will be discussed later in Chapter 9.

6.1.1.8. Adsorption model outputs

The predicated adsorption experimental breakthrough curves for the bench scale monolith using k = 0.0008 s^{-1} and a flow rate of 7 l min^{-1} are shown together with the gas phase temperature at the end of the monolith in Figure 49. The modelled breakthrough curve matches the experimental one with a 0.974 coefficient of determination. It can be noted that that there is a slight deviation at the top and the bottom of the curve. Overall, however, the matching of the curves is satisfactory, and the curves are similar in shape to those from the literature illustrated in Figure 50.

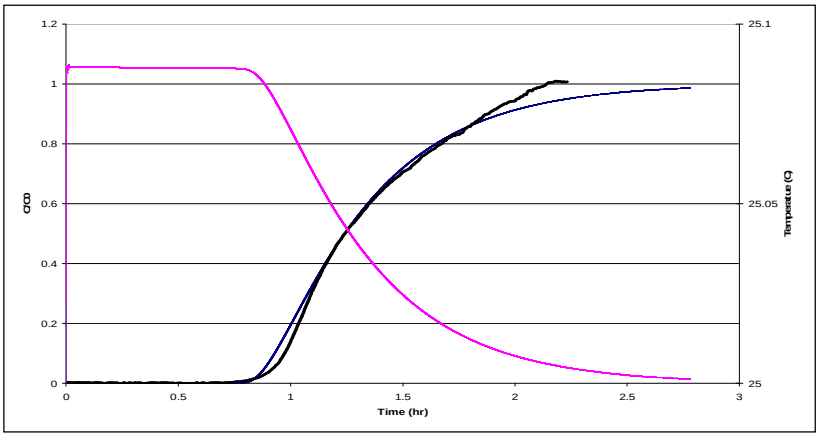

Figure 49. Adsorption breakthrough curve (mass & energy balance)

The temperature curve shows the exothermic nature of the adsorption process, as the temperature increases slightly at the same time as adsorption occurs. The temperature then decreases to 25ºC, the feed temperature, as expected when breakthrough is complete. This temperature curve is similar to that found by Yu, *et al*. (2007) in Figure 50.

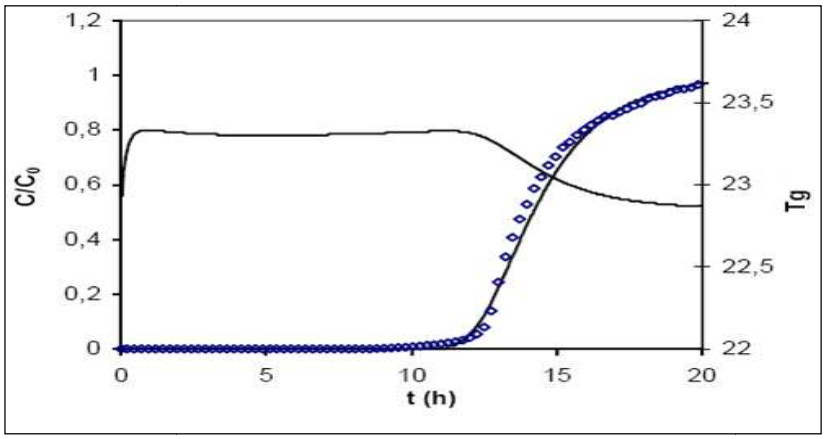

Figure 50. Adsorption breakthrough curve (Yu, *et al*., 2007)

The gas phase concentrations and hence the mass transfer zone (MTZ) can be deduced from the adsorption model by plotting the gas concentration over the length of the monolith at specific intervals of time, as illustrated in Figure 51 for k = 0.0008 s^{-1} and a flow rate of 7 l min^{-1}. This shows how the concentration profile moves through the length of the monolith over time. In accordance with the breakthrough curve illustrated in Figure 49, the monolith of 10.3 cm is fully saturated in less than an hour.

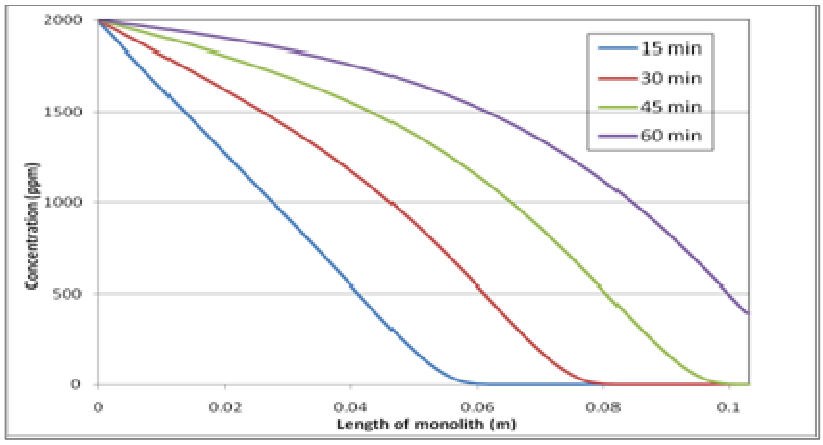

Figure 51. Mass transfer zone (MTZ)

The loading data (that is, the amount adsorbed on the monolith) can be deduced from the simulated breakthrough curve and can be compared to experimental data obtained at the University of Bath. The simulated average loading (q) is obtained from

the gPROMS model based on the LDF approximation. The loading can also be obtained from the gPROMS model by mean of a mass balance and integrating the breakthrough curve. Experimental data, on the other hand, can be obtained in two ways. Firstly (Method A), it can be determined from a mass balance by integrating of the breakthrough curve. Secondly (Method B), it can be determined by weighing the monolith before and after complete breakthrough. The four values are compared in Table 12. The values of the experimental data obtained at the University are slightly different. Method B gave close predictions based on experimental and modelled calculations of DCM loading. While the simulated data predicted the highest loading when compared to the other three values. Loading prediction affects the desorption process and consequently the cyclic process, as the predicted DCM loading is the starting point of the desorption process. In the desorption and cyclic processes, the simulated value of the average loading will be used, as it is directly calculated in the adsorption step.

Table 12. Loading data at 125 min using bench scale platform

Adsorbate	**Modelled (simulated)**	**Modelled (method A)**	**Experimental (method A)**	**Experimental (method B)**
Total Loading (g)	4.51	3.87	3.96	4.23

The value of quantity adsorbed calculated using Tóth equation (eq. 4) equals 3.62 mol kg^{-1}, using the parameters presented in Table 3 of Chapter 5. As expected, this value corresponds to 4.51 g of adsorbate calculated by the gPROMS model. This value can also be experimentally depicted from Tóth isotherms developed similarly to the ones shown in Figure 19 of Chapter 5 by Crittenden, *et al*. (2011) (Crittenden, *et al.*, 2011). For a partial pressure of 2 mbar, the loading is 5 mol kg^{-1}. This value corresponds to 5.6 g of adsorbate. Based on Table 12, the loading data from the simulated adsorption model is in good agreement with the experimental data. Therefore the simulated loading data will be used as the initial loading in the desorption process and consequently in the cyclic process.

6.1.1.9. Effect of gas flow rate on the bench scale apparatus

The effect of gas flow rate and thereby the molar flux on the breakthrough curve is studied in Figure 52. The experimental curves and the gPROMS simulations (with k = 0.0008 s^{-1}) are compared. Three different flow rates are considered in the study, and the operating conditions are listed in Table 13. As can be seen in the figure, increasing the gas flow rate decreases the breakthrough time and vice versa. It is also noted that the relationship is not linear between the increase in the gas flow rate with the decrease of the breakthrough time.

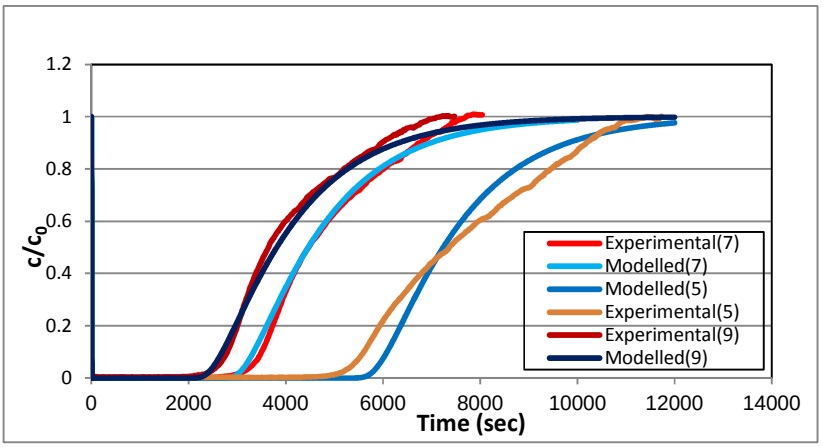

Figure 52. Effect of gas flow rate

Table 13. Operating conditions for adsorption runs

Q (l min^{-1})	**c_0 (ppmv)**
5	1950
7	2000
9	1910

As the flow rate increases, the time to breakthrough is decreased as expected and so is the total time for adsorption. As the velocity of the carrier gas increases, a greater amount of the VOC molecules transfer from the carrier gas and adhere to the carbon surface and the kinetics of adsorption increase causing the activated carbon to become fully loaded more quickly.

In addition as the flow rate increases, the breakthrough curves become slightly steeper while, as the flow rate decreases, the right-hand part of the curve spreads out needing more time to return to the initial concentration. This is because, as the contact time decreases, the time allowed for internal mass transfer will also decrease (Yu, 2003). In theory, low flow velocities can create a broader surface boundary layer producing a higher diffusion resistance in the boundary layer. In some situations, external transport could begin to take part and control the rate of the overall process. Conversely, at high carrier gas velocities, micropore diffusion can become the limiting rate factor and the pore structure becomes very important. The slowest process step controls the overall adsorption rate with the transition from equilibrium control at low flow rates to kinetic control at high flow rates (Brandani, *et al*., 2004).

Theoretically, at high flow rates, the speed of the MTZ increases as the breakthrough time is observed to shorten. As shown in Figures 53 and 54, the MTZ for the higher flow rate moves faster in the monolithic column. The figures show the data for 30 minutes and 45 minutes, respectively. The MTZ is expected to be shorter when the mass transfer increases. A shorter and faster MTZ will make the breakthrough curve become narrow and steeper (Schweitzer, 1997).

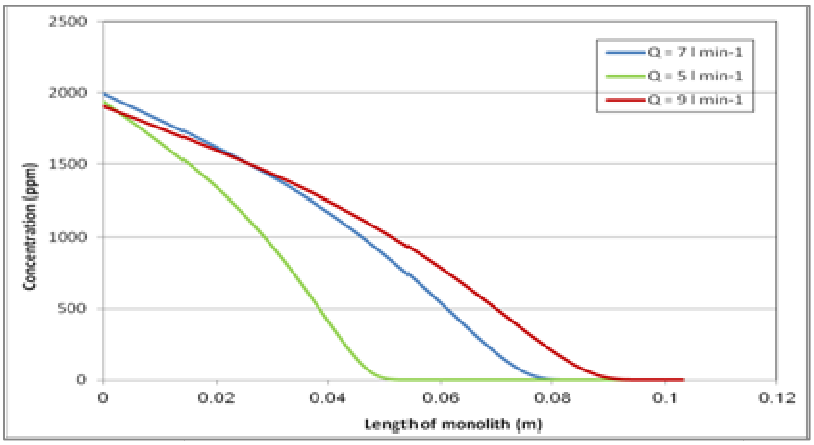

Figure 53. Effect of gas flow rate on MTZ at 30 min

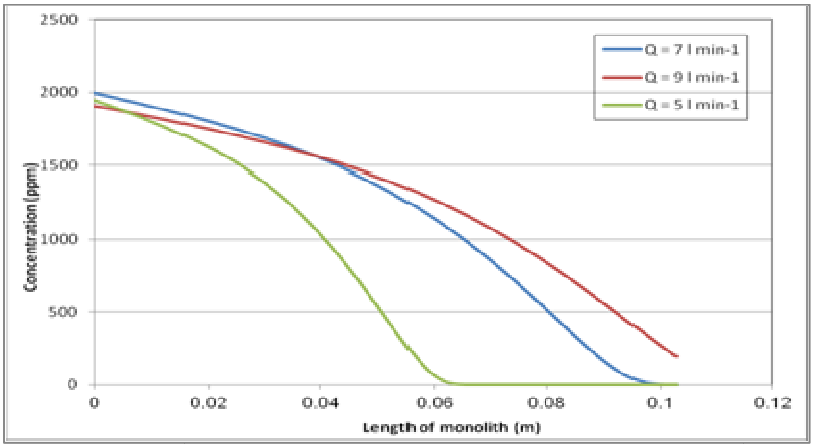

Figure 54. Effect of gas flow rate on MTZ at 45 min

6.1.2. Validation of adsorption on the pilot scale

The gPROMS model devised for the adsorption breakthrough curve is now validated for a longer monolith (58.5 cm). The model was initially validated in section 6.1.1 for a 10.3 cm monolith implemented on the bench scale. To further assure the robustness of the gPROMS model, it is now validated for a longer monolith implemented on the pilot plant rig.

The pilot plant rig is a scale up of the bench scale set up. Therefore, the operating conditions on the pilot plant are also scaled up in comparison with those used for the bench scale. The parameters used on the pilot plant are shown in Table 14.

The gPROMS modelled breakthrough curves for the longer monolith are shown in Figures 55, 56 and 57 to assess their agreement with the experimental breakthrough curve. Figures 55, 56 and 57 correspond to three values of mass transfer coefficients 0.0008 s^{-1}, 0.00087459 s^{-1} and 0.0010466 s^{-1}, respectively. The first value (0.0008 s^{-1}) is the bench scale validated value. The second value (0.00087459 s^{-1}) is the gPROMS parameter estimation value for bench scale. Finally, the third value (0.0010466 s^{-1}) is the gPROMS parameter estimation value for pilot scale.

Table 14. Values of Bath parameters used in mass balance for adsorption and desorption for 58.5 cm monolith

Description	Parameter	Value	Unit
Density of gas (adsorption)	ρ_q	43.15	mol m^{-3}
Density of gas (desorption)	ρ_q	25.7	mol m^{-3}
Axial diffusion coefficient (adsorption)	D_{ax}	0.00285	m^2 s^{-1}
Axial diffusion coefficient (desorption)	D_{ax}	$1.88x10^{-5}$	m^2 s^{-1}
Linear velocity (adsorption)	u_{ave}	3.7	m s^{-1}
Linear velocity (desorption)	u_{ave}	0.2	m s^{-1}
Specific Molar Flux (adsorption)	u_m	143.9	mol m^{-2} s^{-1}
Specific Molar Flux (desorption)	u_m	5.76	mol m^{-2} s^{-1}
Porosity of monolith	ε	0.44	
Density of solid	ρ_s	842.2	kg m^{-3}
Maximum amount adsorbed	q_m	5.91	mol kg^{-1}
Affinity parameter (adsorption)	b	0.0088	Pa^{-1}
Affinity parameter (desorption)	b	$8.3x10^{-5}$	Pa^{-1}
Tóth parameter	t	0.71166	
Mass transfer coefficient	k_e	0.0008	s^{-1}
Length of monolith	L	0.585	m
Diameter of monolith	D	0.0186	m
Side length of channel	d	0.000647	m
Thickness of channel wall	e	0.000395	m
Temperature (adsorption)	T	313.27	K
Pressure	P	101325	Pa
Affinity parameter	b_0	$2.615x10^{-6}$	m^3 mol^{-1}
Isosteric heat of adsorption	ΔH_{ads}	5108.33	J mol^{-1}
Molecular diffusion coefficient	D_{mol}	$1.04976x10^{-5}$	m^2 s^{-1}
Effective diffusion coefficient	D_{eff}	4.5E-11	m^2 s^{-1}
Flow rate	Q	7.2	l min^{-1}
Initial concentration	c_0	2940	ppmv
Axial thermal conductivity (adsorption)	K_{ax}	23	W m^{-1} K^{-1}
Axial thermal conductivity (desorption)	K_{ax}	18	W m^{-1} K^{-1}
Heat transfer coefficient (adsorption)	h_s	6.16	W m^{-2} K^{-1}
Heat transfer coefficient (desorption)	h_s	4.36	W m^{-2} K^{-1}
Heat capacity of nitrogen	c_{pn}	1040	J kg^{-1} K^{-1}
Heat capacity of solid	c_{ps}	1000	J kg^{-1} K^{-1}

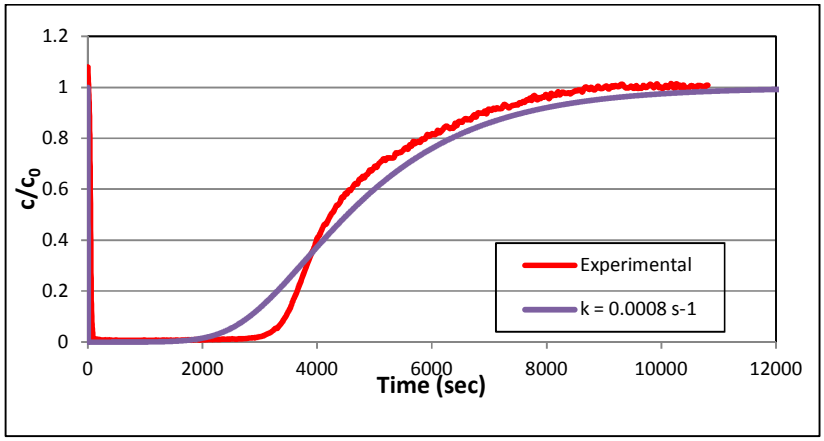

Figure 55. Experimental vs. modelled breakthrough curves for 58.5 cm monolith using k_e = 0.0008 s^{-1}

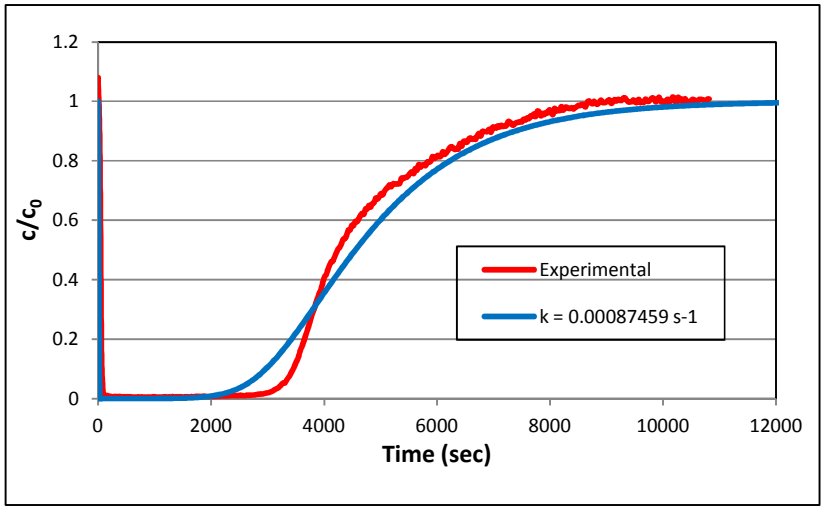

Figure 56. Experimental vs. modelled breakthrough curves for 58.5 cm monolith using k_e = 0.00087459 s^{-1}

None of these comparisons are perfect, but it seems that k_e = 0.0010466 s^{-1} is appropriate to use, with a coefficient of determination value of 0.9744. The gPROMS parameter estimation value for pilot scale (0.0010466 s^{-1}) is close enough to the bench scale validated value (0.0008 s^{-1}). As expected, MAST carbon makes their monoliths in a similar manner, but still the longer monoliths are not identical to the smaller monoliths.

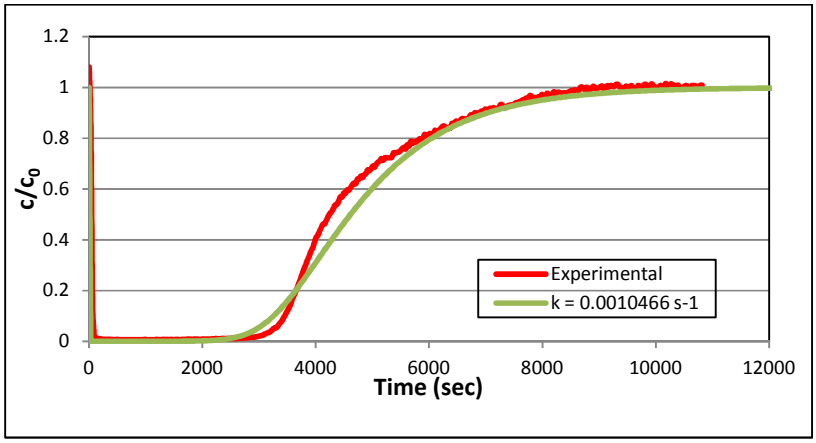

Figure 57. Experimental vs. modelled breakthrough curves for 58.5 cm monolith using k_e = 0.0010466 s^{-1}

6.1.3. Validation of adsorption for another VOC (toluene)

The developed gPROMS model is also validated for the experimental data of Yu *et al.*, (2007) using a different VOC, toluene. The parameters used in the gPROMS model are listed in Table 15. In this comparison, the mass transfer coefficient used in equation (eq. 23) is the one obtained by Yu, *et al*. (2007) and shown in Table 15.

Table 15. Yu, *et al*. (2007) parameters

Description	Value	Unit
Density of Toluene	41.03	mol m^{-3}
Axial diffusion coefficient	$2.65x10^{-4}$	m^2 s^{-1}
Porosity of monolith	0.64	
Density of solid	1040	kg m^{-3}
Affinity parameter	11.5	Pa^{-1}
Total Pressure	101325	Pa
Initial concentration	0.0013	mole
Tóth Parameter	0.206	
Mass transfer coefficient	$2.49x10^{-4}$	s^{-1}
Length of monolith	0.1	m

The developed model nicely predicted the breakthrough curve of Yu, *et al.* (2007), as can be seen in Figure 58.

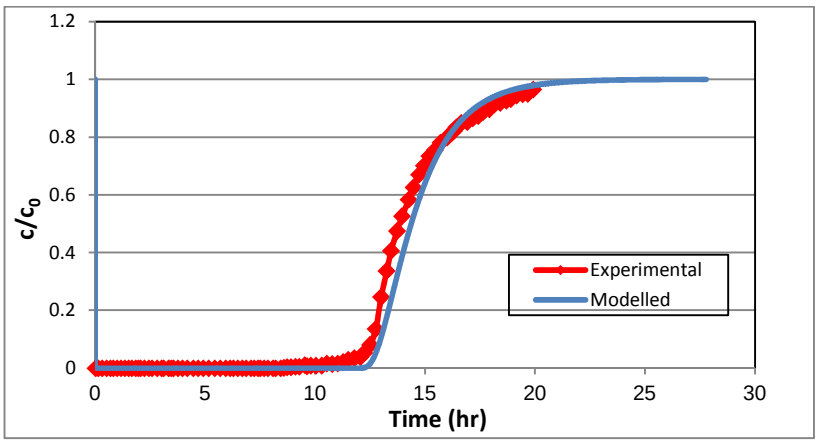

Figure 58. Experimental vs. modelled breakthrough curves for Yu, *et al*. (2007) data using toluene as VOC

The coefficient of determination for the curves shown in Figure 58 above equals 0.9856. Thus the gPROMS model gives a good prediction of the Yu, *et al*. (2007) experimental data.

6.2. Desorption process simulation

Desorption was not studied on the bench scale at the University of Bath. Experimental data which follow came from the pilot scale monolith. Table 3 shows the parameters for desorption provided experimentally and calculated for desorption modelling by the equations presented in Chapter 5.

6.2.1. Desorption on pilot scale

After complete breakthrough with VOC, the electrothermal desorption is started with the introduction of electrical current and the flow of purge nitrogen to push the desorbed VOC out of the monolith. The desorbate concentration reaches a maximum very quickly and attains a high concentration level more than the feed concentration of the adsorption step. Within minutes, most of the VOC is desorbed. Nonetheless, the

concentration continues to decrease slowly, and the remaining VOC will be obtained at rather low concentrations. Electrothermal desorption is very effective in the first minutes but the rate of desorption decreases rather quickly afterward. An experimental desorption curve is shown in Figure 59.

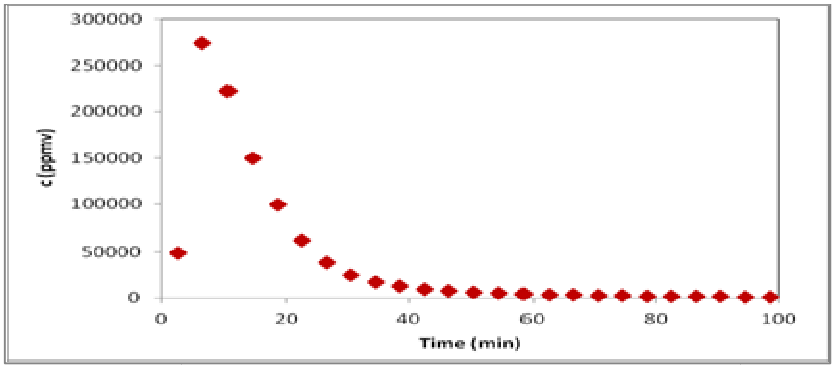

Figure 59. Experimental desorption curve at pilot scale platform

The desorption curve has the common shape of a peak followed by a tail, as illustrated in Figure 59. This shape of desorption curve is distinctive of the ESA process, and the tail is a dispersive wave (Yu, *et al.*, 2007). At the start of desorption, the VOC is highly concentrated, but subsequently the concentration gradually decreases. The performance of the process is highly dependent on the operating conditions.

Electrothermal desorption starts from the loading of 3.40 mol kg^{-1} attained in the adsorption step. Due to heating, the loading starts to decrease (0.98 mol kg^{-1}) then decreases much further (1.48 mol kg^{-1}) once desorption temperature is attained. The experimental loading data calculated by integrating the area under the breakthrough curve (method A) are presented in Table 16 for the pilot scale platform at the University. As can be seen in the Table, experimental desorption recovered 72% of the DCM adsorbed in the adsorption step (2.44 mol kg^{-1} from heating & desorption vs. 3.40 mol kg^{-1} from adsorption).

Table 16. Experimental loading data at pilot scale platform

Method A	**Adsorption**	**Heating only**	**Desorption only**	**Heating & Desorption**	**Recovery**
Loading (mol kg^{-1})	3.40	0.98	1.46	2.44	72%

6.2.2. Validation of desorption on pilot scale

The desorption curve is modelled using the modelling equations provided in Chapter 5. This curve is then validated with experimental data conducted at the pilot scale level, as can be seen in Figure 60. The value of mass transfer coefficient *k* at the higher temperature of 200ºC is 0.0021 s^{-1}. The value has been obtained by parameter estimation. An initial loading of 1.46 mole kg^{-1} which corresponds to the value presented in the previous table is used in modelling.

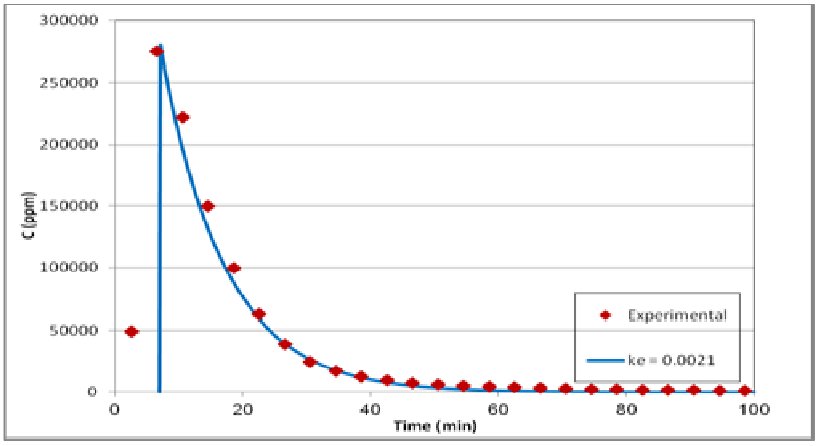

Figure 60. Desorption breakthrough curve for pilot plant

The deviation between the modelled and experimental curves was quantified using the coefficient of determination R^2. The resulting coefficient of determination amounts to 0.9928, confirming the good agreement between the modelled and experimental curves.

The value of the mass transfer coefficient (*k*) was estimated to be 0.0021 s^{-1} for desorption at the pilot-scale. This value is 2.625 times larger than that estimated in section 6.1.1 for adsorption at the bench scale (0.0008 s^{-1}) and 2.006 times larger than that estimated in section 6.1.2 for adsorption at the pilot scale (0.0010466 s^{-1}). It is normal that this value would be greater because the temperature is much higher for desorption. The coefficient *k* is represented by the diffusivity in the solid which increases with temperature regardless of the mechanism of diffusion. Yu, *et al*. (2007) found that *k*

of desorption (0.0034 s^{-1}) was 14 time higher than that for adsorption (0.000249 s^{-1}), thereby supporting the finding in the current study.

The adsorption process in this study is conducted at 298K while desorption takes place at 473K. Therefore, the desorption temperature is 1.587 times higher than the adsorption temperature. The ratio of the desorption mass transfer coefficient to the adsorption mass transfer coefficient can be correlated to the ratio of their corresponding temperatures. This temperature ratio can then be mapped to the diffusion coefficient equations presented in Chapter 5 in order to see which diffusion mechanism has the greater impact on the adsorption/desorption process.

The Knudsen diffusion coefficient can be calculated using equation (eq. 48). This equation relates Knudsen diffusivity to the square root of temperature. The square root of the ratio of desorption to adsorption temperatures gives a value of 1.26 which equals the ratio of desorption to adsorption Knudsen diffusivities. This value is lower than the ratio of desorption to adsorption mass transfer coefficients indicating that Knudsen diffusion is not the mechanism that is mainly dominating the diffusivity in the solid.

The molecular diffusion coefficient can be calculated using the Chapman-Enskog equation (eq. 44) presented in Chapter 5. This equation shows that molecular diffusion is a function of temperature to the power of 1.5. The ratio of desorption to adsorption temperatures powered to 1.5 gives a value of 2.0 which corresponds to the ratio of desorption to adsorption mass transfer coefficients estimated for the pilot scale. This agreement indicates that the dominating diffusion is molecular, as calculated using the Chapman-Enskiog equation.

Molecular diffusion can also be calculated using the FSG equation (eq. 46). This equation relates the molecular diffusion to temperature powered to 1.75. The ratio of desorption to adsorption molecular diffusion amounts to 2.24 based on the temperature ratio. This value is higher than the ratio of desorption to adsorption mass transfer coefficients indicating perhaps the unsuitability of the FSG equation in comparison to the Chapman-Enskiog equation.

It was shown earlier in section 6.1.1.7 that the dominating mass transfer coefficient is the internal one which encompasses both molecular and Knudsen diffusion. Based on the analysis just presented, molecular diffusion seems to be dominating

indicating that the dimension of the gas molecules is much smaller than the pore diameter. Gaseous collisions are also more frequent than collisions of the DCM molecules with the pore walls, and ordinary bulk diffusion occurs.

Another diffusion mechanism that potentially affects the kinetics of adsorption and desorption is surface diffusion, as discussed earlier in section 4.2.2.3. Surface diffusion, however, can be neglected in this analysis since, as described by Ruthven: "surface diffusion is significant only in small diameter pores in which the flux through the gas phase can generally be attributed entirely to Knudsen diffusion". This is not the case here as the flux has been attributed, as above, to molecular diffusion. In addition, Ruthven indicated that the contribution of surface diffusion decreases with increasing temperature. This is because the amount adsorbed on a surface decreases significantly with increasing temperature. Therefore, surface diffusion is expected to be less effective for desorption in comparison with adsorption. The resulting ratio of desorption to adsorption surface diffusion then amounts to less than unity, which is again not the case here.

6.2.3. Experimental vs. simulated desorption

In the desorption curve, two regions are identified. The first region of desorption is mainly controlled by the temperature increase of the monolith whereas in the second region the concentration decreases slowly and is a function of the mass transfer coefficient.

The experimental data show a sharp increase of concentration over the heating time whereas the modelled curve does not take into account this heating time. The purge gas flow rate has no influence on the maximum concentration, which is mostly attributed to the desorption temperature. Tailing increases at reduced flow rate by dilution phenomenon (Yu, *et al.*, 2007).

Table 17. Simulated loading data at pilot scale platform

Method A	**Adsorption**	**Heating only**	**Desorption only**	**Heating & Desorption**
Loading (mol kg^{-1})	3.327	0.98	1.46	2.44

It is observed that VOC adsorbed onto the monolith is not fully desorbed, as demonstrated in Table 17. Adsorption resulted in 3.327 mole kg^{-1} of loading whereas heating and desorption evacuated only 2.44 mole kg^{-1} of VOC. A difference of 0.96 mole kg^{-1} is left adsorbed onto the monolith. Therefore, in cyclic modelling it is assumed that the resulting loading of adsorption is fed to the desorption process. Then the next cycle starting with adsorption is performed with the loading output of the previous cycle.

6.2.4. Validation for another VOC (Toluene)

The developed model is also validated for experimental data from for Yu, *et al.* (2007) using a different VOC, toluene in this case. The parameters used in the model are listed in Table 18.

Table 18. Yu, *et al.* (2007) parameters

Density of Purge Gas (N_2) (mole m^{-3})	25.7
Axial diffusion coefficient (m^2 s^{-1})	2.65×10^{-4}
Porosity of monolith	0.64
Density of solid (kg m^{-3})	1040
Affinity parameter (Pa^{-1})	0.003
Total pressure (Pa)	101325
Initial concentration (mole)	0.0013
Tóth parameter (t)	0.206
Mass transfer coefficient (s^{-1})	3.4×10^{-3}
Length of monolith (m)	0.1
Specific molar flux (mol m^{-2} s^{-1})	0.58
q_0 (mol kg^{-1})	1.59

The developed model nicely predicts the breakthrough curve of Yu, *et al.* (2007), as can be seen in Figure 61. The coefficient of determination for the curves shown in Figure 61 equals 0.9856. Thus the modelled gives a good prediction of Yu, *et al*. (2007) experimental data.

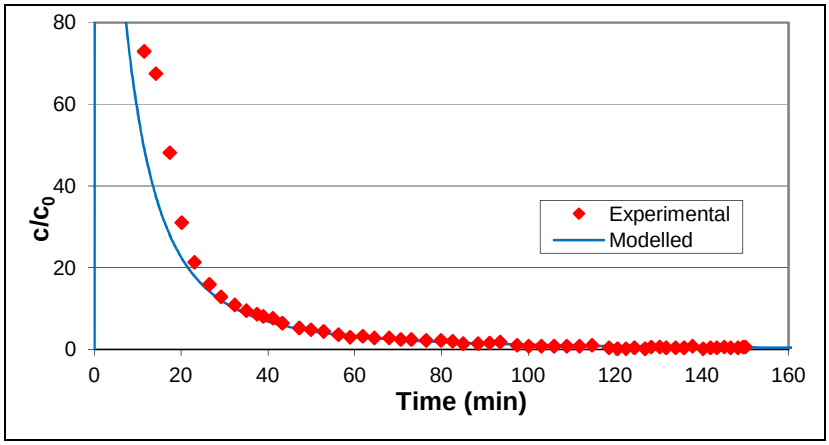

Figure 61. Modelled vs. experimental breakthrough curve for toluene using Yu, *et al.* (2007) data

6.3. Cyclic process simulation

For the cyclic process, the adsorption and desorption processes are simulated consecutively in gPROMS using Tasks, as described in a previous Chapter. Both adsorption and desorption processes have been validated in previous sections with experimental data. Therefore, the simulated cyclic process is based on validated models with k = 0.0008 s^{-1} for adsorption and k = 0.0021 s^{-1} for desorption. For the sake of this work, it can be assumed that cyclic process is made of adsorption and desorption solely and heating and cooling are incorporated in the adsorption and desorption process.

The cyclic process as simulated by gPROMS for the bench scale is illustrated in Figure 62. This figure shows the situation after the adsorption breakthrough curve has been fully completed followed by desorption breakthrough curve. From Figure 62, it is noted that desorption time is in the range of minutes whereas that of adsorption is the range of hours, meaning that the adsorption and desorption processes are not symmetrical. Grande and Rodrigues (2008) also noted that both adsorption and

desorption curves of CO_2 on activated carbon monolith are not symmetrical. Petkovska, *et al*. (2007) also concluded that very long adsorption and short desorption times are observed for their system.

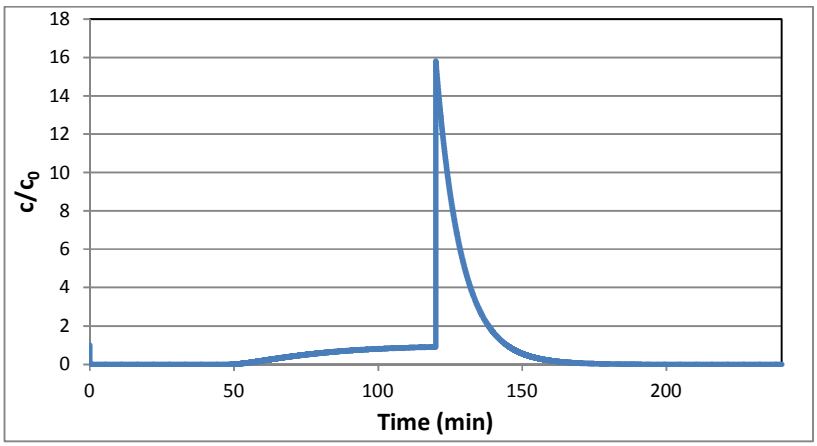

Figure 62. Cyclic process (4 hrs) - adsorption & desorption on the bench scale

Using the bench scale parameters, the maximum concentration in the gas outlet is around 16 times the initial concentration of the polluted gas. This concentration is reached in the first few minutes of desorption as shown in Figure 62. The maximum loading resulting from adsorption reached 3.3 mole kg^{-1}. This value dropped back to zero in desorption as illustrated in Figure 63 since total desorption was assumed.

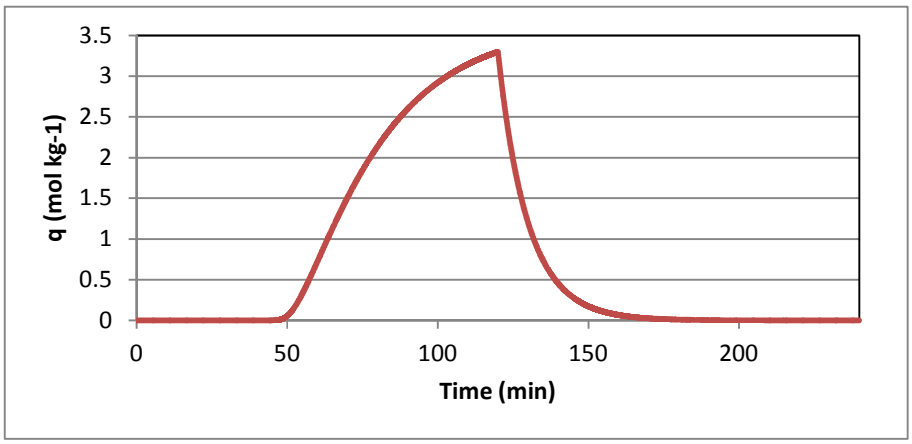

Figure 63. Cyclic process (4 hrs) - adsorption & desorption on the bench scale loading due to adsorption is 3.3 mole kg^{-1} fully recovered in desorption

6.3.1. Effect of cycle time

In the previous section, complete breakthrough was allowed to occur for adsorption and complete desorption was allowed to occur. In a real process, neither of these can occur and, accordingly, a cycle time is set to prevent breakthrough from occurring. In cyclic process modelling, therefore, a practical cycle time is introduced to control the duration time of adsorption and desorption. Adsorption breakthrough starts with the appearance of VOC concentration in the outlet stream. This breakthrough starts to occur at 45 minutes. A 30 minutes adsorption time followed by 30 minutes of desorption is therefore modelled in Figure 64. As can be seen in the Figure, adsorption was not completed within the 30 minutes duration tested as it requires around 45 minutes to breakthrough, and desorption was carried on regardless. Again desorption was not fully completed.

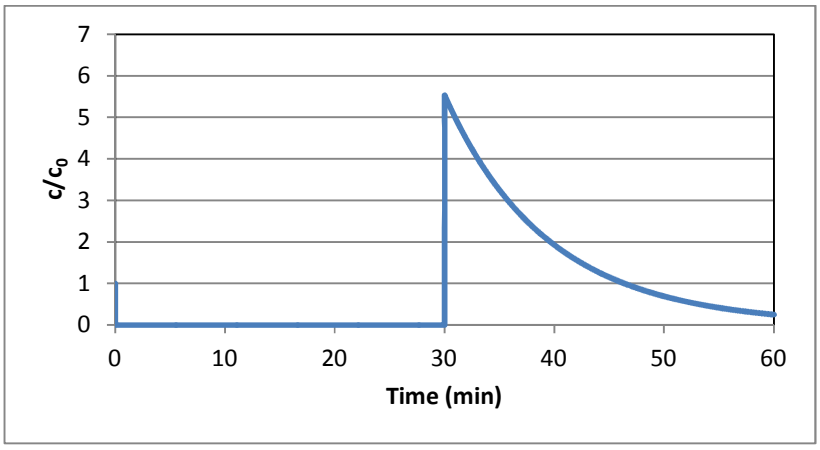

Figure 64. Cyclic process (1 hr) at bench scale – gas phase

The maximum concentration in the gas outlet now did not reach 16 times the initial concentration of the polluted gas upon desorption as in Figure 62. The maximum now was about 5.5 times the initial concentration as shown in Figure 64. This decrease in peak concentration is due to the fact that adsorption did not reach breakthrough in the adsorption step. Desorption is conducted before the full saturation of the monolith takes place. The loading in the solid also decreased from the 3.3 mole kg^{-1} predicted in Figure 63 to around 0.124 mole kg^{-1} as shown in Figure 65. Upon desorption, this value

dropped to only 0.046 mole kg^{-1} as not full desorption was assumed resulting in a recovery of 63% only.

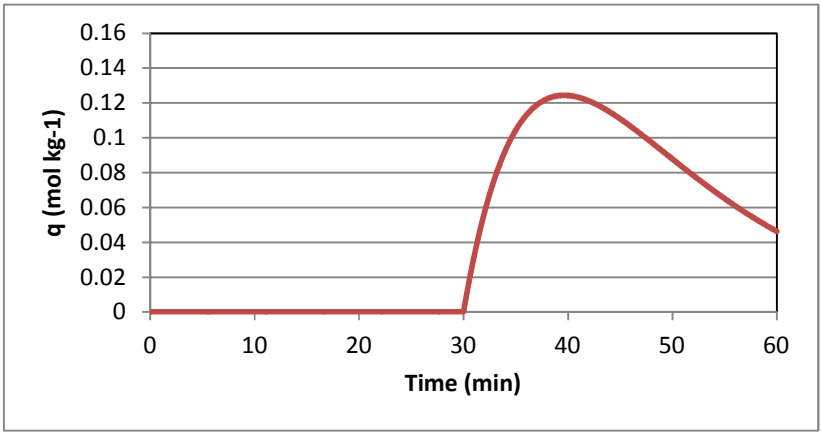

Figure 65. Cyclic process (1 hr) at bench scale - loading data

Successive cycles from start-up with a fresh adsorbent are illustrated in Figure 66. Cyclic process for a cycle time of one hour including 30 minutes of adsorption and 30 minutes for desorption required three consecutive cycles to reach steady state. In the first cycle 63% of adsorbed VOC is recovered while in the second and third cycles 66% of VOC adsorbed is recovered in each as shown in Table 19. Figure 67 shows the loading due to each cycle. Again, steady state required three consecutive cycles to be reached.

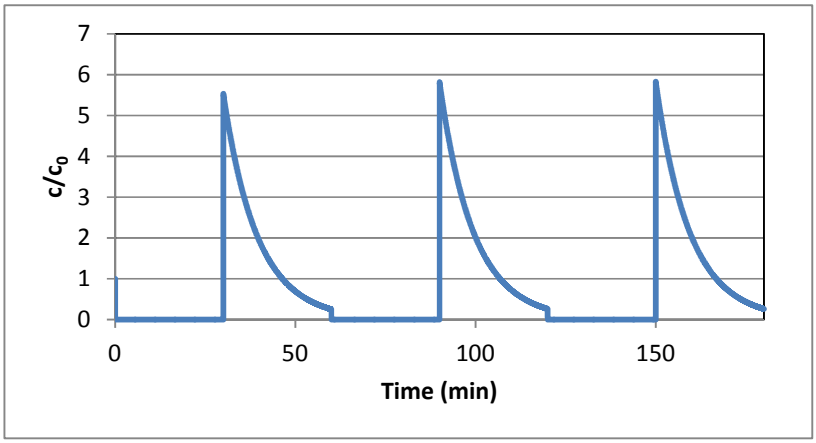

Figure 66. Cyclic process (1 hr & 3 cycles) – gas phase concentration

Table 19. Cyclic process (1 hr & 3 cycles) – loading & recovery

Loading (mole kg-1)	**Cycle 1**	**Cycle 2**	**Cycle 3**
Adsorption	0.12441	0.144	0.145
Desorption	0.04624	0.0485	0.049
Recovery	63%	66%	66%

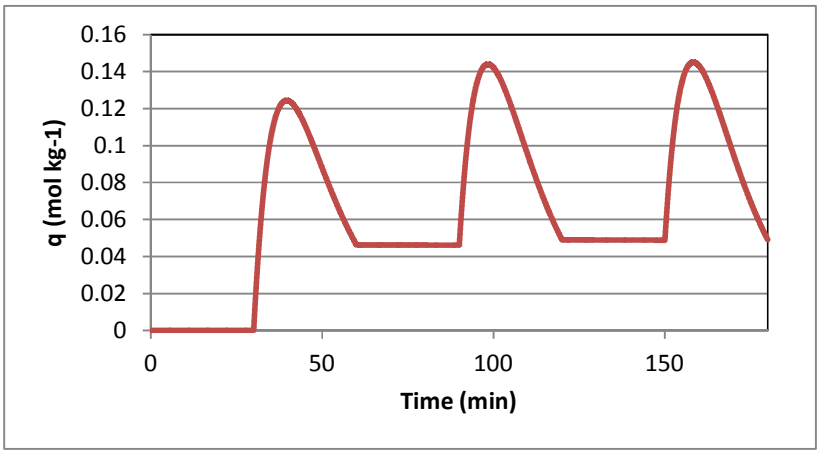

Figure 67. Cyclic process (1 hr & 3 cycles) – loading in solid phase

The effect of decreasing the cycle time on successive cycles is studied in Figures 68 and 69. The cycle time was reduced to 10 min of adsorption and another 10 for desorption. From the figures, it is clear that the adsorption and desorption are not fully completed within the 20 min cycle, and the cycles are not identical from start up. For these cycles to reach steady state, additional cycles were required as shown in Figures 70 and 71. In Figures 70 and 71, the number of cycles is extended to six cycles allowing steady state to be reached and the cycles to stabilize.

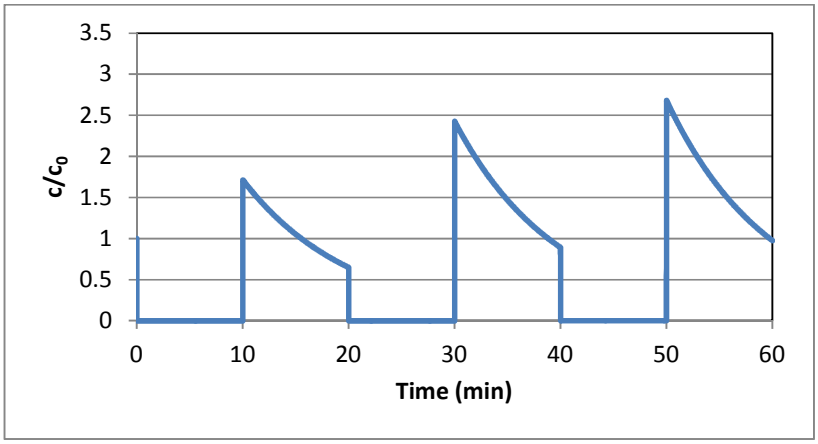

Figure 68. Cyclic process (20 min & 3 cycles) – gas phase concentration

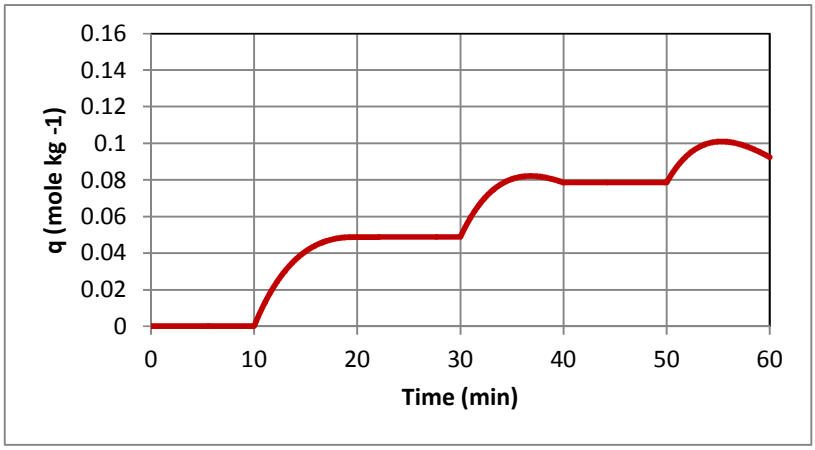

Figure 69. Cyclic process (20 min & 3 cycles) – loading in solid phase

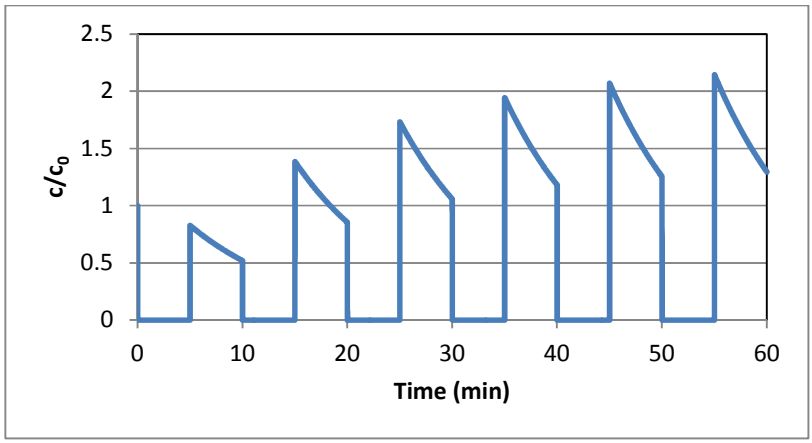

Figure 70. Cyclic process (20 min & 6 cycles)

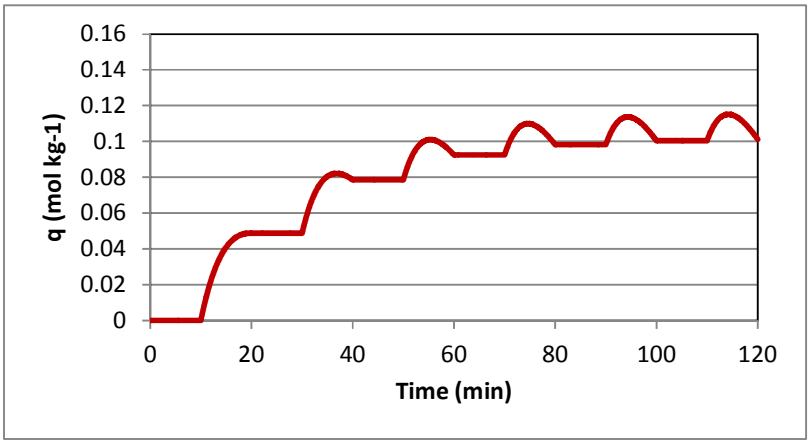

Figure 71. Cyclic process (20 min & 6 cycles)

In Figure 72, the cycle time was reduced further to 10 min in total allowing 5 min for adsorption followed by 5 min for desorption. As illustrated in the Figure, steady state operation is not reached within the 6 cycles but required more than 8 cycles to reach steady state as shown in Figures 74 and 75. The number of cycles was increased to 10 cycles in Figures 74 and 75.

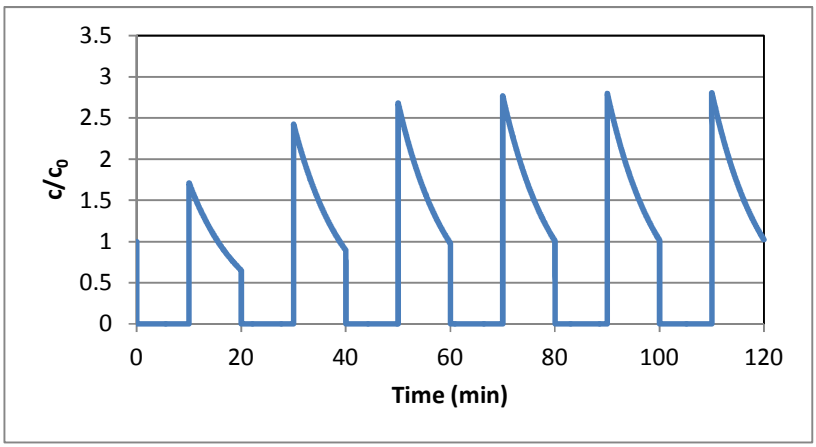

Figure 72. Cyclic process (10 min & 6 cycles)

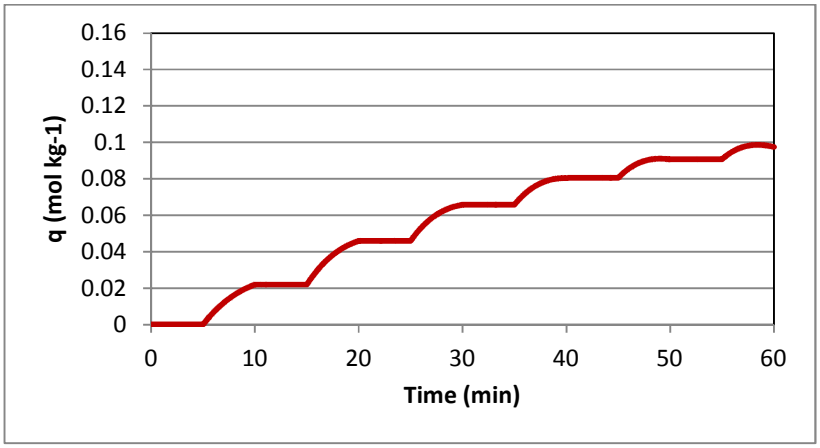

Figure 73. Cyclic process (10 min & 6 cycles)

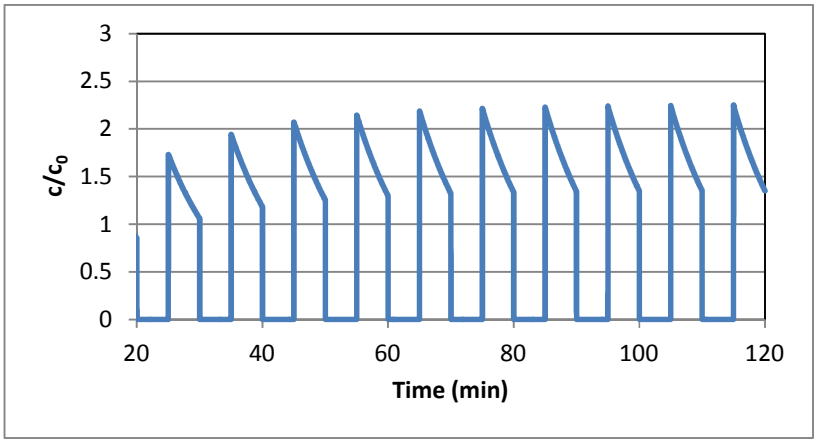

Figure 74. Cyclic process (10 min & 12 cycles)

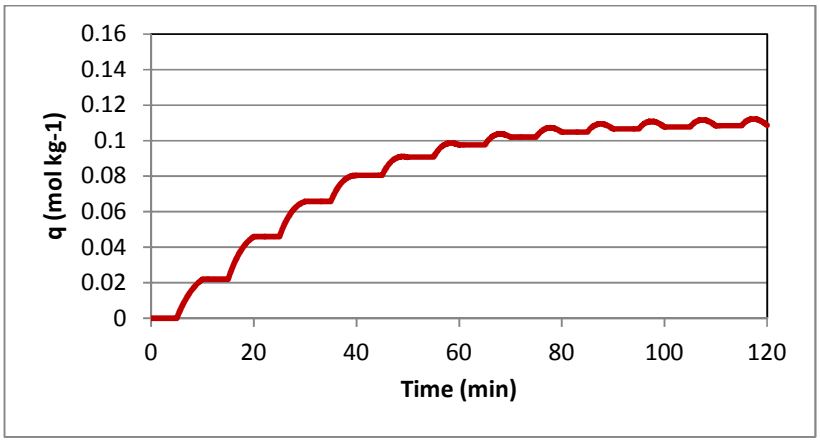

Figure 75. Cyclic process (10 min & 12 cycles)

6.3.2. Effect of initial concentration

The effect of altering the initial concentration on the cyclic breakthrough curve is also considered and studied in Figures 76 and 77 for 30 minutes of adsorption followed by 30 minutes of desorption. The effect of altering the initial concentration is not apparent on the maximum concentrations reached in Figure 76. However, increasing the initial concentration resulted in higher loading onto the solid monolith as shown in Figure 77.

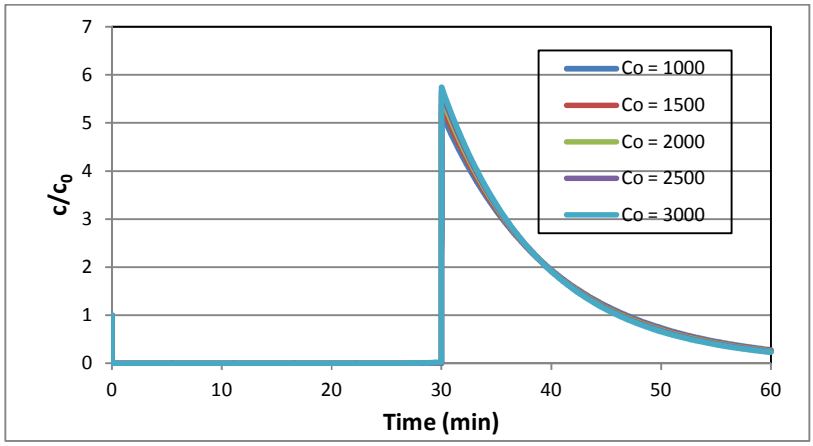

Figure 76. Effect of initial concentration on gas phase concentration

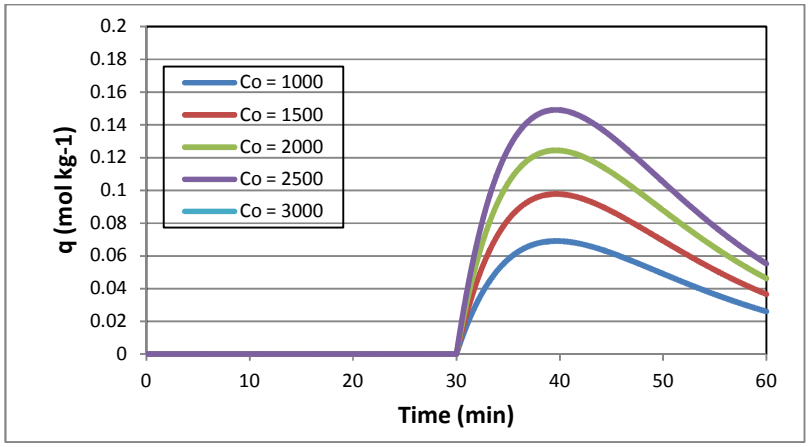

Figure 77. Effect of initial concentration on loading

6.3.3 Effect of regeneration temperature

The effect of regeneration temperature is tested on the cyclic breakthrough curve. Testing the regeneration temperature involves recalculating the parameters used in the desorption process especially as most of these parameters are temperature dependent. The base case is conducted at a desorption temperature of 200ºC as used up to now. The other regeneration temperatures studied are 150ºC and 250ºC.

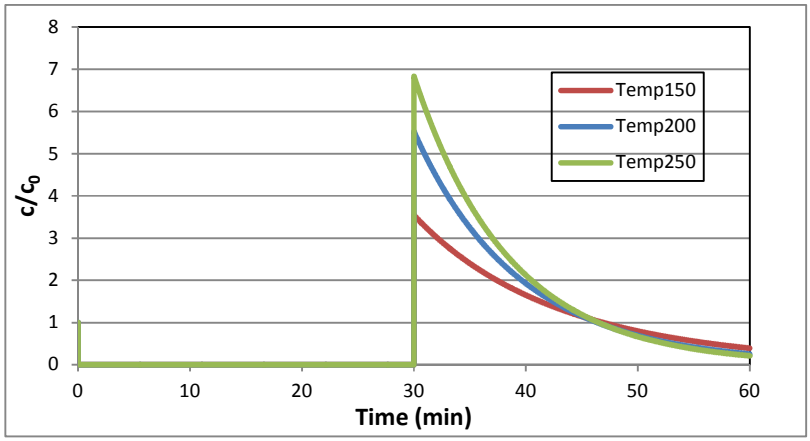

Figure 78. Cyclic process at varying desorption temperatures

As expected, increasing a regeneration temperature results in a faster desorption time and thereby a shorter overall cycle time. In addition, the maximum concentration reaches a higher value multiple of the initial concentration (c_0 = 2000 ppmv) for a higher desorption temperature. The maximum concentration reached 5.5 times the initial concentration (c_0 = 2000 ppmv) of the polluted gas upon desorption for the base case having a regeneration temperature of 200ºC and a maximum of 6.7 times the initial concentration (c_0 = 2000 ppmv) was reached when the regeneration temperature was increased to 250ºC as shown in Figure 78. Consequently the loading decreased with the increased regeneration temperature as can be seen in Figure 79. At higher regeneration temperature, higher recovery of VOC is expected.

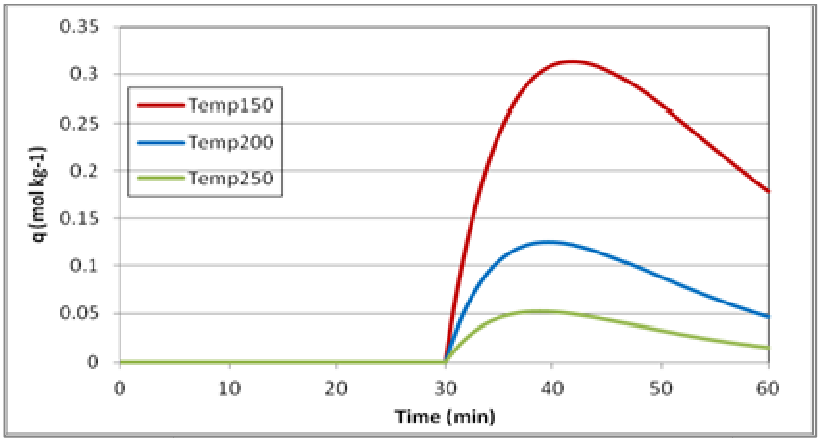

Figure 79. Cyclic process at varying desorption temperatures – loading in solid phase

6.3.4. Discussion of 1D cyclic process in the literature

The cyclic process is not fully investigated in the literature. Two studies have been conducted on cyclic process by Petkovska, *et al*. (2007) and Grande and Rodrigues (2008). The former study was conducted to recover hazardous VOC using activated carbon fibre cloth and was modelled using COMSOL & MATLAB while the latter removed CO_2 from flue gas by means of MAST activated carbon monolith and used gRPOMS in modelling.

Petkovska, *et al*. (2007) successfully used the mathematical model of their ESA process to investigate the influences of the key operational parameters on the cyclic process performance. The simulations were conducted for varying desorption temperatures breakthrough concentrations, supply voltages and gas flow rates for the duration of adsorption and desorption half cycles (Petkovska, *et al*., 2007).

The results demonstrate clear influence of the selected operational parameters on the performance of the ESA system. It can be deduced that the increase of the desorption temperature is favourable for the separation and purification of the feed stream, as well as regeneration of the adsorbed vapour, but undesirable for energy consumption. Alternatively, the increase in the breakthrough concentration is unfavourable for separation and purification of the feed stream, but good when regeneration of the adsorbed vapour and energy consumption are of principal importance. The increase of the supply voltage brings about superior energy efficiency. The total vapour recovery is

around 20%. It increases with the increase of the switch temperature, the decrease of the breakthrough concentration and with the increase of the supply voltage (Petkovska, *et al.*, 2007).

Grande and Rodrigues (2008) noted that their mathematical model described the experiments with good precision. The experimental data illustrated that both adsorption and desorption curves are not symmetrical, which cannot be precisely explained by the mathematical model used in their work. This behaviour is attributed to the channels with varying sizes in the boundaries of the honeycomb.

Grande and Rodrigues (2008) also observed that the cycle should be rearranged and enhanced. The primary necessary enhancement is to have the regeneration step of the cycle counter-current to the feed step. Another imperative feature that should be taken into account in the cycle is that VOC can be recovered in the electrification and desorption step, but this desorption step should be followed by a purge to let the system to cool down.

6.4. References

Bonjour, J., Clausse, M. & Meunier, F., 2005. A TSA process with indirect heating and cooling: parametric analysis and scaling-up to practical sizes. *Chemical Engineering and Processing*, 44, pp.969-977.

Brandani, F., Rousse, A., Brandani, S. & Ruthven, D.M., 2004. Adsorption Kinetics and Dynamic Behavior of a Carbon Monolith. *Adsorption*, 10(2), pp.99-109.

Brosillon, S., Manero, M. H. & Foussard, J, N., 2001. Mass transfer in VOC adsorption on zeolithe: experimental and theoretical breakthrough curves, *Environmental Science Technology*, 35(17), pp.3571-3575.

Clausse, M., Bonjour, J. & Meunier, F., 2004. Adsorption of gas mixture in TSA adsorbers under various heat removal conditions. *Chemical Engineering Science*, 59, pp.3657-3670.

Crittenden, B. D., Camus, O., Perera, S. P., Mays, T. J., Sánchez-Liarte, F., Tennison, S. R. & Crezee, E., 2011. Nonuniform channels in adsorbent monoliths. *AIChE Journal*, 57(5), pp.1163-1172.

Glueckauf, E. 1955. Part 10 – Theory of chromatography. Formula for diffusion into spheres and their application to chromatography. *Trans Faraday Soc*, 51, pp.1540-1551.

Grande, C. A, & Rodrigues, A. E., 2008. Electric swing adsorption for CO2 removal from flue gases. *International Journal of Greenhouse Gas Control*, 2(2), pp.194-202.

Grande, C. A., Cavenati, S., Barcia, P., Hammer, J., Fritz, H.G. & Rodrigues, A.E., 2006. Adsorption of propane and propylene in zeolite for a honeycomb monolith, *Chemical Engineering Science*, 61, pp.3053-3067.

Hawthorn, R. D. 1974. Afterburner catalysts-effects of heat and mass transfer between gas and catalyst surface. *AIChE Symp. Ser. Recent Advances in Air Pollution Control*, 137 (70), pp.428-438.

Karger, J. & Ruthven, D. M., 1992. *Diffusion in Zeolites and other microporous solids*. John Wiley, New York.

Patton, A., Crittenden, B. D. & Perera, S. P., 2004. Use of the linear driving force approximation to guide the design of monolithic adsorbents. *Chemical Engineering Research Des.*, 82, pp. 999-1009.

Petkovska, M., Antov-Bozalo, D., Markovic, A. & Sullivan, P., 2007. Multiphysics modeling of electric-swing adsorption system with in-vessel condensation. *Adsorption*, 13(3-4), pp.357 -372.

Ruthven, D. M., 1984. *Principles of adsorption & adsorption processes*. John Wiley & Sons, Inc.

Sánchez-Liarte, F., 2009. *Performance of electrically regenerable monolithic adsorbents for VOC control*. Ph.D. thesis: University of Bath.

Schweitzer, P. A., 1997. *Handbook of separation techniques of chemical engineering*. McGraw Hill.

Valdés-Solís, T., Linders, M., J. G., Kapteijn, F., Marban, G. & Fuertes, A. B., 2004. Adsorption and breakthrough performance of carbon-coated ceramic monoliths at low concentration of *n*-butane. *Chemical Engineering Science***,** 59(13), pp.2791-2800.

Yu, F. D., 2003. *Adsorption de composés organiques volatils sur un monolithe de charbon actif avec régénération thermique par effect Joule*. Ph.D. Thesis, Ecole Nationale Superieur des industrie chimiques, Laboratoire des Sciences du Génie Chimique, L'institut National Polytechnique de Lorraine, France.

Yu, F. D., Luo, L. A. & Grevillot, G., 2007. Electrothermal swing adsorption of toluene on an activated carbon monolith: Experiments and parametric theoretical study. *Chemical Engineering and Processing: Process intensification*, 46 (1), pp.70-81.

Chapter 7

Three dimensional modelling

One of the principal objectives of this study is to model the ESA process in a three-dimensional presentation. The reason behind this objective is to thoroughly study the effect of the different parameters on the adsorption/desorption process.

7.1. 3D Considerations

7.1.1. Geometrical presentation

3D models have been constructed lately in the literature because of the advancement in computer capabilities and in mathematical solutions to resolve intricate problems. The geometrical presentation for modelling in 3D is handled differently from one author to another, and several approaches are considered in the literature. The 3D geometrical presentation has a major impact on formulating the modelling equations and boundary conditions.

For a single monolithic channel, different domains can be addressed to represent the 3D model in the gas and solid phases. Camus, *et al*. (2007) considered two axes of symmetry to model the single channel as shown in Figure 80, thereby decreasing the channel to 1/4 of its size and reducing the computational time.

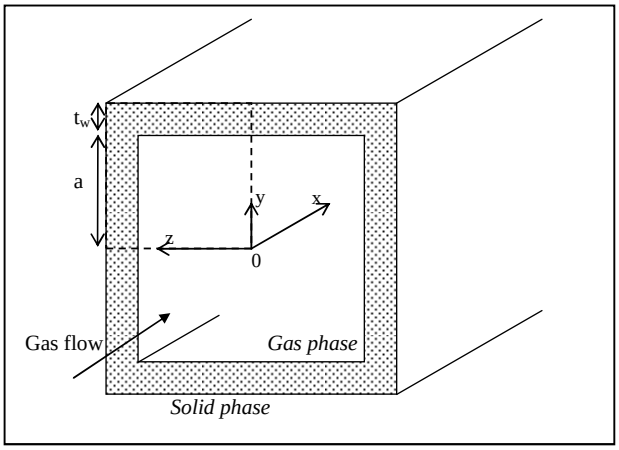

Figure 80. Three dimensional spaces in the solid and the monolithic channels (Camus, *et al*., 2007)

In a later study, Crittenden, *et al*. (2011) considered symmetry in three axes and reduced the channel to 1/8 of its size to lessen the computational time of the solution, as shown in Figure 81.

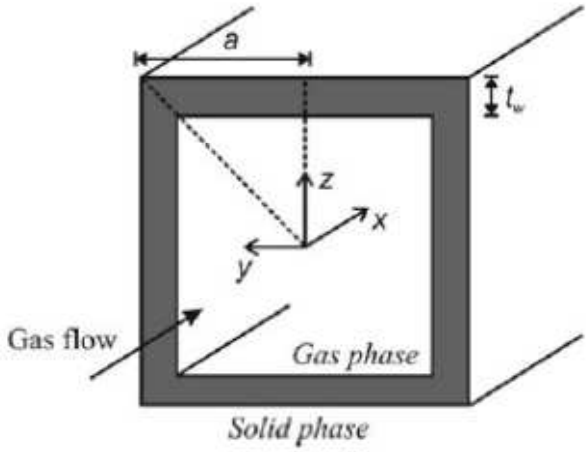

Figure 81. Three dimensional spaces in the solid and the monolithic channels (Crittenden, *et al*., 2011)

Grande, *et al*. (2006) presented two different configurations for their mathematical model: the first one retains the 3D picture of the configuration; while the other considers variation only in the axial direction. Figure 82 is a schematic diagram of both configurations.

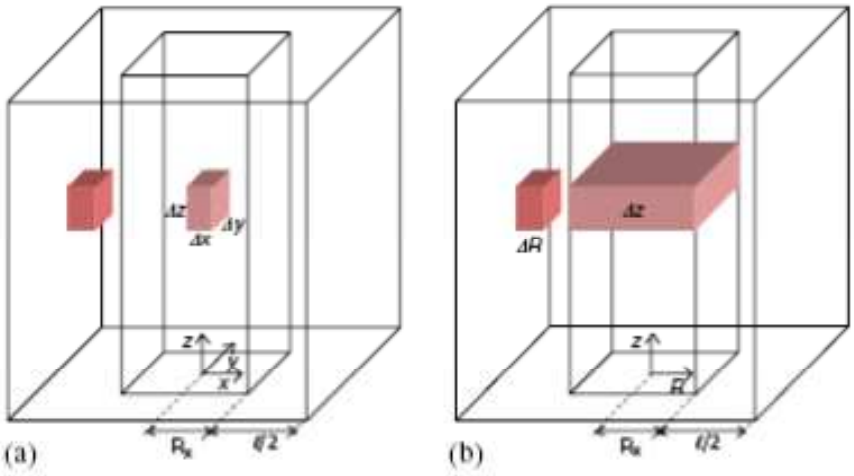

Figure 82. Breakthrough curves schematic modelling in one channel monolith: (a) 3D model; (b) 1D model (Grande, *et al.*, 2006)

Ahn and Brandani (2005a) improved the height equivalent theoretical plate (HETP) methodology by initiating a three-dimensional model and developing a straightforward HETP expression that considered the effect of the monolithic wall at the four corners. The authors also neglected diffusion in the axial direction within the solid and set the four corners (Figure 83) as an independent domain. In spite of these adjustments, the mathematical result required several hours of runtime to simulate.

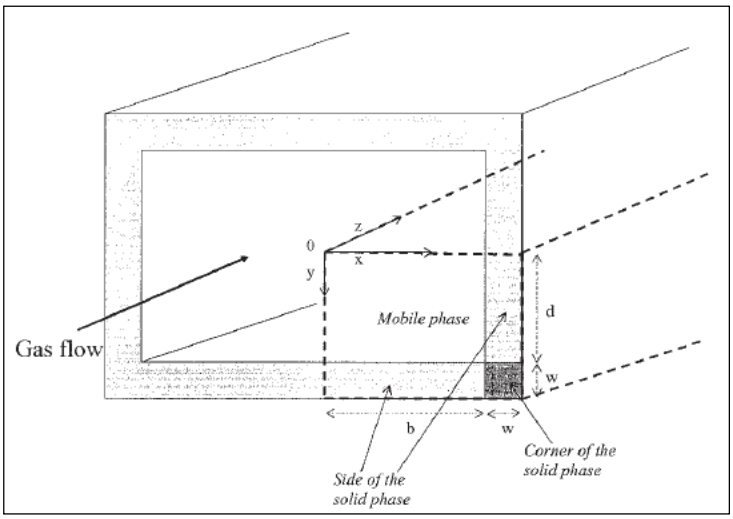

Figure 83. Rectangular channel (Ahn & Brandani, 2005a)

For the current study, the geometrical presentation of Grande, *et al*. (2006) was not adopted due to the fact that it involved overlapping domains causing the need to fill these domains with zeros. Also the geometrical presentation of Crittenden, *et al*. (2011) was not suitable since it necessitated writing out the boundary equations at the diagonal adding to the complexity of the problem.

The geometrical presentation presented by Ahn and Brandani (2005a) and Camus, *et al*. (2007) was adopted for the current study. One fourth of the monolithic square channel is modelled as illustrated in Figure 84. For this configuration, one gas domain and three solid domains are included. The gas domain is one quarter of the overall gas channel and is square in shape. The solid domains represent also one quarter of the overall solid domain. But this solid domain consists of one square corner and two rectangular borders equal in shape as illustrated in Figure 84.

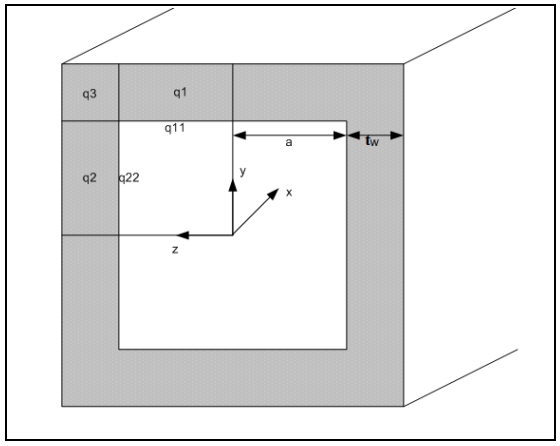

Figure 84. Three dimensional spaces in the solid and the monolithic channel

7.1.2. Discretisation method

The effect of the geometrical presentation is not only limited to formulating the 3D model but also largely affects the discretisation method used in approximating the solution of the differential equations, whether it is the finite difference method (FDM) or the finite element method (FEM). The discretisation process utilized by FEM and FDM differs. FDM is less robust for irregular shaped bodies than FEM. FDM involves approximating derivatives in a PDE and then solving the algebraic equations. In FEM,

the integral equation derived from the differential equation is solved by assuming a piecewise continuous function over the domain.

For the current study, FDM is used mainly as the discretisation method. The models of the software gPROMS are addressed by means of the "method of lines" numerical method. Discretisation of the distributed equations is performed with regard to all domains thereby reducing the solution to a combination of differential algebraic equations. In the main, the centred finite difference method (CFDM) is used. Grande, *et al*. (2006), on the other hand, used the orthogonal collocation on finite elements method (OCFEM) to solve most of their problem.

7.1.3. Uniform and non-uniform channel geometry

Monolithic channels differ in dimension and form as illustrated in Figure 85 of the monolith side view. At the edge of the monolith, the channels are uneven, non-square and smaller in cross sectional area than those at the inside. To simplify monolithic modelling, the performance of only a single channel is considered with the assumption that all the channels are equal in size and shape. Ahn and Brandani (2005b), nevertheless, assessed the non-uniformity of the channel to model the adsorption of CO_2 on square channel carbon monoliths and Crittenden, *et al*. (2011) considered non-uniform channel geometries in adsorbent monoliths to model the adsorption of VOC on a MAST ACM.

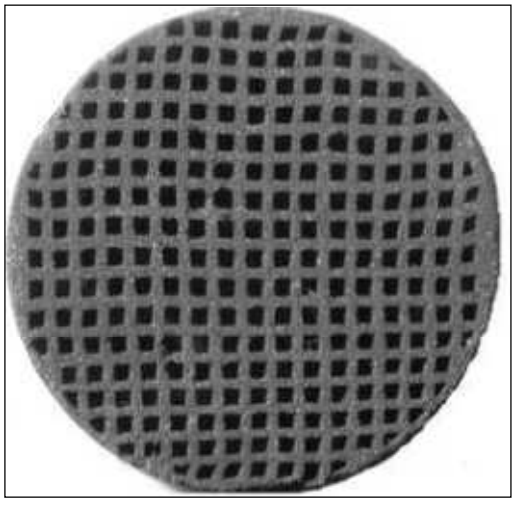

Figure 85. Cross sectional area of MAST activated carbon monolith used in bench scale column (Camus, *et al*., 2007)

Crittenden, *et al*. (2011) concluded that the non-uniformities in channel sizes resulted in broadening of the breakthrough curve. The channel size distribution used in the non-uniform channel model (NUCM) was broader than the one observed for uniform square channels. The NUCM produced a somewhat dissimilar end of the breakthrough curve than that obtained by a uniform channel model (UCM) and the experimental data. One cause could be the fact that the effective diffusion coefficient utilized in the NUCM is rather higher than that back-calculated by the UCM. Using the NUCM, the air flow is slower in the smaller channels. Hence breakthrough is not fully attained in these small channels justifying the vaguely dissimilar loadings forecasted by the models.

There is some uncertainty that deviations from channel to channel are probable in a monolithic adsorbent as the velocity distribution through different channels of a monolith at steady flow rate is explained by a normal distribution (Crittenden, *et al*., 2011). Therefore for the current study, only uniform channels are considered, and hence only one single channel is modelled.

7.1.4. Velocity profile

For the 1D model, the average channel velocity was used and derived from the volumetric flow rate over the monolith cross sectional area, as presented in an earlier Chapter. Three-dimensional modelling of the gas channel has previously demonstrated that there is a small variation in the breakthrough curves for the following three channel gas flow assumptions (Crittenden, *et al*., 2011):

- Developing flow
- Fully developed flow
- Plug flow

The equation for fully developed laminar flow in a rectangular duct was derived by Cornish (1928). This expression is then reduced due to symmetry to the following approximation, used in this study. The equation represents the parabolic velocity profile for a square channel (Crittenden, *et al*., 2011):

$$u(y,z) = \frac{9}{4} u_{ave} \left(1 - \frac{y^2}{a^2}\right)\left(1 - \frac{z^2}{a^2}\right) \qquad \text{(eq. 74)}$$

As reported by Crittenden, *et al*. (2011), the curves for developing flow and fully developed flow are coincident. The curve using the plug flow assumption, on the other hand, shows a longer time to breakthrough in comparison to the other two. Accordingly to simplify the development of the NUCM model, the fully developed parabolic flow assumption was utilized in the study of Crittenden, *et al*. (2011). This made the channel flow model fully three-dimensional with regard to the gas concentration.

Grande, *et al.* (2006) used diluted gas where the quantity of adsorbed gas is extremely small in comparison to the amount of inflowing gas into the column. Therefore, the gas density was assumed to be constant throughout the length of the channel. The momentum equation was then reduced to a constant velocity profile independent of the axial direction. The profile of velocity was totally developed over the entire channel and expressed analytically by Bird, *et al*. (2002)

$$u = \frac{\Delta P R_x^2}{4\mu_g L_c}\left[1-\left(\frac{y}{R_x}\right)^2\right]\left[1-\left(\frac{z}{R_x}\right)^2\right] \qquad \text{(eq. 75)}$$

where

ΔP = pressure difference between monolith inlet and outlet, Pa

μ_g = gas viscosity, kg s^{-1} m^{-1}

R_x = single channel half-length in x direction, m

$$\rho = \frac{MW}{RT_g}P \qquad \text{(eq. 76)}$$

MW = gas molecular weight, g mol^{-1}

R = ideal gas constant, m^3 Pa K mol^{-1}

T_g = gas temperature, K

Both Grande, *et al.* (2006) and Ahn and Brandani (2005a) considered a completely developed velocity profile function of *y* and *z* in the axial direction, and this

consideration will be adopted for the current study using the modified Cornish expression.

7.1.5. Diffusion vs. dispersion

By definition, dispersion is caused by the coupling of concentration difference and fluid flow whereas diffusion is caused by random movement of particles (Brownian motion) suspended in a fluid. Dispersion with an axial dispersion coefficient of (D_{ax}) is strongly a function of position and independent of chemistry. Diffusion (D_{mol}), on the other hand, is independent of direction and strongly dependent on chemical interaction. Dispersion also is much larger than diffusion. For the current study, D_{ax} is 24 times larger than D_{mol}, as axial dispersion (D_{ax}) amounts to 2.536 x 10^{-4} m^2 s^{-1} and molecular diffusion (D_{mol}) equals 1.04976 x 10^{-5} m^2 s^{-1}. Diffusion is normally the progression in which a component shifts through a concentration gradient, and dispersion denotes the mixing due to physical processes.

The amount of dispersion is lower in developing velocity profiles than in those which are fully developed. This arises because dispersion is enhanced by differences in the velocity of the fluid particles perpendicular to the main direction of flow. Diffusion details the net flux of molecules from a region of high concentration to one of low concentration. The result of diffusion is a gradual mixing of material.

The 1D mass balance model developed in Chapter 5 is axially dispersed through a single square channel where the flow regime in the channel is laminar. Therefore for this 1D configuration, the axial dispersion coefficient (D_{ax}) is considered, as plug flow with axial dispersion is assumed. The velocity profile is relatively flat for laminar flow. A dispersion coefficient is inversely proportional to a diffusion coefficient. The axial dispersion coefficient for laminar flow can be calculated by means of the Taylor relation from the molecular diffusion coefficient (D_{mol}).

Typically, D_{mol} is used in most studies for 3D modelling in the gas phase (Ahn & Brandani, 2005a; Grande, *et al*., 2006; Crittenden, *et al.*, 2011). Zabka, *et al*. (2006), however, used both D_{ax} in the axial direction and D_{mol} in the radial direction of the single monolith channel gas phase equation. For the current study, D_{mol} in the gas phase will be considered in the three directions of *x*, *y* and *z*.

7.1.6. LDF approximation

For the developed 1D model presented in Chapter 5, the LDF approximation was used to estimate the average amount of VOC adsorbed onto the surface of the activated carbon. This assumption can also be applied when developing the 3D model. Crittenden, *et al.* (2011) used the LDF approximation in their 3D model to estimate the average loading. Zabka, *et al*. (2006 & 2007) used a silica-based monolithic column and transformed the mass balance of the monolithic channel wall into an LDF equation by taking the average of the pore concentration throughout the monolithic wall and adopting the assumption of a parabolic pore concentration profile over the wall. Nikolajsen (2007) in his thesis stated that "to avoid the complexity of the diffusion solutions it is common practice to use the linear driving force (LDF) model with an overall effective rate constant. This approach eliminates the diffusion model for the adsorbent and assumes that the overall rate of uptake is LDF". By adopting this approach, the diffusion model for the adsorbed VOC can be eliminated and the overall rate of uptake can be estimated using the LDF expression.

The LDF approximation can also be used at the pore level. Kolade, *et al*. (2009) studied VOC abatement using an adsorptive reactor where the solid zone comprises the adsorbent and the catalyst. The mass balances were established in the gas phase and the solid phase where reaction and adsorption terms were incorporated. The reaction term accounted for the reaction taking place at the catalyst site while the adsorption term used the LDF expression to describe the intra-particle mass transfer. LDF is used to calculate the rate of adsorption at the particle level where a modified effective gas diffusion coefficient is devised.

Grande (2004) in his thesis studied the adsorption of VOCs (propane and propylene) on to a zeolite honeycomb monolith and used the LDF approximation in the gas phase continuity equation to account for the divergence among the bulk gas concentration and the gas concentration at the channel wall surface. Later on, Grande, *et al.* (2006) did not use the LDF approximation but only equated the mass fluxes at the interface of the gas and solid. Adsorption was accounted for in the mass balance equation of the monolith wall, the adsorption taking place in the zeolite crystals inserted into the ceramic monoliths. Ahn and Brandani (2005a) also did not use the LDF

approximation but only equated the mass fluxes at the fluid-solid interface and used a linear adsorption isotherm to account for equilibrium at the channel surface of the microfabricated monolithic column.

In order to consider the adsorption at the micro-scale, additional considerations/parameters are needed, such as an LDF expression for the intra-particle mass transfer and a modified effective diffusion coefficient for the rate of adsorption in a particle. In conclusion, the LDF approach at the gas/solid interface remains a valid approach and provides an overall approximation of the rate of adsorption in the solid phase. Therefore, for the current study, the LDF approximation will be used in modelling, especially since no adsorption data at the pore level inside the monolith is available. From the LDF approximation, the diffusion inside the pores of the solid is calculated using the diffusion coefficient knowing that the amount adsorbed equals the amount diffused within the solid.

7.2. ESA model development

7.2.1. Assumptions

A number of assumptions have been made in the development of the model. Some of these assumptions are listed as follows:

- Gas phase in assumed ideal and the ideal gas law is utilized.
- Gas is distributed uniformly in all the channels at the monolith entrance.
- Pressure drop is negligible.
- Purge gas (N_2) is not adsorbed.
- LDF approximation is valid.

7.2.2. Mass balance equations in gas phase configuration

The 1D model presented in an earlier Chapter was extended to 3D for the gas channel. By adopting the LDF approach, the mass balance in the solid domain is reduced

into the LDF equation at the interface of the gas and the solid phases. The overall 3D mass balance then amounts to the following equation:

$$\frac{\partial c(x,y,z)}{\partial t} - D_{mol}\left(\frac{\partial^2 c(x,y,z)}{\partial x^2} + \frac{\partial^2 c(x,y,z)}{\partial y^2} + \frac{\partial^2 c(x,y,z)}{\partial z^2}\right) + \left(\frac{9}{4}u_{ave}\left(1-\frac{y^2}{a^2}\right)\left(1-\frac{z^2}{a^2}\right)\right)\left(\frac{\partial c(x,y,z)}{\partial x}\right) = 0 \qquad \text{(eq. 77)}$$

where

c	=	gas concentration, mol m^{-3}
t	=	time, s
D_{mol}	=	molecular diffusion coefficient, m^2 s^{-1}
x,y,z	=	position of column, m
u_{ave}	=	interstitial velocity, m s^{-1}

The LDF equation approximates the average loading within the solid as follows.

$$\frac{\partial \bar{q}(x)}{\partial t} = k\left(q^*(x) - \bar{q}(x)\right) \qquad \text{(eq. 78)}$$

where

$\bar{q}$	=	average loading within the solid, mol kg^{-1}
q^*	=	surface concentration at equilibrium with the gas, mol kg^{-1}
k	=	mass transfer coefficient

The adsorbed quantity (q^*) is in equilibrium with the gas and calculated using the Tóth equation:

$$q^*(x) = q_m \frac{bPc(x)/\rho_g}{\left(1+\left(bPc(x)/\rho_g\right)^t\right)^{1/t}} \qquad \text{(eq. 79)}$$

where

b	=	affinity coefficient, Pa^{-1}
P	=	Pressure, Pa
q^*	=	surface concentration in equilibrium with the gas, mol kg^{-1}
q_m	=	maximum solid loading, mol kg^{-1}
t	=	parameter of Tóth model

c = concentration of DCM in gas, mol m^{-3}

Initial Conditions

For the adsorption:

$$c(x, y, z) = c_0,\ \bar{q}(x) = 0 \quad \text{(eq. 80)}$$

For the desorption:

$$c(x, y, z) = 0,\ \bar{q}(x) = q_0 \quad \text{(eq. 81)}$$

Boundary Conditions

For the adsorption:

$$D_{mol} \frac{\partial c(0, y, z)}{\partial x} = u_{ave}\left(c(0, y, z) - c_0\right) \quad \text{(eq. 82)}$$

$$\frac{\partial c(L, y, z)}{\partial x} = 0 \quad \text{(eq. 83)}$$

$$\frac{\partial c(x, y, 0)}{\partial z} = 0 \quad \text{(eq. 84)}$$

$$\frac{\partial c(x, 0, z)}{\partial y} = 0 \quad \text{(eq. 85)}$$

$$D_{mol} \frac{\partial c(x, y, a)}{\partial z} = -\left(\frac{1}{a_s}\right)\rho_s \frac{\partial \bar{q}(x)}{\partial t} \quad \text{(eq. 86)}$$

$$D_{mol} \frac{\partial c(x, a, z)}{\partial y} = -\left(\frac{1}{a_s}\right)\rho_s \frac{\partial \bar{q}(x)}{\partial t} \quad \text{(eq. 87)}$$

where

W = $a + t_w$, m

a_s = geometrical presentation of area over volume, m^{-1}

For the desorption:

$$D_{mol}\frac{\partial c(0,y,z)}{\partial x} = u_{ave}\left(c(0,y,z) - c_0\right) \quad \text{(eq. 88)}$$

$$\frac{\partial c(L,y,z)}{\partial x} = 0 \quad \text{(eq. 89)}$$

$$\frac{\partial c(x,y,0)}{\partial z} = 0 \quad \text{(eq. 90)}$$

$$\frac{\partial c(x,0,z)}{\partial y} = 0 \quad \text{(eq. 91)}$$

$$D_{mol}\frac{\partial c(x,y,a)}{\partial z} = -\left(\frac{1}{a_s}\right)\rho_s\frac{\partial \bar{q}(x)}{\partial t} \quad \text{(eq. 92)}$$

$$D_{mol}\frac{\partial c(x,a,z)}{\partial y} = -\left(\frac{1}{a_s}\right)\rho_s\frac{\partial \bar{q}(x)}{\partial t} \quad \text{(eq. 93)}$$

7.2.3. Extended LDF approximation

The LDF equation at the interface is averaged and defined in the previous section in one dimensional matrix. But in the 3D configuration presented in Figure 84, two interfaces (q_{11} & q_{22}) are identified. Therefore, the LDF equation can be extended and configured in 2D where q_{11} is a function of x and z and q_{22} is a function of x and y. Or the LDF equation is reduced further and both q_{11} and q_{22} are defined in 1D as a function of x only. Both definitions of the LDF equations are presented as follows for q_{11} and q_{22}, respectively:

2D Interface:

$$\frac{\partial \bar{q}_{11}(x,z)}{\partial t} = k\left(q_{11}^{*}(x,z) - \bar{q}_{11}(x,z)\right) \quad \text{(eq. 94)}$$

$$\frac{\partial \bar{q}_{22}(x,y)}{\partial t} = k\left(q_{22}^{*}(x,y) - \bar{q}_{22}(x,y)\right) \quad \text{(eq. 95)}$$

1D Interface:

$$\frac{\partial \bar{q}_{11}(x)}{\partial t} = k\left(q_{11}^{*}(x) - \bar{q}_{11}(x)\right) \quad \text{(eq. 96)}$$

$$\frac{\partial \bar{q}_{22}(x)}{\partial t} = k\left(q_{22}^{*}(x) - \bar{q}_{22}(x)\right) \quad \text{(eq. 97)}$$

The adsorbed quantity (*q**) is in equilibrium with the gas and estimated by the Tóth equation:

2D Interface:

$$q_{11}^{*}(x,z) = q_m \frac{bPc(x,a,z)/\rho_g}{\left(1+\left(bPc(x,a,z)/\rho_g\right)^t\right)^{1/t}} \quad \text{(eq. 98)}$$

$$q_{22}^{*}(x,y) = q_m \frac{bPc(x,y,a)/\rho_g}{\left(1+\left(bPc(x,y,a)/\rho_g\right)^t\right)^{1/t}} \quad \text{(eq. 99)}$$

1D interface:

$$q_{11}^{*}(x) = q_m \frac{bPc(x)/\rho_g}{\left(1+\left(bPc(x)/\rho_g\right)^t\right)^{1/t}} \quad \text{(eq. 100)}$$

$$q_{22}^{*}(x) = q_m \frac{bPc(x)/\rho_g}{\left(1+\left(bPc(x)/\rho_g\right)^t\right)^{1/t}} \quad \text{(eq. 101)}$$

7.2.4. Mass balance equations in solid phase configuration

Once the equations of the gas phase are modelled in gPROMS, the degrees of freedom settled, and a solution is obtained, the diffusion equations in the solid domains can be introduced. By adopting the LDF approximation, diffusion inside the pores of the solid is calculated using the diffusion coefficient, knowing that the amount adsorbed equals the amount diffused within the solid.

The mass balances in the solid phase describe the diffusion of adsorbed DCM in the solid phase and are presented by the following equations related to the different domains (q_1, q_2 & q_3) presented in Figure 84:

$$\frac{\partial q_1(x,y,z)}{\partial t} = D_{eff}\left(\frac{\partial^2 q_1(x,y,z)}{\partial x^2} + \frac{\partial^2 q_1(x,y,z)}{\partial y_1^{\,2}} + \frac{\partial^2 q_1(x,y,z)}{\partial z_1^{\,2}}\right) \quad \text{(eq. 102)}$$

$$\frac{\partial q_2(x,y,z)}{\partial t} = D_{eff}\left(\frac{\partial^2 q_2(x,y,z)}{\partial x^2} + \frac{\partial^2 q_2(x,y,z)}{\partial y_2^{\,2}} + \frac{\partial^2 q_2(x,y,z)}{\partial z_2^{\,2}}\right) \quad \text{(eq. 103)}$$

$$\frac{\partial q_3(x,y,z)}{\partial t} = D_{eff}\left(\frac{\partial^2 q_3(x,y,z)}{\partial x^2} + \frac{\partial^2 q_3(x,y,z)}{\partial y_3^{\,2}} + \frac{\partial^2 q_3(x,y,z)}{\partial z_3^{\,2}}\right) \quad \text{(eq. 104)}$$

where

q_1,q_2,q_3	=	amount of VOC adsorbed, mol kg $^{-1}$
D_{eff}	=	effective diffusion coefficient, m^2s^{-1}
y_1, y_2, y_3	=	axes of distribution domains, m
z_1, z_2, z_3	=	axes, of distribution domains, m

$$q_3(x,y,a) = q_1(x,y,a) \quad \text{(eq. 105)}$$

$$q_3(x,a,z) = q_2(x,a,z) \quad \text{(eq. 106)}$$

Initial Conditions

$$c(x,y,z) = c_0,\ q_1(x,y,z) = 0,\ q_2(x,y,z) = 0,\ q_3(x,y,z) = 0, \quad \text{(eq. 107)}$$

2D interface:

$$\bar{q}_{11}(x,z) = 0,\ \bar{q}_{22}(x,y) = 0 \quad \text{(eq. 108)}$$

1D interface:

$$\bar{q}_{11}(x) = 0,\ \bar{q}_{22}(x) = 0 \quad \text{(eq. 109)}$$

Boundary Conditions

$$D_{mol}\frac{\partial c(0,y,z)}{\partial x}=u_{ave}\left(c(0,y,z)-c_0\right),\ \frac{\partial c(L,y,z)}{\partial x}=0 \quad \text{(eq. 110)}$$

$$\frac{\partial q_1(0,y,z)}{\partial x}=0,\ \frac{\partial q_1(L,y,z)}{\partial x}=0 \quad \text{(eq. 111)}$$

$$\frac{\partial q_2(0,y,z)}{\partial x}=0,\ \frac{\partial q_2(L,y,z)}{\partial x}=0 \quad \text{(eq. 112)}$$

$$\frac{\partial q_3(0,y,z)}{\partial x}=0,\ \frac{\partial q_3(L,y,z)}{\partial x}=0 \quad \text{(eq. 113)}$$

$$\frac{\partial c(x,y,0)}{\partial z}=0,\ \frac{\partial c(x,0,z)}{\partial y}=0 \quad \text{(eq. 114)}$$

$$\frac{\partial q_1(x,y,0)}{\partial z_1}=0,\frac{\partial q_1(x,W,z)}{\partial y_1}=0 \quad \text{(eq. 115)}$$

$$\frac{\partial q_2(x,0,z)}{\partial y_2}=0,\frac{\partial q_2(x,y,W)}{\partial y_2}=0 \quad \text{(eq. 116)}$$

$$\frac{\partial q_3(x,y,W)}{\partial z_3}=0,\frac{\partial q_3(x,W,z)}{\partial y_3}=0 \quad \text{(eq. 117)}$$

2D interface:

$$D_{mol}\frac{\partial c(x,y,a)}{\partial z}=-\left(\frac{1}{a_s}\right)\rho_s\frac{\partial \bar{q}_{22}(x,y)}{\partial t} \quad \text{(eq. 118)}$$

$$D_{mol}\frac{\partial c(x,a,z)}{\partial y}=-\left(\frac{1}{a_s}\right)\rho_s\frac{\partial \bar{q}_{11}(x,z)}{\partial t} \quad \text{(eq. 119)}$$

$$D_{eff}\frac{\partial q_2(x,y,a)}{\partial z_2}=-\left(\frac{1}{a_s}\right)\frac{\partial \bar{q}_{22}(x,y)}{\partial t} \quad \text{(eq. 120)}$$

$$D_{eff}\frac{\partial q_1(x,a,z)}{\partial y_1}=-\left(\frac{1}{a_s}\right)\frac{\partial \bar{q}_{11}(x,z)}{\partial t} \quad \text{(eq. 121)}$$

1D interface:

$$D_{mol}\frac{\partial c(x,y,a)}{\partial z}=-\left(\frac{1}{a_s}\right)\rho_s\frac{\partial \bar{q}_{22}(x)}{\partial t} \quad \text{(eq. 122)}$$

$$D_{mol}\frac{\partial c(x,a,z)}{\partial y}=-\left(\frac{1}{a_s}\right)\rho_s\frac{\partial \bar{q}_{11}(x)}{\partial t} \quad \text{(eq. 123)}$$

$$D_{eff}\frac{\partial q_2(x,y,a)}{\partial z_2}=-\left(\frac{1}{a_s}\right)\frac{\partial \bar{q}_{22}(x)}{\partial t} \quad \text{(eq. 124)}$$

$$D_{eff}\frac{\partial q_1(x,a,z)}{\partial y_1}=-\left(\frac{1}{a_s}\right)\frac{\partial \bar{q}_{11}(x)}{\partial t} \quad \text{(eq. 125)}$$

7.5. References

Ahn, H. & Brandani, S., 2005a. Analysis of breakthrough dynamics in rectangular channels of arbitrary aspect ratio. *AIChE Journal*, 51(7), pp.1980-1990.

Ahn, H. & Brandani, S., 2005b. Dynamics of carbon dioxide breakthrough in a carbon monolith over a wide concentration range. *Adsorption*, 11, pp.473-477.

Bird, R.B., Steward, W.E. & Lightfoot, E.N., 2002. Transport phenomena, second ed. Wiley International, Singapore.

Camus, O., Crittenden, B., Perera, S., Mays, T., Sánchez-Liarte, F., Patsos, A., Tennison, S. R. & Crezee, E., 2007. Non-uniformities in adsorbent monoliths, *In: 9th International conference on Fundamentals of Adsorption*, 20 - 25 May. Giardini Naxos, Sicily.

Cornish, R. J. 1928. Flow in a pipe of rectangular cross-section. *Proc R. Soc Lond. A Math Phys Sci*. 120, pp.691-700.

Crittenden, B. D., Camus, O., Perera, S. P., Mays, T. J., Sánchez-Liarte, F., Tennison, S. R. & Crezee, E., 2011. Nonuniform channels in adsorbent monoliths. *AIChE Journal*, 57(5), pp.1163-1172.

Grande, C. A., 2004. *Propane / Propylene separation by adsorption processes*. Ph.D. Dissertation. University of Porto.

Grande, C. A., Cavenati, S., Barcia, P., Hammer, J., Fritz, H.G. & Rodrigues, A.E., 2006. Adsorption of propane and propylene in zeolite for a honeycomb monolith, *Chemical Engineering Science*, 61, pp.3053-3067.

Kolade, M.A., Kogelbauer, A. & Alpay, E., 2009. Adsorptive reactor technology for VOC abatement, *Chemical Engineering Science*, 64, pp.1167-1177.

Nikolajsen, K. M., 2007. *Novel structured adsorber and oxidation catalysts for the removal of VOCs in low concentration*, PhD Thesis. Ecole Polytechnique Fédérale de Lausanne, Suisse.

Zabka, M., Minceva, M. & Rodrigues, A. E., 2006. Experimental and modelling study of adsorption in preparative monolithic silica column. *Chemical Engineering and Processing,* 45, pp.150-160.

Zabka, M., Minceva, M. & Rodrigues, A. E., 2007. Experimental characterization and modelling of analytical monolithic column. *Journal of Biochemical and Biophysical Methods*, 70, pp. 95-105.

Chapter 8

Three-dimensional modelling result

8.1. Adsorption process simulation

The 3D model developed in Chapter 7 is used in modelling the breakthrough curve of the adsorption process. This curve is compared to the experimental data then validated at different operating conditions. The 3D profiles resulting from the 3D model are also presented and evaluated.

8.1.1. Adsorption breakthrough curve

The 3D model developed in the previous Chapter produces the adsorption breakthrough curve. Namely, the 3D model using the extended LDF approximation is used where the average loading at the interfaces are $\bar{q}_{11}(x, z)$ and $\bar{q}_{22}(x, y)$. The resulting breakthrough curve for the bench scale is compared to that produced experimentally at the University of Bath. The parameters are those given in Table 3 of Chapter 5. Figure 86 shows how these two curves compare with each other. It is clear that the gPROMS 3D modeled curve produces a good fit with the experimental data.

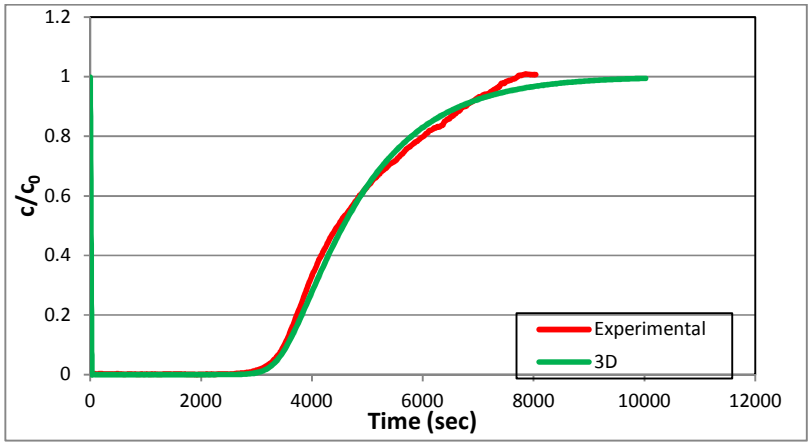

Figure 86. 3D modelled vs. experimental breakthrough curves

8.1.2. Parameter estimation

Parameter estimation was conducted for the 3D model on the mass transfer coefficient (*k*). For the 1D model presented in an earlier Chapter, a previous parametric study was conducted and a value of 0.0008 s^{-1} was used for the mass transfer coefficient (*k*). Parameter estimation is conducted in Figure 87. Three values of mass transfer coefficient (0.001 s^{-1}, 0.0009 s^{-1}, 0.0008 s^{-1}) were tested.

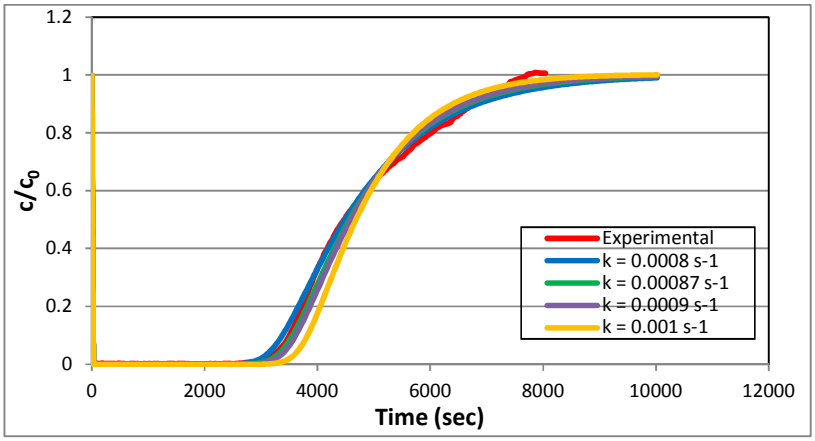

Figure 87. Effect of varying mass transfer coefficient on breakthrough curves

Based on Figure 87, parametric estimation for the mass transfer coefficient did not produce a better value than the one used in the 1D model. Therefore the value of

0.0008 s^{-1} predicted for the mass transfer coefficient (k) is used in both 1D and 3D modelling.

8.1.3. Validation at different operating conditions

The 3D model was validated at different operating conditions from the one presented in Figure 86 which was 7.2 l min^{-1}. Two other operating conditions (5 l min^{-1} and 9 l min^{-1}) were used in the validation process, as carried out previously for the 1D model. Figures 88 and 89 show the predicted breakthrough curves vs. the experimental ones, respectively.

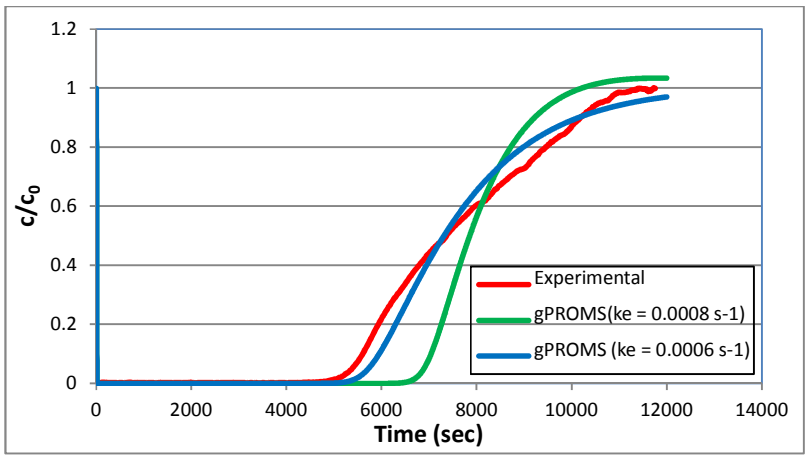

Figure 88. 3D breakthrough curve at 5 l min^{-1} (k_e = 0.00087459 s^{-1} & 0.00061552 s^{-1})

Figure 88 compares the experimental breakthrough curve at 5 l min^{-1} with the predicted 3D curves at two mass transfer coefficients (k = 0.00087459 s^{-1} & 0.00061552 s^{-1}). These were the mass transfer coefficients tested earlier in Chapter 6 for the 1D model. As can be seen a mass transfer coefficient of 0.00061552 s^{-1} produced a better matching breakthrough curve with the experimental data. This was also the case for the 1D model.

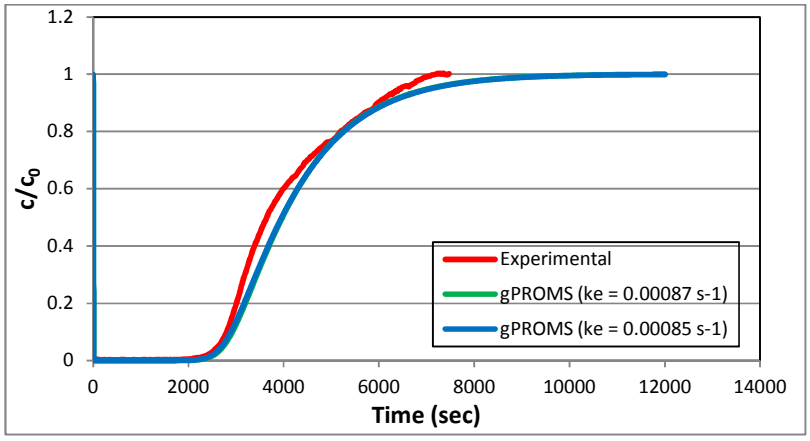

Figure 89. 3D breakthrough curve at 9 l min^{-1} (k = 0.00087459 s^{-1} & 0.0008597 s^{-1})

Figure 89 compares the experimental breakthrough curve at 9 l min^{-1} operating condition with the predicted 3D curves at two mass transfer coefficients (k = 0.00087459 s^{-1} & 0.0008597 s^{-1}) tested for the 1D model in Chapter 6. The effect of the mass transfer coefficient is not apparent in the Figure, as resulting breakthrough curves overlap.

Figures 87, 88 & 89 validate the developed 3D model at three different operating conditions and compare their predicted breakthrough curves with their corresponding experimental data. The mass transfer coefficient affects the breakthrough curves and requires a parameter estimation study to set these parameters at each operating condition. This effect is mostly noticeable at lower flow rates. Henceforth, k is set at 0.0008 s^{-1} as it was for the 1D model in Chapter 6.

8.2. 3D Profiles

The 3D model developed in gPROMS produces profiles for concentration and uptake. These profiles correspond to the breakthrough curve in the gas channel in the three coordinates, the uptake at the interface and the adsorption in the solid domains.

8.2.1. Gas channel

The breakthrough curve resulting from the 3D model with extended LDF approximation is presented in 3D configuration in Figure 90 in term of c/c_0 as a function of time along the gas channel.

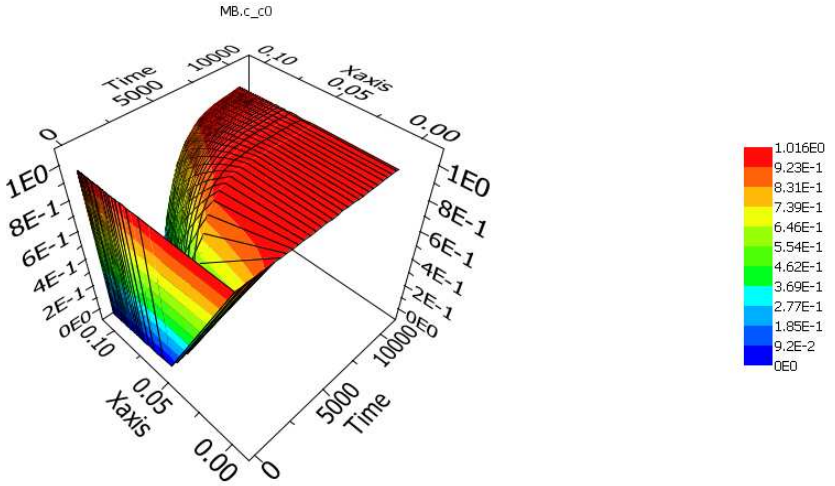

Figure 90. Breakthrough curve in *x* direction in 3D presentation for c/c_0 (the vertical axis)

The same breakthrough curve is presented in Figure 91 but in terms of absolute concentration (c). The value of c reaches the initial concentration (c_0) upon saturation. The path of the mass transfer zone travelling down the length of the column, denoted by the *x* axis, is illustrated in Figures 90 and 91.

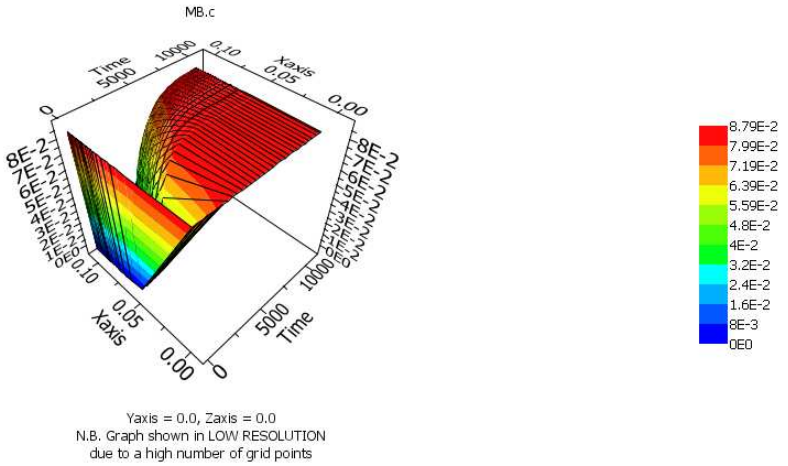

Figure 91. Breakthrough curve in *x* direction in 3D presentation for c (the vertical axis)

The breakthrough curve is also presented in Figures 92 and 93 in terms of concentration over the *y* and *z* axes, respectively. The concentration profile over the *y* axis or the *z* axis is uniform, as illustrated in the Figures.

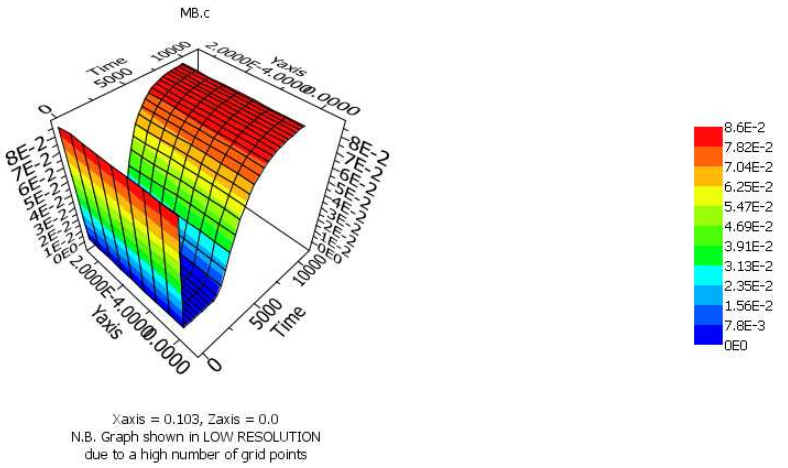

Figure 92. Breakthrough curve in *y* direction in 3D presentation at end of channel for *c* (the vertical axis)

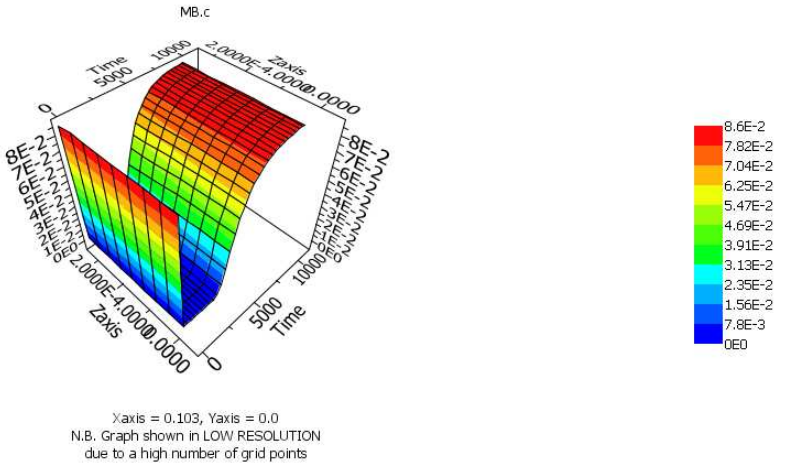

Figure 93. Breakthrough curve in *z* direction in 3D presentation at end of channel for *c* (vertical axis)

The fact that the concentration profile is uniform over the *y* and *z* axes verifies that the concentration gradient over these axes is negligible, and that the concentration gradient over the length of the channel dominates. Consequently, using a simpler, one-

dimensional model, which takes only account of the concentration change in the axial direction and assumes perfect mixing of the gas along the *y* and *z* axes would be justified for the current study.

Figures 94 and 95 illustrate the uptake along the length of the column at the interfaces q_{11} and q_{22}, respectively. The average uptake at the interfaces is calculated using the extended LDF approximation. The average loading reaches a maximum value of 3045 mol m^{-3}, which is lower than the ACM maximum loading of 4680 mol m^{-3}.

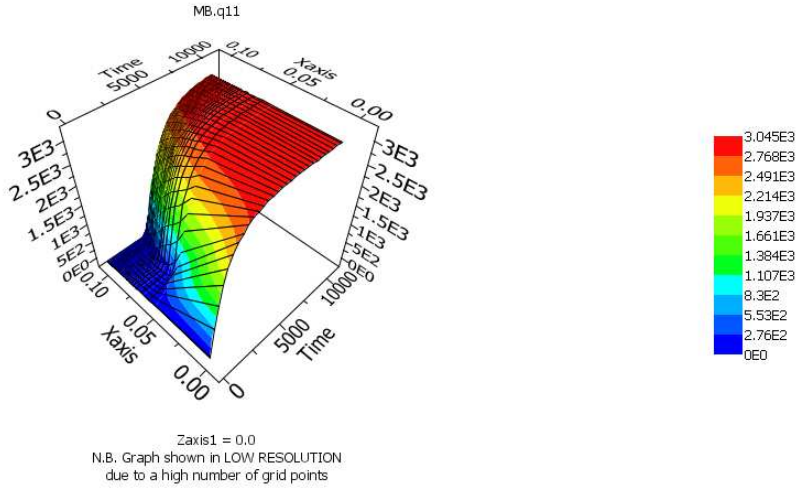

Figure 94. Uptake q_{11} (vertical axis) at the interface in *x* direction

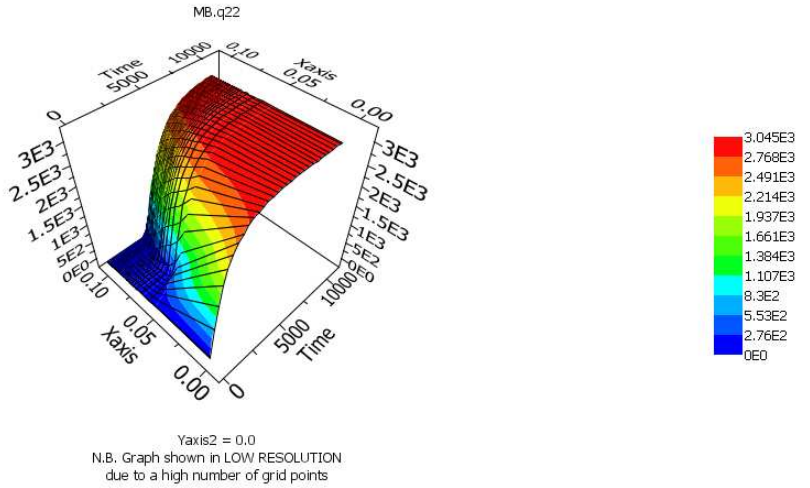

Figure 95. Uptake q_{22} (vertical axis) at the interface in *x* direction

Figure 96 shows the uptake along the *z* axis at the q_{11} interface at the entrance for the column. Figure 97 also shows the uptake along the *z* axis at the q_{11} interface but at the end of the monolithic column. Similar figures to Figures 96 and 97 could be produced for the q_{22} interface along the *y* axis. These figures illustrate a uniform uptake at the interface over the studied axis. The average uptake at the beginning and end of the monolithic column is affected by the travelling mass transfer zone along the column.

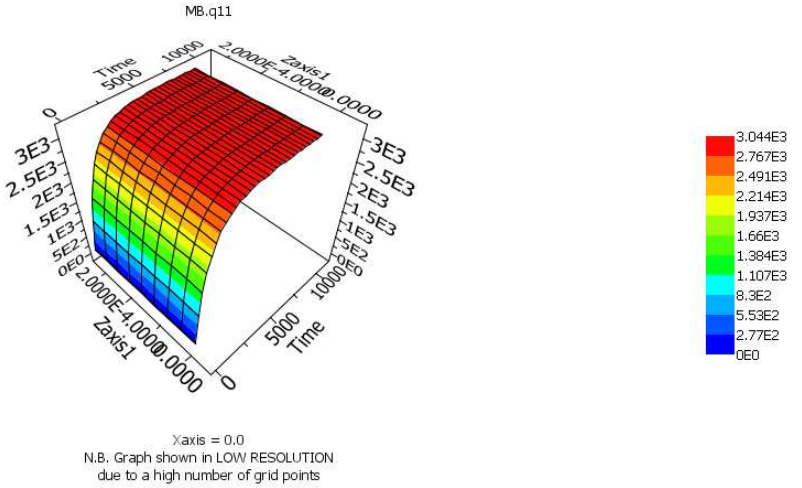

Figure 96. Uptake at the interface q_{11} (vertical axis) in *z* direction at the beginning of the column

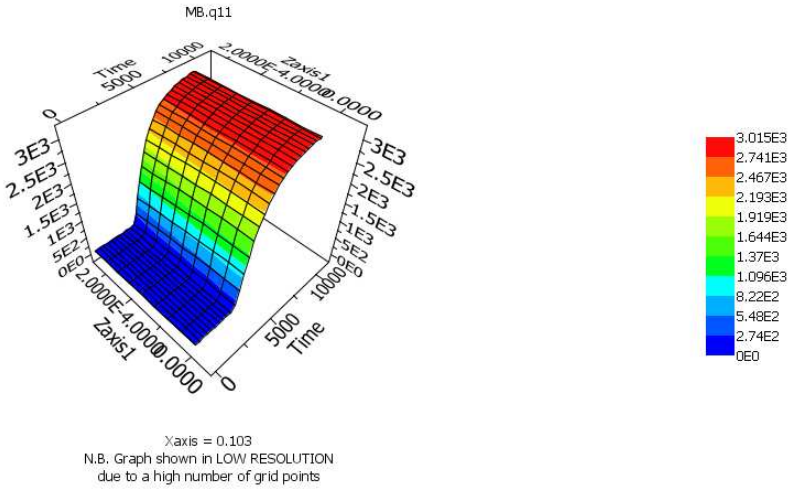

Figure 97. Uptake at the interface q_{11} (vertical axis) in *z* direction at the end of the column

The average uptake at the interfaces is estimated by the LDF approximation based on the concentration in the gas channel. The uniformity of uptake profile at the interfaces over the *y* and *z* axes conforms with the symmetry of the square channel. Also this uniformity demonstrates that variation is only observed over the length of the channel. Again, using a simpler, one-dimensional model, which takes account only of the changes in the direction of the x axis, would be justified for the current study.

8.2.2. Adsorption in solid phase

As modelled in the previous Chapter, the 3D model can be extended to account for the adsorption in the solid domain. The solid domain was divided into three sections as described in Chapter 7. These sections were two rectangles (q_1 and q_2) and one square q_3. As detailed in the previous Chapter, the loading in each section was calculated based on the diffusion coefficient (D_{eff}) and the boundary conditions at the interfaces. Figures 98, 99 and 100 illustrate the loading in each sections of the solid (q_1, q_2 and q_3), respectively. As expected, the loading in q_1 and q_2 are identical due to symmetry. Loading in q_1, q_2 and q_3 reached a maximum of 3198 mol m^{-3}.

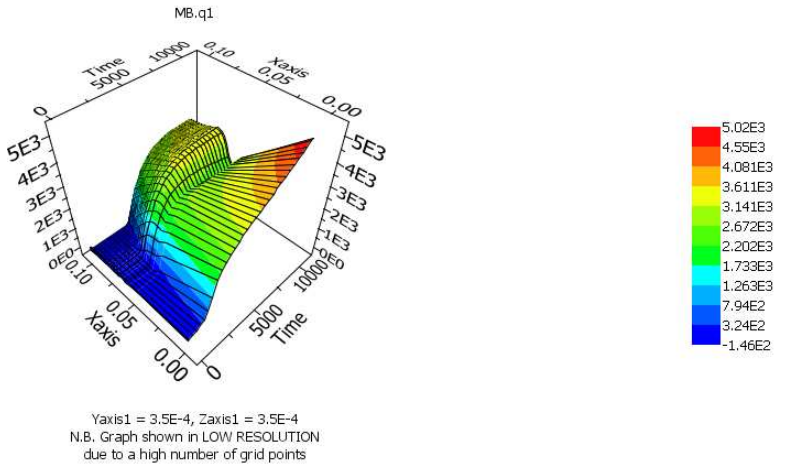

Figure 98. q_1 Uptake in *x* direction (vertical axis) in 3D presentation

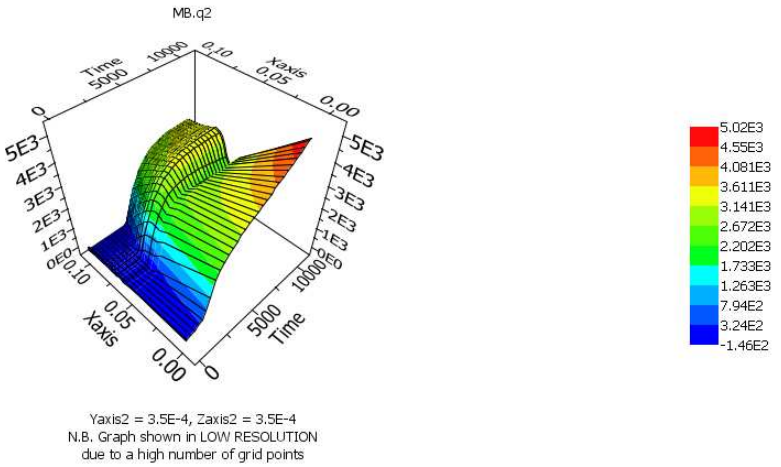

Figure 99. q_2 uptake in x direction (vertical axis) in 3D presentation

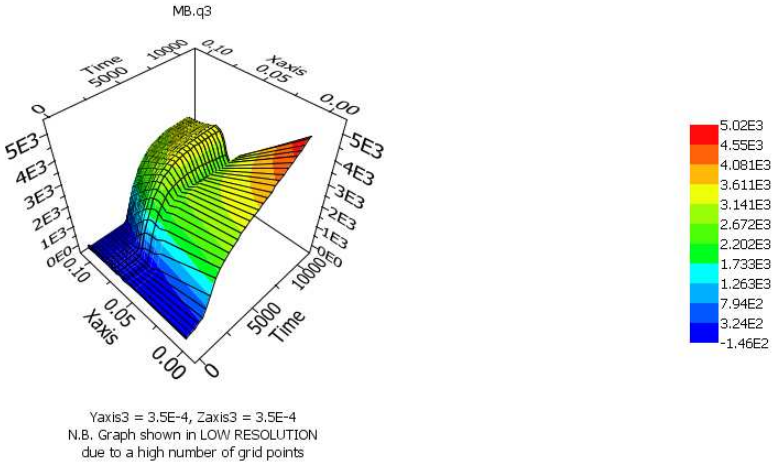

Figure 100. q_3 uptake (vertical axis) in 3D gPROMS modelling

As can be seen in Figures 98 - 100, the profiles of the uptakes in the solid domains are identical and their shapes match the profiles of the overall uptake q_{11} and q_{22}, but with different maximum values. The loading profiles of the three solid domains, however, show a significant valley halfway down the length of the channel. This valley could be attributed to the fact that the execution output reported that the iteration became stuck during the execution of the process. This problem arose from about x = 0.05 m up to about x = 0.08 m. From x = 0.08 m to the end of the monolith, x = 0.103 m, the problem did not arise.

Figures 101 and 102 show the loading in q_1 in the y and z directions, respectively. The loading reached slightly different values in the two figures due to the configuration of the rectangular solid section q_1. The loading reached a value of 3176 mol m^{-3} in the y direction and 3225 mol m^{-3} in the z direction. These values are reasonable when compared with the average loading predicted at q_{11} which amounted to 3045 mol m^{-3}. Similar figures can be produced for q_2 and q_3.

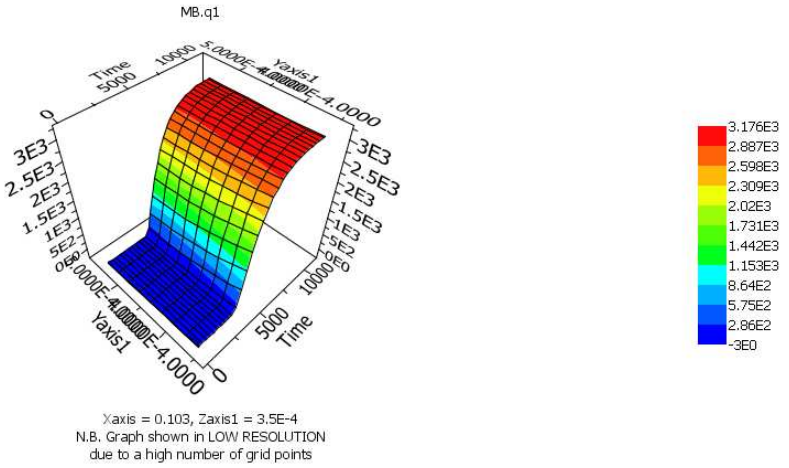

Figure 101. q_1 uptake in 3D configuration in the direction of the y axis

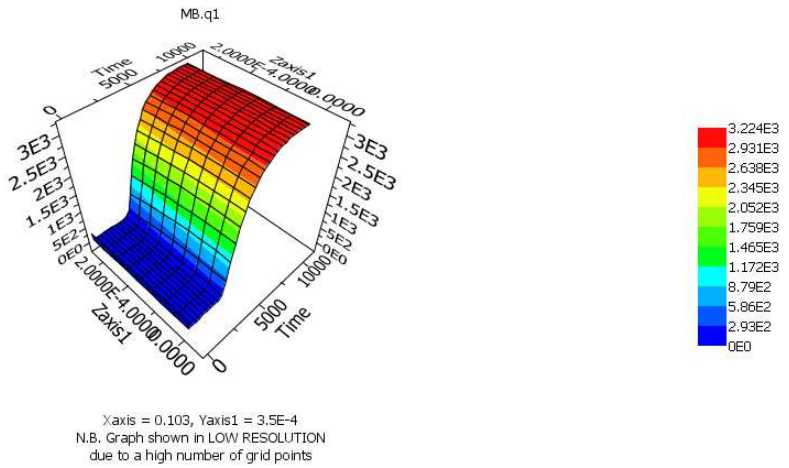

Figure 102. q_1 uptake in 3D configuration in the direction of the z axis

The profiles of q_1, q_2 and q_3 in the y and z axes demonstrate the fact that no loading variation takes place in the y and z axes within the solid monolith. This outcome is expected due to the use of the LDF approximation that produces an average loading since the loading in the solid domains are calculated from the effective diffusion coefficient. Again this fact is expected as no variation was observed in the gas concentration in the y and z directions. Consequently, 1D modelling can be considered sufficient to satisfy the conditions of the current study.

8.3. Desorption process simulation

The 3D model is also used to simulate the desorption process in configuration using the parameters pertaining to the bench scale as presented in Table 3 of Chapter 5. From the 3D profiles of the desorption process, it was observed that variation in the gas phase concentration only occurred in the axial direction (x). The desorption breakthrough curves in both the y and z directions had uniform profiles. Also variation of the desorbed average loading (q_{11} and q_{22}) from the solid to the purge gas was only occurring in the axial direction and average desorption from the solid monolith to the gas phase was uniform in both the y and z directions.

Desorption from the individual solid domains (q_1, q_2 and q_3), however, encountered convergence issues. The predicted 3D profiles for q_1, q_2 and q_3 were not very realistic. Convergence problems were also encountered in the 3D profiles of adsorption in the solid, as was seen in section 8.2.2. Therefore, it can be concluded that 3D modelling in the solid domains was encountering convergence issues both in adsorption and desorption. The convergence issues in the solid phase could be attributed to use of the LDF approximation in the model. The use of this approximation will be discussed further in Chapter 9.

8.4. Conclusion about 3D modelling

Vis-à-vis the findings on 3D modelling presented in this Chapter and the findings on 1D modelling presented in Chapter 6, it can be concluded that no benefit is to be gained by using 3D modelling for the current system of interest. No variations in the y

and *z* directions were observed in the 3D profiles for both adsorption and desorption. Hence, the 1D model can be used effectively to interpret adsorption, desorption and the cyclic process for the recovery of VOC on a MAST carbon monolith. That is not to say that 3D modelling would have no value in other monolithic adsorption processes or systems. Further discussion on 1D vs. 3D modelling will be presented in Chapter 9.

Chapter 9

Discussion

This Chapter discusses some of the findings presented in the previous Chapters, especially, the comparison between the 1D and 3D models, the evaluation of the LDF approximation, and the implication of the mass transfer coefficient.

9.1. 1D vs. 3D modelling

For the sake of this study, 1D and 3D modelling have been presented. Chapters 5 and 6 present modelling in the 1D configuration; while Chapters 7 and 8 cover 3D modelling. 1D modelling was initiated as a building block in the development of the 3D model. The 1D model was established for adsorption, desorption and the cyclic process. 3D modelling, on the other hand, was developed to be potentially more accurate although it was found that 1D modelling was sufficient for the current study. This finding is confirmed next.

9.1.1. 1D vs. 3D in gPROMS

The gPROMS modelled 3D breakthrough curve is compared to the modelled gPROMS 1D curve, in earlier Chapters. Figure 103 now compares the 1D and 3D curves to the experimental breakthrough curve. As can be seen in the figure, the two gPROMS curves coincide at their upper part, but the 3D model is a poorer fit as seen for the beginning of the breakthrough curve. The coefficients of determination for the two curves are 0.9738 and 0.9728 for the 1D and 3D curves, respectively.

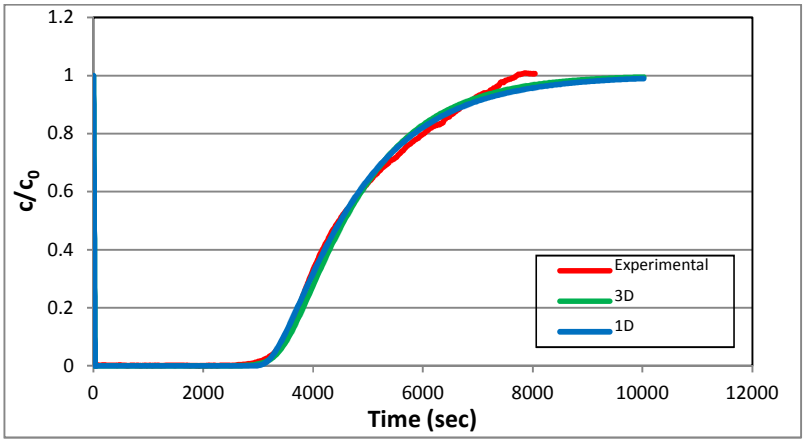

Figure 103. 1D & 3D modelled vs. experimental breakthrough curves

It can be seen therefore that 1D modelling presents a good approximation for the experimental data without going through the trouble of 3D modelling which is more demanding in terms of formulation. In addition, 3D modelling is generally computationally more extensive. For example, simulation took two seconds to run the 1D developed model in gPROMS with a total CPU time of 0.203 seconds. On the other hand, the simulation took 99 seconds to run the 3D model including the solid domains with a total CPU time of 81.277 seconds.

9.1.2. 3D gPROMS vs. 3D COMSOL

At the University of Bath, 3D modelling was conducted using COMSOL (Crittenden, *et. al*., 2011). Figure 104 compares the experimental data with the modelled 3D curves using both COMSOL and gPROMS. The modelled breakthrough curves coincide in their higher parts, but the gPROMS breakthrough curve takes more time to initial breakthrough. The COMSOL breakthrough curve starts earlier. The coefficients of determination for the two curves are 0.99413 and 0.9728 for the COMSOL and gPROMS curves, respectively.

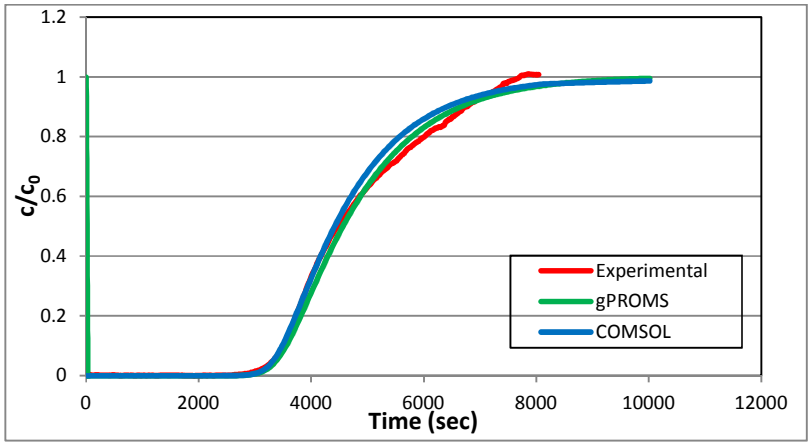

Figure 104. 3D modelled vs. experimental breakthrough curves

The COMSOL breakthrough curve seems to be slightly better than the gPROMS curve based on the coefficient of the determination. The gPROMS curve takes more time to breakthrough but does not show the strong concavity at the upper part of the curve.

9.1.3. 1D gPROMS vs. 3D COMSOL

The 1D model developed in gPROMS is next compared to the 3D model constructed at the University of Bath using COMSOL. Figure 105 illustrates the comparison between the resulting adsorption breakthrough curves along with the experimental data.

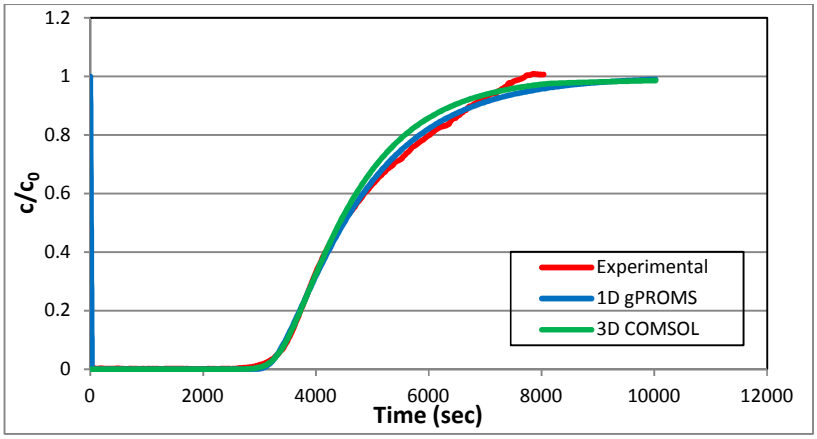

Figure 105. 1D modelled gPROMS, 3D modelled COMSOL vs. experimental breakthrough curves

The coefficient of determination is higher for the COMSOL breakthrough curve (0.99413) than that of the 1D gPROMS model (0.9738). However, the shape of the 1D curve demonstrates less concavity at its upper part and seems to fit the experimental data better.

The difference between the two models could also be attributed to the discretisation method used. COMSOL Multiphysics software uses the finite element method (FEM). gPROMS, on the other hand, uses the finite difference method (FDM) for resembling the solution to the differential equations.

The advantage of the 1D model remains in the fact that it can be developed into a cyclic process of operation in gPROMS, unlike the 3D model developed in COMSOL which is constrained by the COMSOL limitation in solving the integral process. This aspect has been reported by Petkovska, *et al*. (2007) who used COMSOL and MATLAB in combination to simulate the TSA cycle (Petkovska, *et al*., 2007).

9.1.4. Comparison with the literature

The literature was generous in supplying information on 1D modelling in comparison with 3D modelling which has only been conducted in a limited number of studies. Bonjour, *et al*. (2005), Clausse, *et al*. (2004) and Yu, *et al*. (2007) have all claimed that under characteristic conditions used in the monolithic column, a one-dimensional model is adequate to describe the experimental data because of the relatively minor effect of concentration in the other coordinates (radial, y or z directions).

Ahn and Brandani (2005a) showed that it is feasible to match precisely the 3D simulation results using a 1D model of adsorption. This was done by specifying an equivalent system dimension. The computational time thereby was reduced to one second or less for a single channel breakthrough. According to Ahn and Brandani (2005a) several hours are required to get the numerical solution to the 3D model on a high performing computer (Ahn & Brandani, 2005a and 2005b).

Grande, *et al*. (2006) conducted modelling in different configurations for propane and propylene adsorption in zeolite 4A honeycomb monolith. A complete 3D model was developed in addition to a simplified model to describe the adsorption step. A

comparison between these models was conducted illustrating that the simplified model could be utilized without losing precision but reducing significantly the computational time (Grande, *et al*., 2006).

In a personal communication, Grande justified the use of a simplified model instead of the 3D model: "Regarding the 3D model, I can give you some advices. First one, try to avoid it! Unless you think it is completely necessary, it will consume a lot of your time and the results are not that different from what you get with the simplified model. In case you have to do it, note that you may experience two kinds of problems: first one is related to code (you have to define several domains filled almost with zeros). The second one is a direct result of the first one: convergence problems. You have lots of zeros in one side (gas or solid), and on the other side you have the same variable with its maximum value. I have experienced them even having a very slow kinetics of diffusion. So it would not be a surprise to have convergence problems in “normal” cases." (C. Grande, personal communication, May 21, 2011). As can be seen from the previous Chapters, Grande's advice is particularly pertinent.

Perdana, *et al*. (2007) used 2D and 3D models for kinetic modeling of NOx adsorption. The use of a 2D model was adequate to study adsorption transport and kinetics. The 3D model, in comparison with the 2D, gave similar concentration profiles but in a 3D view despite its greater computational demands.

Crittenden, *et al*. (2011), on the other hand, used 3D modeling and confirmed that 1D modeling is limited in predicting the performance of the monolithic column. The authors confirmed the necessity to model the gas phase convection-diffusion in 3D, as the maximum gas phase concentration exists on the middle axis while the lowest concentration exists in the corners (Crittenden, *et al*., 2011).

Two-dimensional (2D) model has been used in some studies to represent mainly the solid phase influenced by the diffusion rate. Petkovska, *et al*. (2007) noticed that the concentrations and temperatures change both in the axial and radial directions. Therefore, the use of a simpler one-dimensional model might not be justified in their systems (Petkovska, *et al*., 2007).

The adequacy of the 1D model in comparison to 2D and 3D modelling is debatable. Of course individual studies and their corresponding operational conditions

differ. Nontheless for the current study, 1D modelling is sufficient to adequately represent the ESA cyclic process.

9.2. LDF approximation

The LDF approximation has been used throughout this study in the development of the 1D and 3D models. The LDF approximation is used to estimate the average amount of VOC adsorbed onto the surface of the activated carbon. Crittenden, *et al*. (2011) used the LDF approximation in their 3D model to approximate the average loading. Zabka, *et al*. (2006 & 2007) transformed the mass balance of the channel wall into an LDF equation. Grande (2004) in his thesis used the LDF approximation in the gas phase continuity equation to account for the divergence among the bulk gas concentration and the gas concentration at the channel surface. By adopting the LDF approach, the diffusion model for the adsorbed VOC can be eliminated and the overall rate of uptake can be estimated. The LDF approach, therefore, reduces the complexity of the model.

Other studies, however, have not used the LDF in their work. For example, Grande, *et al*. (2006) only equated the mass fluxes at the interface of the gas and solid. Ahn and Brandani (2005a) also equated the mass fluxes at the fluid-solid interface and used a linear adsorption isotherm to account for equilibrium at the channel surface.

The LDF approximation can also be used at the pore level. Grande, *et al.* (2006) used the LDF expression to account for adsorption in the zeolite crystals inserted into the ceramic monolith wall. Kolade, *et al*. (2009) used the LDF expression to describe the intra-particle mass transfer in the solid zone encompassing the adsorbent and the catalyst. LDF is used to calculate the rate of adsorption at the particle level where a modified effective gas diffusion coefficient is devised. However, in order to consider adsorption at the micro-scale, additional considerations and parameters are needed, such as an LDF expression for the intra-particle mass transfer and a modified effective diffusion coefficient for the rate of adsorption in a particle.

In conclusion, the LDF approach at the gas/solid interface remains a valid assumption and provides an overall approximation of the rate of adsorption in the solid

phase. Therefore, for the current study, the LDF approximation has been used in both 1D and 3D modelling. For the 3D model, the mass balance in the gas phase seems to be adequate with the use of the extended LDF approximation to estimate the average loading in the solid, especially since no adsorption data at the pore level inside the monolith is available. From the LDF approximation, the diffusion inside the pores of the solid is then calculated using the diffusion coefficient knowing that the amount adsorbed equals the amount diffused within the solid. However, the 3D mass balance in the solid phase seems less adequate based on the 3D profiles presented in the previous Chapter.

9.3. Mass transfer coefficient

The effect of diffusion is of vital significance to monolithic adsorbent simulation and design. A precise understanding of the mass transfer coefficient is indispensable for modelling and prediction of monolithic performance. The effect of mass transfer coefficient on the breakthrough curve is very important is comparison to the effect of other parameters of the mass balance equation. Higher value of mass transfer coefficient results in a steeper breakthrough curve indicating greater loading onto the ACM, and thereby a narrow MTZ that signifies a more efficient use of the monolithic channel.

Two main mass transfer mechanisms are taking place in a monolithic channel; an external mass transfer from the gas bulk to the channel wall and an internal mass transfer within the porous monolith. The controlling regime, whether external or internal transfer, depends on the geometric properties of the monolith and the flow properties. Both the external mass transfer from the bulk gas to the monolithic surface and the internal transfer related to the diffusion within the monolithic pores must be considered.

As concluded in Chapter 6, the effect of external resistance was found to be negligible in comparison to the internal one, and the overall mass transfer coefficient was therefore essentially a function of the internal one only. The dominating internal mass transfer coefficient encompasses both molecular and Knudsen diffusion. Molecular diffusion calculated using the Chapman-Enskiog equation seems to be dominating based on the analysis discussed in section 6.2.2 indicating that the dimension of the gas molecules is much smaller than the pore diameter. Gaseous collisions are more frequent

than collisions of the DCM molecules with the pore walls, and ordinary bulk diffusion occurs.

In addition, the dominating internal mass transfer coefficient is directly related to the effective diffusion coefficient as approximated by Glueckauf (1955) and Patton, *et al*. (2004). Both approximations relate the internal mass transfer coefficient to the effective diffusion coefficient using a geometrical transformation. In addition to the suitability of the geometrical transformation, the effective diffusion coefficient has a major impact on the breakthrough curve.

For the current study, the mass transfer coefficient was estimated for the developed 1D and 3D models based on a parameter estimation study. Neither the Glueckauf (1955) nor the Patton, *et al*. (2004) approximations predicted the best mass transfer coefficient, probably due to the unsuitability of their geometrical adaptations. Instead, the best values of mass transfer coefficient were found by parameters estimation methods (fitting of curves and the use of gPROMS).

9.3. References

Ahn, H. & Brandani, S., 2005a. Analysis of breakthrough dynamics in rectangular channels of arbitrary aspect ratio. *AIChE Journal*, 51(7), pp.1980-1990.

Ahn, H. & Brandani, S., 2005b. Dynamics of carbon dioxide breakthrough in a carbon monolith over a wide concentration range. *Adsorption*, 11, pp.473-477.

Bonjour, J., Clausse, M. & Meunier, F., 2005. A TSA process with indirect heating and cooling: parametric analysis and scaling-up to practical sizes. *Chemical Engineering and Processing*, 44, pp.969-977.

Clausse, M., Bonjour, J. & Meunier, F., 2004. Adsorption of gas mixture in TSA adsorbers under various heat removal conditions. *Chemical Engineering Science*, 59, pp.3657-3670.

Crittenden, B. D., Camus, O., Perera, S. P., Mays, T. J., Sánchez-Liarte, F., Tennison, S. R. & Crezee, E., 2011. Nonuniform channels in adsorbent monoliths. *AIChE Journal*, 57(5), pp.1163-1172.

Glueckauf, E. 1955. Part 10 – Theory of chromatography. Formula for diffusion into spheres and their application to chromatography. *Trans Faraday Soc,* 51, pp.1540-1551.

Grande, C. A., 2004. *Propane / Propylene separation by adsorption processes*. Ph.D. Dissertation. University of Porto.

Grande, C. A., Cavenati, S., Barcia, P., Hammer, J., Fritz, H.G. & Rodrigues, A.E., 2006. Adsorption of propane and propylene in zeolite for a honeycomb monolith, *Chemical Engineering Science,* 61, pp.3053-3067.

Grande, C., 2011. *Discussion on modelling* [email] (Personal communication, 21 May 2011).

Kolade, M.A., Kogelbauer, A. & Alpay, E., 2009. Adsorptive reactor technology for VOC abatement, *Chemical Engineering Science***,** 64, pp.1167-1177.

Patton, A., Crittenden, B. D. & Perera, S. P., 2004. Use of the linear driving force approximation to guide the design of monolithic adsorbents. *Chemical Engineering Research Des*., 82, pp. 999-1009.

Perdana, I., Creaser, D., Made Bendiyasa, I. & Rochmadi, Tyoso, B. W., 2007. Modelling NOx adsorption in a thin NAZSM-5 film supported on a cordierite monolith. *Chemical Engineering Science*, 62(15), pp.3882-3893.

Petkovska, M., Antov-Bozalo, D., Markovic, A. & Sullivan, P., 2007. Multiphysics modeling of electric-swing adsorption system with in-vessel condensation. *Adsorption*, 13(3-4), pp.357 -372.

Yu, F. D., Luo, L. A. & Grevillot, G., 2007. Electrothermal swing adsorption of toluene on an activated carbon monolith: Experiments and parametric theoretical study. *Chemical Engineering and Processing: Process intensification*, 46 (1), pp.70-81.

Zabka, M., Minceva, M. & Rodrigues, A. E., 2006. Experimental and modelling study of adsorption in preparative monolithic silica column. *Chemical Engineering and Processing*, 45, pp.150-160.

Zabka, M., Minceva, M. & Rodrigues, A. E., 2007. Experimental characterization and modelling of analytical monolithic column. *Journal of Biochemical and Biophysical Methods*, 70, pp. 95-105.

Chapter 10

Conclusions and Recommendations

Volatile organic compounds (VOC) are harmful air pollutants threatening the public health, and activated carbon monoliths (ACM) are considered suitable for the recovery of low concentration VOCs from air streams by the adsorption process. Mathematical modelling of the adsorption/desorption process proposes a model that can be applied on a prototype unit, like the one illustrated on Figure 106, for the recovery of VOCs in the chemical industry.

Figure 106. First commercial ACM fast cycle solvent recovery unit (Crittenden, 2011)

The aim of this thesis is to control and manage VOCs in air streams. Its objective lies in developing and validating a process model for the adsorption/desorption process,

and its scope is to model the cyclic ESA process for the recovery of VOC namely DCM using ACM from MAST Carbon Technology Ltd.

Mathematical modelling constitutes heart of the present work covering the basic concepts of adsorption equilibrium and kinetics, choosing the modelling software and selecting the modelling approach. One-dimensional modelling was the building block for the development of the three-dimensional model. The modelling equations, parameters and structure were constructed in 1D configuration. A parametric study and parameter estimation were conducted for the model different parameters. The adsorption, desorption and cyclic modes of operation were tested. Finally, the model was validated on the bench and pilot scales and for another type of VOC. Three-dimensional modelling of the adsorption process was then attained, and the aspects differentiating 1D from 3D modelling were covered.

10.1. Conclusions

A number of specific conclusions can be drawn from research presented in this thesis:

- The 1D model adequately represents the experimental data at the bench and pilot scales, at different operating conditions, for dichloromethane in experiments carried out at the University of Bath and for a different type of VOC (toluene) studied elsewhere.
- The 1D model is sufficient for the current study to represent adsorption, desorption and the cyclic process (from start-up) without going through the additional trouble of using 3D modelling which is generally more demanding in terms of formulation and computation.
- The 3D model does not enhance the fitness of the breakthrough curves to the experimental data, as it gives uniform concentration profiles in the y and z directions indicating that no concentration gradient is observed in directions perpendicular to flow.
- This does not mean that the 3D model has no value in other process applications. What it means is that it has no particular value in the study of VOC adsorption

onto MAST carbon monolith under the conditions of experiments carried out at the University of Bath.

- The LDF approximation is a valid assumption used in the mass balance of 1D and 3D modelling to adequately predict the concentration in the gas phase without going into a fundamental diffusion study within the solid.
- The mass transfer coefficient used in the LDF approximation is directly related to the internal mass transfer coefficient which is found to be controlled mainly by molecular diffusion inside the pore structure of the monolith.
- The values of the mass transfer coefficients are found by parameter estimation based on their corresponding adsorption or desorption breakthrough curves. There is good consistency between values of adsorption and desorption when temperature differences are taken into account.

10.2. Recommendations

Based on the conclusions devised from the current study, the following recommendations are proposed for future work:

- The 1D model was developed in the current study for a single channel with the assumption that all the channels in a monolith are equal in size and shape. Crittenden, *et al.* (2011), however, considered non-uniform channel geometries in adsorbent monoliths to model the adsorption of VOC on a MAST ACM. Therefore, it is recommended to develop the 1D model further so that it can be used with monoliths that have non-uniform channels. This model could then be developed further to buildup a simulation of the full cycle.
- One of the major assumptions made in the present study is the use of LDF approximation at the gas solid interface. Even though an extended LDF approximation was used accounting for the full surface area of the interface, the LDF equation remains an approximation. Therefore, it is recommended to apply the LDF approximation at the pore level by deriving the rate of adsorption at the micro-scale level where a modified effective gas diffusion coefficient is needed.

- Another consideration is related to the parameters used in the modelling equations. Petkovska, *et al*. (2007) used fixed parameters for both adsorption and desorption. In the current study, temperature dependent parameters were calculated for both the adsorption and desorption steps. To take these parameters one step further, it is recommended to incorporate parametric equations within the model to account for both concentration and temperature variations. In addition, incorporating parametric equation within the cyclic model enhances the prediction of heating and cooling curves. For example, the isosteric heat of adsorption equation needs to be incorporated in the model, as Shen, *et al*. (2011) reported that the isosteric heat of adsorption varies with the surface loading. It was also demonstrated in this thesis that the mass transfer coefficient is temperature dependent, and its value needs to be adjusted for the changing temperature profile during regeneration.
- Finally, the energy balance used in modelling was derived based on a number of assumptions and limitations. A number of terms are included in the energy balance, among which is a term that characterizes the type of heating used in regenerating the ACM. The adsorption process used in the current study is ESA, a specific type of TSA. In order to specify the electric heating of the process in comparison to thermal heating, a volumetric power (P_v) term should be incorporated into the energy balance. This term was omitted in the current study due to the unavailability of the experimental data needed for this term. Therefore, it is recommended to measure and collect the electrical resistivity, voltage and current in future experimental work to incorporate electric heating in the energy balance.

10.3. References

Crittenden, B. D., 2011. *Discussion on prototype* [email] (Personal communication, 5 December 2011).

Crittenden, B. D., Camus, O., Perera, S. P., Mays, T. J., Sánchez-Liarte, F., Tennison, S. R. & Crezee, E., 2011. Nonuniform channels in adsorbent monoliths. *AIChE Journal*, 57(5), pp.1163-1172.

Petkovska, M., Antov-Bozalo, D., Markovic, A. & Sullivan, P., 2007. Multiphysics modeling of electric-swing adsorption system with in-vessel condensation. *Adsorption*, 13(3-4), pp.357 -372.

Shen, C., Yu, J., Li., P. Grande, C. A. & Rodrigues, A. E., 2011. Capture of CO2 from gas by vaccum pressure swing adsorption using activated carbon beads. *Adsorption*, 17(1), pp. 179-188.

"We shall not cease from exploration
And the end of all our exploring
Will be to arrive where we started
And know the place for the first time."
T. S. Elliot